

EFFECT OF PARTICLE SIZE DISTRIBUTION AND PACKING  
CHARACTERISTICS ON RAILROAD BALLAST SHEAR STRENGTH: A  
NUMERICAL STUDY USING THE DISCRETE ELEMENT METHOD

by

S M Naziur Mahmud

A thesis

submitted in partial fulfillment

of the requirements for the degree of

Master of Science in Civil Engineering

Boise State University

August 2017

© 2017

S M Naziur Mahmud

ALL RIGHTS RESERVED

BOISE STATE UNIVERSITY GRADUATE COLLEGE

**DEFENSE COMMITTEE AND FINAL READING APPROVALS**

of the thesis submitted by

S M Naziur Mahmud

Thesis Title: Effect of Particle Size Distribution and Packing Characteristics on Railroad Ballast Shear Strength: A Numerical Study using the Discrete Element Method

Date of Final Oral Examination: 25 May 2017

The following individuals read and discussed the thesis submitted by student S M Naziur Mahmud, and they evaluated his presentation and response to questions during the final oral examination. They found that the student passed the final oral examination.

Debakanta Mishra, Ph.D. Chair, Supervisory Committee

Arvin Farid, Ph.D. Member, Supervisory Committee

Bhaskar Chittoori, Ph.D. Member, Supervisory Committee

The final reading approval of the thesis was granted by Debakanta Mishra, Ph.D., Chair of the Supervisory Committee. The thesis was approved by the Graduate College.

## DEDICATION

This thesis is dedicated to my family members and to you as a reader.

## ACKNOWLEDGEMENTS

I would like to express my sincere gratitude to the chair of my Supervisory Committee, Dr. Debakanta Mishra, for his guidance, constructive criticisms and patient encouragement throughout the research works related to this Master's thesis. I also wish to thank Dr. Arvin Farid and Dr. Bhaskar Chittoori for serving on my Supervisory Committee. The contributions of Derrick Blanksma and Dr. David Potyondy of Itasca Consulting Group, Inc. for help with PFC3D<sup>®</sup> related questions are highly acknowledged. I would also like to thank Ali Khoubani, a PhD student at Oregon State University, for helping me with the basic understanding of PFC3D<sup>®</sup>. Finally, I would like to thank my family members for their continued support and faith during the period of this research.

## ABSTRACT

Railroad infrastructure plays a significant role in sustaining the economy of a country, and facilitates fast, safe and reliable transportation of passengers as well as commodities. Significant capital investments are required for the construction and maintenance of a railroad network that is structurally and functionally adequate. The ballast layer is one of the main structural components of a conventional rail track system, and comprises coarse-grained unbound particles, often as large as 63 *mm* in size. The ballast as a load-bearing layer resists train-induced stresses through particle-particle interaction. Accordingly, particle-size distribution and packing characteristics are important factors that govern the mechanical behavior of the ballast layer under loading. A well-performing ballast layer should ideally possess optimum drainage characteristics to ensure rapid removal of surface water and adequate shear strength to restrain the track against excessive movement under loading. In-depth understanding of different factors affecting ballast behavior can help reduce recurrent costs associated with ballast maintenance.

Conducting common shear strength tests on coarse-grained geomaterials such as railroad ballast, and performing parametric studies to quantify the effects of different material, specimen, and test parameters on shear strength properties is often not feasible in standard geotechnical engineering laboratories due to the significantly large specimen and test setup requirements. In such situations, the Discrete Element Method (DEM) that facilitates micromechanical analysis of particulate matter becomes a logical alternative.

The primary objective of this research effort is to study the effects of particle-size distribution and packing characteristics on the shear strength behavior of railroad ballast. This was accomplished by simulating commonly used laboratory shear strength tests such as Direct Shear Test and Triaxial Monotonic Shear Strength Test using DEM. A commercially available three-dimensional DEM package (Particle Flow Code - PFC3D<sup>®</sup>) was used for this purpose. Published laboratory-test data were used to calibrate the numerical model. A series of parametric analyses were subsequently carried out to quantify the individual effects of different variables being studied on ballast shear strength behavior. In an effort to increase ballast shear strength through better packing within the granular matrix, a new gradation parameter, termed as the “Coarse-to-Fine (C/F) Ratio” was proposed. Changing the ‘coarse’ and ‘fine’ fractions within a particular gradation specification, the resulting effect on ballast shear strength was studied. In addition to studying the particle-to-particle interaction within the ballast matrix, this study also focused on studying the phenomenon of geogrid-ballast interaction under different packing conditions. A recently developed parameter known as the “Geogrid Gain Factor” was used to quantify the benefits of geogrid reinforcement of ballast. The ultimate objective was to further the understanding of ballast behavior under loading, which will ultimately lead to the design and construction of better-performing railroad tracks.

## TABLE OF CONTENTS

DEDICATION .....	iv
ACKNOWLEDGEMENTS .....	v
ABSTRACT .....	vi
LIST OF TABLES .....	xiii
LIST OF FIGURES .....	xvi
CHAPTER 1: INTRODUCTION .....	1
1.1 Introduction.....	1
1.2 Background and Problem Statement.....	2
1.3 Research Objectives and Tasks.....	6
1.4 Outline of the Thesis Document .....	7
CHAPTER 2: REVIEW OF PUBLISHED LITERATURE .....	9
2.1 Introduction.....	9
2.2 Components of a Ballasted Railroad Track .....	9
2.2.1 Superstructure.....	11
2.2.2 Substructure.....	12
2.3 Railroad Ballast: Functions and Properties.....	13
2.3.1 Functions of a Ballast Layer.....	14
2.3.2 Ballast Gradation.....	14
2.3.3 Particle Shape Properties and their Effect on Railroad Ballast Behavior .....	21

2.3.4	Shear Strength Testing of Ballast.....	24
2.3.5	Resilient Behavior of Railroad Ballast.....	29
2.4	Discrete Element Modeling of Granular Material .....	31
2.4.1	Principles of Discrete Element Modeling .....	32
2.5	Introduction to PFC3D <sup>®</sup> as a DEM Tool .....	34
2.5.1	The PFC3D <sup>®</sup> Model .....	35
2.5.2	Cycling Sequence.....	37
2.5.3	Contact Constitutive Models.....	41
2.6	Use of Geosynthetics in Transportation Structures .....	44
2.6.1	Introduction to Geogrids .....	44
2.6.2	Introduction to Geogrid Gain Factor.....	48
2.7	Summary.....	49
<b>CHAPTER 3: DISCRETE ELEMENT MODELING OF DIRECT SHEAR STRENGTH TEST ON RAILROAD BALLAST.....</b>		<b>51</b>
3.1	Introduction.....	51
3.2	DEM Simulation of Direct Shear Test (DST).....	51
3.2.1	Specimen Preparation and Testing.....	52
3.2.2	Monitoring.....	63
3.2.3	Visualization of Shear Band.....	64
3.3	Model Calibration Using Laboratory-Test Data.....	65
3.3.1	Model Calibration - Using Spheres.....	66
3.3.2	Model Calibration - Using 2-ball Clumps.....	68
3.4	Parametric Study on Direct Shear Test (DST) Results.....	69
3.4.1	Effect of Ballast Gradations .....	70

3.4.2	Effect of Flat & Elongated Ratio.....	74
3.4.3	Effect of Particle Angularity .....	75
3.4.4	Effect of Aggregate Top-Size .....	78
3.4.5	Effect of Material Specific Gravity.....	79
3.4.6	Effect of Specimen Porosity.....	79
3.4.7	Effect of Coefficient of Inter-Particle Friction.....	81
3.4.8	Effect of Applied Normal Stress Level.....	82
3.5	Study of Ballast Packing Conditions Using the Concept of Coarse to Fine Ratio	83
3.5.1	Development of a Coarse to Fine Ratio Gradation Parameter for Railroad Ballast - Alternative – 1 .....	84
3.5.2	Development of a Coarse to Fine Ratio Gradation Parameter for Railroad Ballast - Alternative – 2 .....	88
3.5.3	Effect of C/F Ratio on Ballast Shear Strength .....	90
3.6	Limitations of the Direct Shear Testing.....	94
3.7	Summary of Results of Direct Shear Strength Testing of Railroad Ballast	96
<b>CHAPTER 4: DISCRETE ELEMENT MODELING OF TRIAXIAL MONOTONIC SHEAR STRENGTH TESTS.....</b>		<b>99</b>
4.1	Introduction.....	99
4.2	DEM Simulation of Triaxial Monotonic Shear Strength Tests (TXT) .....	99
4.2.1	Specimen Preparation and Testing.....	100
4.2.2	Model Calibration Using Laboratory-Test Data .....	109
4.3	Effect of Different Material, Specimen, and Test Parameters on Triaxial Shear Strength Test (TXT) Results.....	112
4.3.1	Effect of Ballast Gradations .....	113

4.3.2	Effect of Material Specific Gravity.....	115
4.3.3	Effect of Specimen Porosity.....	116
4.3.4	Effect of Coefficient of Inter-Particle Friction.....	117
4.3.5	Effect of Applied Confining Pressure Levels .....	118
4.3.6	Effect of Moisture (Suction Pressure).....	119
4.4	Limitations of the Triaxial Monotonic Shear Strength Testing of Railroad Ballast	121
4.5	Summary of Results of Triaxial Monotonic Shear Strength Testing of Railroad Ballast.....	122
4.6	Comparison of Parametric Study Results of Direct Shear Testing and Triaxial Monotonic Shear Strength Testing on Railroad Ballast.....	123
<b>CHAPTER 5: DISCRETE ELEMENT MODELING OF GEOGRID EMBEDDED CYCLIC TRIAXIAL TESTING .....</b>		<b>125</b>
5.1	Introduction.....	125
5.2	DEM Simulation of Geogrid Embedded Cyclic Triaxial Testing .....	125
5.2.1	Specimen Preparation and Testing.....	127
5.2.2	Calculation of Geogrid Gain Factor .....	134
5.3	Parametric Study on Cyclic Triaxial Testing of Geogrid-Embedded Railroad Ballast Specimens .....	136
5.3.1	Effect of Ballast Gradations .....	137
5.3.2	Effect of Geogrid Aperture Size.....	138
5.3.3	Effect of Geogrid Location .....	139
5.4	Limitations Associated with DEM Simulations of Cyclic Triaxial Testing on Geogrid-Embedded Ballast Specimens.....	140
5.5	Summary of Results from DEM Simulations of Cyclic Triaxial Testing on Geogrid-Embedded Ballast Specimens.....	141

CHAPTER 6: SUMMARY OF FINDINGS AND RECOMMENDATIONS FOR FUTURE RESEARCH .....	142
6.1 Introduction.....	142
6.2 Summary of Findings.....	142
6.3 Recommendations for Future Research .....	146
REFERENCES .....	148

## LIST OF TABLES

Table 2.1	Cumulative Percent Passing Individual Sieve Sizes for Typical AREMA Ballast Gradations (adopted from Manual for Railway Engineering, 2016) .....	16
Table 3.1	Relative Radius Magnitudes Associated with Different Ballast Shapes used in the DEM Simulations of DST .....	54
Table 3.2	Cumulative Percent Passing Individual Sieve Sizes for the Ballast Gradations used in the Current Study .....	57
Table 3.3	Parameters used for DEM Simulations of Direct Shear Strength Tests ...	62
Table 3.4	Parameters used in Calibrating the DEM Model of Direct Shear Tests (Ballasts Simulated as Spherical Balls) .....	68
Table 3.5	Angle of Internal Friction Values for Different Ballast Gradations Established through DEM Simulation of Direct Shear Tests .....	72
Table 3.6	Comparative Evaluation of Angle of Internal Friction Showing the Effect of F & E Ratio.....	75
Table 3.7	Comparative Evaluation of Angle of Internal Friction Showing the Effect of Degree of Angularity .....	76
Table 3.8	Comparative Evaluation of Angle of Internal Friction Showing the Effect of Particle Shapes.....	77
Table 3.9	Comparative Evaluation of Angle of Internal Friction Values for Different Aggregate Top Sizes .....	78
Table 3.10	Comparative Evaluation of Angle of Internal Friction for Different Material Specific Gravity.....	79
Table 3.11	Comparative Evaluation of Angle of Internal Friction for Different Specimen Porosity .....	80
Table 3.12	Comparative Evaluation of Angle of Internal Friction Showing the Effect of Coefficient of Inter-particle Friction .....	82

Table 3.13	Examples of the Coarse-to-Fine Ratio Concept for Railroad Ballasts – For AREMA #24 Gradations.....	87
Table 3.14	Examples of the Gravel-to-Sand Ratio Concept for Railroad Ballasts – For AREMA #4 Gradations.....	88
Table 3.15	Examples of the Coarse-to-Fine Ratio (C/F Ratio) Concept for Railroad Ballasts – For AREMA #24 Gradations .....	89
Table 3.16	Examples of the Coarse-to-Fine Ratio (C/F Ratio) Concept for Railroad Ballasts – For AREMA #4 Gradations .....	90
Table 3.17	Comparative Evaluation of Angle of Internal Friction Showing the Effect of Coarse-to-Fine Ratio (for AREMA #24 Gradations) .....	92
Table 3.18	Comparative Evaluation of Angle of Internal Friction Showing the Effect of Coarse-to-Fine Ratio (for AREMA #4 Gradations) .....	94
Table 4.1	Relative Radius Magnitudes Associated with Different Ballast Shapes used in the DEM Simulations of Triaxial Shear Strength Tests .....	101
Table 4.2	Cumulative Percent Passing Individual Sieve Sizes for the Ballast Gradations used for Simulating Triaxial Shear Strength Tests.....	102
Table 4.3	Parameters used in Calibrating the DEM Model of Triaxial Monotonic Shear Strength Tests .....	111
Table 4.4	Comparative Evaluation of Shear Strength Parameters for Different Ballast Gradations.....	115
Table 4.5	Comparative Evaluation of Shear Strength Parameters for Different Material Specific Gravity.....	116
Table 4.6	Comparative Evaluation of Shear Strength Parameters for Different Specimen Porosity .....	117
Table 4.7	Comparative Evaluation of Shear Strength Parameters Showing the Effect of Coefficient of Inter-particle Friction .....	118
Table 4.8	Comparative Evaluation of Shear Strength Parameters Showing the Effect of Suction Pressure (Results Illustrated for the Calibrated Model using Lab Data).....	120
Table 4.9	Comparison of Parametric Study Results of Direct Shear Testing and Triaxial Monotonic Shear Strength Testing on Railroad Ballast.....	123

Table 5.1	Parameters Used in the DEM Simulations of Geogrid (Stahl and te Kamp, 2013) .....	128
Table 5.2	Parameters Used in the DEM Simulations of Geogrid Embedded Cyclic Triaxial Testing of Railroad Ballasts .....	133
Table 5.3	Comparative Evaluation of Geogrid Gain Factor Values Showing the Effect of Ballast Gradations.....	138
Table 5.4	Comparative Evaluation of Geogrid Gain Factor Showing the Effect of Geogrid Aperture Size .....	138
Table 5.5	Comparative Evaluation of Geogrid Gain Factor Showing the Effect of Geogrid Location .....	140

## LIST OF FIGURES

Figure 2.1	Schematic of a Typical Ballasted Track: (a) Side View; (b) Cross-Sectional View (Selig and Waters, 1994).....	10
Figure 2.2	Contributions of Different Layers towards Overall Track Settlement (Selig and Waters, 1994).....	13
Figure 2.3	AREMA-Recommended Gradation Bands for #4 and #24 Ballast Materials (adopted from Manual for Railway Engineering, 2016).....	16
Figure 2.4	Illustration of the Longest and Shortest Perpendicular Dimensions (for Defining F & E Ratio) (adopted from Huang, 2010).....	21
Figure 2.5	Parameters for Determining the Degree of Angularity (after Lees, 1994)	23
Figure 2.6	Degree of Angularity Chart (after Lees, 1994).....	24
Figure 2.7	Schematic Representation of the Direct Shear Test Setup.....	27
Figure 2.8	Schematic Diagram of Triaxial Monotonic Shear Strength Test.....	28
Figure 2.9	Schematic Diagram of Mohr-Coulomb Plot.....	29
Figure 2.10	Response of Granular Material Subjected to Triaxial Loading, and Measurement of Resilient-Modulus (Buchanan, 2007).....	30
Figure 2.11	Resilient-Modulus ( $M_R$ ) Response of Railroad Ballast under Different Stress States (after Lackenby et al., 2007).....	31
Figure 2.12	Flow Chart Showing the Main Principles of DEM (adopted from What Is DEM Ebook, 2017).....	34
Figure 2.13	Internal Force and Moment Acting on the Two Pieces at a Ball-Ball Contact (Itasca, 2016).....	37
Figure 2.14	Sequence of Primary Operations that Occur during Each Simulation Cycle, Termed as the Cycle Sequence (adopted from Itasca, 2016).....	38
Figure 2.15	Schematics Illustrating Typical Geogrid Types: (a) Uniaxial Geogrid; (b) Biaxial Geogrid; (c) Triaxial Geogrid (Das, 2010).....	46

Figure 2.16	A Schematic Illustrating the Mechanism of Aggregate-Geogrid Interlocking (after Penman and Priest, 2009) .....	47
Figure 3.1	Ballast Particle Shapes used for Discrete Element Modeling of Direct Shear Strength Tests in the Current Study: (a) Spherical; (b) 2-ball clump; (c) 4-ball clump; and (d) 8-ball clump .....	54
Figure 3.2	Ballast Shapes Generated Corresponding to Different Flat and Elongated Ratio Values (a) F&E = 2.3; (b) F&E = 3.0; (c) F&E = 3.5 .....	55
Figure 3.3	Ballast Shapes Generated Corresponding to Different Angularity Values: Front View of (a) A = 300 to 399; (b) A = 600 to 699; (c) A = 900 to 999; Top View of (d) A = 300 to 399; (e) A = 600 to 699; (f) A = 900 to 999 .....	55
Figure 3.4	Ballast Shapes Generated using Different Number of Pebbles (NOP) per the “Surface-Calculate” Command: (a) NOP = 10; (b) NOP = 15; (c) NOP = 20; (d) NOP = 25; (e) NOP = 30; (f) NOP = 34 .....	56
Figure 3.5	Ballast Gradations Used for Direct Shear Tests in this Research Study...	57
Figure 3.6	Schematic Representation of the Linear Contact Model Incorporated in PFC (Itasca, 2016) .....	59
Figure 3.7	Model Direct Shear Strength Test Specimen Generated: (a) Before Shearing; (b) After Shearing .....	64
Figure 3.8	Visualization of the Shear Band in Direct Shear Strength Testing Simulation .....	65
Figure 3.9	Photograph of Direct Shear Test Equipment at the University of Illinois at Urbana-Champaign (Huang et al., 2009) .....	66
Figure 3.10	Model Calibration using Laboratory-Test Data (Ballast Particles Simulated as Spherical Balls) .....	67
Figure 3.11	Model Calibration using Laboratory-Test Data (Ballast Particles Simulated as 2-ball Clumps) .....	69
Figure 3.12	Calculating the Shear Strength Parameters (Results Presented for the Control Specimen Comprising Spherical Particles) .....	70
Figure 3.13	Comparative Evaluation of Failure Shear Stress for (a) AREMA #4 and (b) AREMA #24 Ballast Gradations .....	71
Figure 3.14	Comparative Evaluation of Coordination Number for (a) AREMA #4 and (b) AREMA #24 Gradations .....	73

Figure 3.15	Comparative Evaluation of Failure Shear Stress for Specimens Comprising Particles with Different F & E Ratio.....	75
Figure 3.16	Comparative Evaluation of Failure Shear Stress for Different Degree of Angularity of Ballasts .....	76
Figure 3.17	Comparative Evaluation of Failure Shear Stress for Different Particle Shapes .....	77
Figure 3.18	Comparative Evaluation of Failure Shear Stress for Different Aggregate Top Sizes.....	78
Figure 3.19	Comparative Evaluation of Failure Shear Stress Showing the Effect of Material Specific Gravity.....	79
Figure 3.20	Comparative Evaluation of Failure Shear Stress Showing the Effect of Specimen Porosity .....	80
Figure 3.21	Comparative Evaluation of Failure Shear Stress Showing the Effect of Inter-particle Friction Coefficient.....	81
Figure 3.22	Comparative Evaluation of Failure Shear Stress Showing the Effect of Applied Normal Stress Level.....	83
Figure 3.23	Schematic of Particles in a Box (figure not drawn to scale) (adopted from Vavrik et al., 2002) .....	86
Figure 3.24	Ballast Gradation used in this Research to Study the Effect of Coarse-to- Fine Ratio (for AREMA #24 Gradations) .....	91
Figure 3.25	Comparative Evaluation of Failure Shear Stress Showing the Effect of Coarse-to-Fine Ratio (for AREMA #24 Gradations).....	91
Figure 3.26	Ballast Gradation used in this Research to Study the Effect of Coarse-to- Fine Ratio (for AREMA #4 Gradations) .....	93
Figure 3.27	Comparative Evaluation of Failure Shear Stress Showing the Effect of Coarse-to-Fine Ratio (for AREMA #4 Gradations).....	93
Figure 4.1	Ballast Particle Shapes used for Discrete Element Modeling of Triaxial Shear Strength Tests in the Current Study: (a) 2-ball Clump_1; (b) 2-ball Clump_2; (c) 3-ball Clump_1; and (d) 3-ball Clump_2 .....	100
Figure 4.2	Schematic Representation of the Hill Contact Model between Two Spheres (Potyondy, 2016).....	103

Figure 4.3	Cylindrical Shaped Physical Vessel used in DEM Simulation of Triaxial Shear Strength Test (modified from Potyondy, 2017a).....	104
Figure 4.4	Boundary-contraction Packing Procedure: (a) Initial Particle Cloud at End of Step 1, (b) Relaxed Particle Cloud at End of Step 2, and (c) Compacted Granular Assembly at End of Step 3 (Potyondy, 2017a).....	106
Figure 4.5	Cylindrical Triaxial Monotonic Shear Strength Testing Specimen Generated using DEM (after Material-Genesis Procedure).....	108
Figure 4.6	Ballast Gradation Used in this Research Study for Triaxial Monotonic Shear Strength Testing Model Calibration using Lab Data.....	110
Figure 4.7	Particle-Size Distribution Achieved during the Triaxial Monotonic Shear Strength Test Model Calibration.....	111
Figure 4.8	Triaxial Monotonic Shear Strength Test Model Calibration Using Laboratory-Test Data.....	112
Figure 4.9	Typical Mohr's Circle Drawn from Triaxial Monotonic Shear Strength Testing of Railroad Ballasts for Calculating the Shear Strength Parameters (Results Illustrated for the Calibrated Model using Lab Data).....	113
Figure 4.10	Comparative Evaluation of Peak Deviator Stress at Failure for Two Different AREMA Gradations: (a) AREMA #4 and (b) AREMA #24 ..	114
Figure 4.11	Comparative Evaluation of Peak Deviator Stress at Failure Showing the Effect of Material Specific Gravity.....	116
Figure 4.12	Comparative Evaluation of Peak Deviator Stress at Failure Showing the Effect of Specimen Porosity .....	117
Figure 4.13	Comparative Evaluation of Peak Deviator Stress at Failure Showing the Effect of Inter-particle Friction Coefficient.....	118
Figure 4.14	Comparative Evaluation of Peak Deviator Stress at Failure Showing the Effect of Applied Confining Pressure Levels .....	119
Figure 4.15	Comparative Evaluation of Peak Deviator Stress at Failure Showing the Effect of Applied Suction Pressure (Results Illustrated for the Calibrated Model using Lab Data) .....	120
Figure 5.1	DEM Simulation of Cyclic Triaxial Testing on Geogrid-Embedded Ballast Specimens (Illustrates Model State after the Test is Complete) (adopted from Potyondy, 2017b).....	126

Figure 5.2	Undeformed Configuration of a Grid Layer (a) Showing Grid Balls, and (b) Grid Bonds .....	129
Figure 5.3	Grid-embedment Procedure: (a) Constrained Grid and Initial Particle Cloud at End of Step 2, (b) Constrained Grid and Relaxed Particle Cloud at End of Step 3, (c) Constrained Grid and Compacted Granular Assembly at End of Step 4, and (d) Unconstrained and Deformed Grid at End of Step 5 (Potyondy, 2017b).....	131
Figure 5.4	Geogrid Embedded Cylindrical Triaxial Shear Strength Test Specimen Simulated using DEM.....	132
Figure 5.5	Typical Deviator Stress vs Axial Strain Plot from Cyclic Triaxial Testing on a Geogrid-Embedded Ballast Specimen .....	134
Figure 5.6	Resilient-Modulus versus Porosity for Reinforced and Unreinforced Configurations Models Varying Friction Coefficient Values, Tested under Moist Conditions at 150 kPa Confinement (after Potyondy, 2017b).....	136
Figure 5.7	Geogrid-Embedded Cylindrical Test Specimens at the End of Material Genesis Procedure: (a) Two Layers of Geogrid - One Layer at 152 mm from the Top, the Second Layer at 152 mm from the Bottom; and (b) Two Layers of Geogrid - One Layer at 254 mm from the Top, and the Second Layer at 254 mm from the Bottom.....	139

## CHAPTER 1: INTRODUCTION

### 1.1 Introduction

The railroad track system forms an integral part of the transportation infrastructure of a country and plays a significant role in sustaining a healthy economy. The railway constitutes a fuel-efficient and environment-friendly mode of transportation. According to an independent study for the Federal Railroad Administration (FRA), moving freights by railroads, on average, is three to four times more fuel-efficient than by trucks (Vantuono, 2011). Environmental Protection Agency (EPA) data show that freight railroads contributed only 0.6% to the total greenhouse gas emission in the United States (U.S.) in spite of accounting for approximately 40% of the total amount of freight transported by volume (Vantuono, 2011). It is expected that there will be a 40% increase in the total U.S. freight shipments by 2045, which will increase the need for improved railroad infrastructure (Rail Intermodal Keeps America Moving, 2016). Notable increase in domestic and international freight volumes in the U.S. were observed from 1998 to 2010, and the volume in 2020 is expected to increase by 49% compared to that in 2010 (Warne, 2004). The demand for faster trains has been increasing consistently over the recent past owing to ever-increasing traffic congestions and fuel costs. Significant annual investments are required to construct and maintain a railroad track network that is structurally and functionally adequate. In-depth understanding of the mechanics of track behavior is necessary to facilitate the development and maintenance of a reliable railroad network.

## 1.2 Background and Problem Statement

The ballast layer is one of the main components of a conventional rail track structure comprising coarse-grained unbound particles, often as large as  $63\text{ mm}$  in size. The granular ballast is placed as the top layer of the railroad substructure, in the cribs between the crossties (also known as sleepers), and in the shoulders beyond the sleeper ends. The ballast layer serves two primary functions: (1) it ensures rapid removal of surface water from the track structure, and (2) it works as a load-bearing platform to support the superstructure, and dissipates train-induced stresses sufficiently to protect the underlying subgrade layer. Accordingly, a well-performing ballast layer should ideally possess optimum drainage and shear strength properties. Upon repeated train loading, the quality of the ballast layer deteriorates, and it becomes “dirty” or “fouled” through progressive accumulation of fines within the granular matrix (Indraratna et al., 2012). This “contamination” of the granular matrix leads to gradual deterioration in the drainage as well as shear strength properties, and can adversely affect track performance under loading. Past research studies have observed that, the ballast layer accounts for a major portion of total track settlement (Selig and Waters, 1994; Mishra et al., 2014b; Abadi et al., 2016). It has also been reported that a major portion of the track maintenance budget is spent on the substructure (Raymond et al., 1978; Ionescu et al., 1998). Therefore, in-depth understanding of the physical and mechanical characteristics of ballast is critical to facilitate the design, construction, and maintenance of well-performing track structures.

Ballast, as a load-bearing layer, resists train-induced stresses through particle-particle interaction; therefore, shear strength of the ballast layer is primarily dependent on particle-to-particle interlock. Accordingly, gradation (particle-size distribution) and

packing characteristics are the primary factors that govern the mechanical behavior of a ballast layer under loading. Gradation is one of the most influential characteristics in determining how unbound aggregates perform in a constructed structural layer. The importance of specifying proper aggregate grading has long been recognized for achieving satisfactory performance in pavement applications. Gradation is a key factor influencing not only the mechanical response of an unbound granular layer (often characterized by resilient-modulus, shear strength, and permanent deformation properties), but also permeability, frost susceptibility, and susceptibility to erosion (Bilodeau et al., 2007, 2008). Several researchers (Trollope et al., 1962; Thom and Brown, 1988; Dawson et al., 1996; Kolisoja, 1998; Lekarp, 1999; Ekblad, 2007) examined the impact of grain-size distribution on the performance of unbound materials, and recommended in-depth understanding of gradation in order to improve pavement design and construction procedures. Yideti et al. (2013) developed a packing theory-based framework as an effective tool to evaluate the permanent deformation susceptibility of unbound granular materials, regardless of particle shape, angularity and surface texture. In bound materials such as Hot-Mix Asphalt (HMA), aggregate gradation influences almost every important property including stiffness, permeability, workability, and resistance to moisture damage (Roberts et al., 1996). It has also been found that, in Portland Cement Concrete (PCC), gradation impacts durability, porosity, and aggregate-to-cement bond strength through surface area characteristics of different aggregate sizes. Extensive research has been conducted on the optimization of aggregate packing in the concrete industry (Roy et al., 1993; de Larrard and Sedran, 1994; and Goltermann et al., 1997). An optimized aggregate gradation leads to an increase in concrete strength by 10

to 20 percent (Goltermann et al., 1997). On the other hand, comparatively less attention has been focused on studying the effects of railroad ballast gradation and packing characteristics on overall structural performance of the ballast layer. Proper understanding of the effects of particle-size distribution and packing characteristics on ballast shear strength can potentially facilitate the optimization of track substructure design, ultimately leading to a reduction in recurrent track maintenance costs.

Commonly used tests to study the shear strength behavior of unbound granular materials are the direct shear test (DST), and the triaxial monotonic shear strength test (TXT). However, owing to the large particle-size (often as large as  $63\text{ mm}$ ) of railroad ballast, significantly large specimens have to be tested in the laboratory for realistic estimation of the shear strength properties. ASTM D 3080-90 (ASTM, 2011) is the test procedure commonly used to perform the direct shear strength tests in the laboratory. This test specification requires a minimum specimen thickness of six times the maximum particle diameter and a minimum specimen diameter or width of ten times the maximum particle diameter. However, from a practical point of view, a smaller apparatus to particle-size ratio has great advantage because it reduces the size of the specimen required for testing. For example, typical specimen sizes selected by researchers for direct shear testing of railroad ballast are  $400\text{ mm} \times 400\text{ mm} \times 300\text{ mm}$  (Dissanayake et al., 2016),  $300\text{ mm} \times 300\text{ mm} \times 200\text{ mm}$  (Indraratna et al., 2012; Ngo et al., 2014). Similarly, typical cylindrical specimen sizes used for triaxial monotonic shear strength testing of railroad ballast are,  $610\text{ mm}$  height  $\times$   $305\text{ mm}$  diameter (Qian et al., 2013, 2015; Mishra et al., 2014a),  $600\text{ mm}$  height  $\times$   $300\text{ mm}$  diameter (Indraratna et al., 2009, 2012; Lu and McDowell, 2010; Ngo et al. 2016),  $508\text{ mm}$  height  $\times$   $254\text{ mm}$  diameter (Kashani et al.,

2017, Rohrman et al., 2017), 300 mm height  $\times$  150 mm diameter (McDowell and Li, 2016).

Different factors (such as particle-size distribution, aggregate top-size, specimen porosity, material specific gravity, and inter-particle friction coefficient) can affect the response and performance of a ballast layer. It is critical to know the relative significance of each of these factors in order to facilitate improved material selection and design practices. Conducting shear strength tests on railroad ballast and performing parametric studies to quantify the effects of different material, specimen, and test variables on shear strength properties is often not feasible in standard geotechnical engineering laboratories because of the significantly large specimen and test setup requirements. In such situations, numerical modeling tools become logical alternatives to facilitate in-depth understanding of material behavior. One such numerical-modeling approach commonly used to study the behavior of particulate systems is the Discrete Element Method (DEM). The DEM can be used as an effective tool to conduct parametric studies on coarse-grained geomaterials for which extensive laboratory testing is often impractical. Furthermore, once modeled, identical specimens can be subjected to different simulated loading and testing conditions for a “true” parametric analysis by isolating the effects of individual factors being studied. Considering the inherent variations associated with preparation and testing of geomaterial specimens in the laboratory, such isolation of individual factors is often not possible. Parametric studies conducted using calibrated numerical models become the preferred approach in such cases.

### 1.3 Research Objectives and Tasks

The primary objective of this research effort was to study the effects of particle-size distribution and packing characteristics on the shear strength behavior of railroad ballast. Shear strength properties for both unreinforced and geogrid-reinforced specimens were studied through DEM simulations of direct-shear (for unreinforced specimens only) and triaxial monotonic shear strength tests (for both unreinforced and reinforced specimens). A commercially available three-dimensional DEM package PFC3D<sup>®</sup> was used for this purpose (Itasca, 2016). In-depth understanding of different factors affecting the shear strength behavior of railroad ballast would help to improve track-substructure design practices and subsequently reduce recurrent maintenance costs.

Different tasks carried out to accomplish the overall research objective are listed below.

1. Extensive review of published literature to gather information on railroad ballast behavior, discrete element modeling of ballasts, and the mechanism and benefits of ballast reinforcement using geogrids.
2. Development of a numerical model to simulate Direct Shear Testing of railroad ballast and calibration of the model using available laboratory-test data. A simpler version of the model was first developed using spherical-shaped particles. The model was subsequently modified to include complex particle shapes.
3. Studying the effects of particle-size distribution, aggregate top-size, specimen porosity, material specific gravity, and inter-particle friction coefficient on ballast shear strength through parametric analysis of simulated Direct Shear Strength Tests.

4. Introduction of a new gradation parameter termed as “Coarse-to-Fine Ratio” (C/F Ratio) as an indicator of packing condition within the ballast matrix. Changing the ‘coarse’ and ‘fine’ fractions within a particular gradation specification, and analyzing the resulting effects on ballast shear strength through simulated Direct Shear Strength Tests.
5. Studying the effects of particle-size distribution, specimen porosity, material specific gravity and inter-particle friction coefficient on ballast shear strength as established through DEM simulations of Triaxial Monotonic Shear Strength Tests. Note that a recently released “Material-Modeling Support Package” for PFC 5.0 (Potyondy, 2017a) was used as the basic framework for this modeling task.
6. Investigating the effects of different specimen and test parameters on the mechanism of geogrid-ballast interaction to assess potential implications on the benefits achieved through the geogrid reinforcement of ballast.

#### **1.4 Outline of the Thesis Document**

This Master’s thesis document comprises six chapters.

Chapter 2 summarizes findings from an extensive review of published literature on the functions of railroad ballast and different tests commonly used to characterize the stress-strain behavior of railroad ballast pertinent to the response of railroad track structures under loading. Brief discussions on fundamentals of the Discrete Element Method (DEM) and the underlying algorithm in PFC3D<sup>®</sup> have also been presented. Finally, the effects of geogrid inclusion in the ballast layer have been discussed.

Chapter 3 presents results from research tasks pertaining to simulation of direct shear tests using DEM. Details of the model development and calibration efforts have been presented. This is followed by results from parametric analyses performed to study the effects of (1) particle-size distribution, (2) aggregate top-size, (3) specimen porosity, (4) specimen density, and (5) inter-particle friction coefficient on ballast shear strength. A new gradation parameter termed as “Coarse-to-Fine Ratio” (C/F Ratio) has been introduced as an indicator of the packing condition within the ballast matrix. This is followed by discussions highlighting the limitations and major assumptions inherent to the current simulation approach.

Chapter 4 presents details concerning DEM simulation of triaxial monotonic shear strength testing of railroad ballast. Basic components of the model have been described along with details of the calibration effort. Finally, the results from the parametric study have been presented, and the findings have been compared to those from the DST simulations.

Chapter 5 discusses findings from studying the mechanism of geogrid-ballast interaction through DEM simulations. The increase in ballast resilient modulus due to geogrid reinforcement has been quantified, and the effects of different specimen and test parameters on this modulus increase have been studied.

Chapter 6 presents a summary of findings from different research tasks performed under the scope of this master’s thesis effort; recommendations for future research and developmental efforts have also been presented.

## CHAPTER 2: REVIEW OF PUBLISHED LITERATURE

### 2.1 Introduction

As already discussed, the objective of this research effort was to study the effects of particle-size distribution and packing characteristics on the shear strength behavior of railroad ballast. To accomplish this objective, a proper understanding of functions and properties of railroad ballast, typical shear strength testing protocols for ballast, discrete element modeling of ballast, and the mechanism and benefits of ballast reinforcement using geogrids is essential. Accordingly, an extensive literature review on research related to railroad ballast was undertaken, and the findings have been presented in this chapter. First, a general overview of conventional ballasted railroad track components has been presented, followed by an overview of ballast functions, properties, and different tests to characterize the stress-strain behavior of railroad ballast pertinent to the response of railroad track under loading. Subsequently, an introduction to the Discrete Element Method (DEM) as an advanced approach to the model behavior of particulate media such as railroad ballast has been described, followed by an introduction to PFC3D<sup>®</sup> as a software tool for discrete element modeling. Finally, some discussion on the use of geogrids for railroad ballast reinforcement has been presented.

### 2.2 Components of a Ballasted Railroad Track

Railroad track systems are constructed to provide a smooth and safe running surface for trains. Track components can be grouped into two main categories.

- (i) Superstructure - consists of the rails, fastening systems, and cross ties (sleepers), i.e., the top portion of the track; and
- (ii) Substructure - consists of the ballast, subballast, and subgrade layers, i.e., the lower portion of the track.

Components of a conventional ballasted railroad track are shown in Figure 2.1.

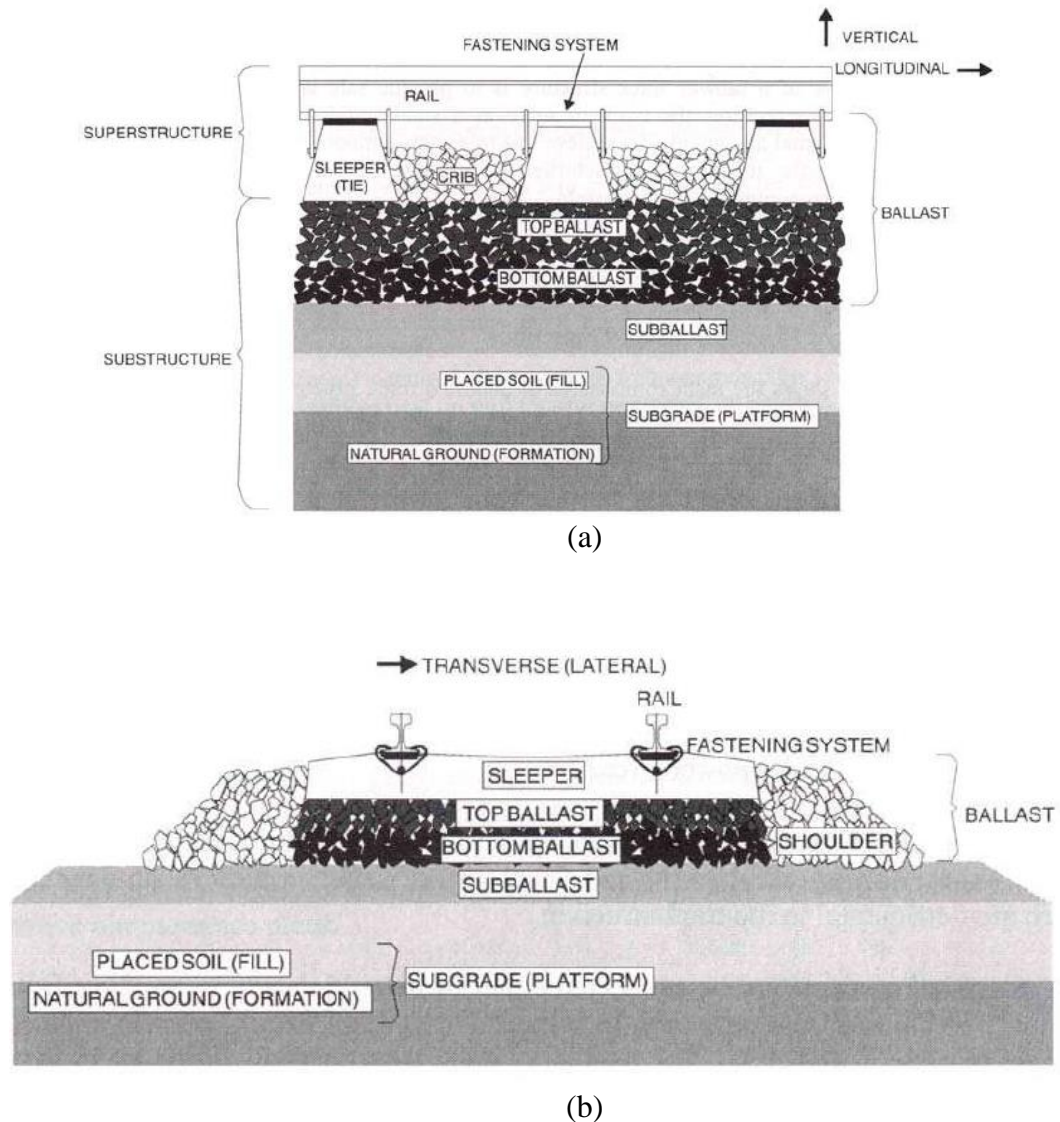


**Figure 2.1 Schematic of a Typical Ballasted Track: (a) Side View; (b) Cross-Sectional View (Selig and Waters, 1994)**

### 2.2.1 Superstructure

The railway track superstructure consists of the rails, fastening systems, and crossties (also referred to as ties, or sleepers), i.e., the top portion of the track. These components are the primary load carrying elements of the track structure, and transfer train-induced loads to the track substructure.

Rail: Rails are longitudinal steel members, which are in direct contact with the train wheels. The primary function of rails is to guide the train wheels; other functions are to transfer concentrated wheel loads to the sleepers and to act as electrical conductors for the signaling system. Rails must have sufficient stiffness to distribute wheel loads over multiple sleepers, and to limit deflection between the supports. Rail defects and discontinuities, such as joints, can cause large impact loads, which have detrimental effects on the riding quality and the track components below. The standard gage between two rails is 1435 *mm* (56.5 *in.*) in North America.

Fastening System: The main function of the fastening system is to retain the rails against the crossties and to resist vertical, lateral, longitudinal, and overturning movements of the rails. It acts as a means of absorbing rail loads elastically and transferring them to the underlying crossties. Besides, fastening system provides resiliency and damping for the superstructure.

Ties (Sleepers): The main functions of ties (sleepers) are to distribute the wheel loads transferred by the rails and fastening system to the supporting ballast and restrain rail movement by anchorage of the superstructure in the ballast. Ties are laid transversely to support and hold the rails and fastening systems to maintain track gauge, level, and alignment. They also restrict lateral, vertical, and longitudinal movements of the rails

through anchorage of the superstructure into the ballast. The most commonly used materials for manufacturing of ties are wood (timber) and reinforced concrete.

### 2.2.2 Substructure

Railway track substructure consists of the top ballast, subballast, and subgrade layers, i.e., the lower portion of the track.

Ballast: The granular ballast is placed as the top layer of the substructure, in the cribs between the crossties, and in the shoulders beyond the tie-ends. Ballast works as a load-bearing platform to support the train loading, and protect the subgrade. A more in-depth discussion on ballast functions, and different factors affecting railroad ballast behavior are provided in Section 2.3 of this document.

Subballast: Subballast is the blanket layer that separates the ballast and the subgrade to prevent interpenetration between the two layers. The primary function of this layer is to reduce the stress levels transferred through the ballast layer further to protect the subgrade layer, thus offering a less-expensive option to the otherwise thicker ballast. Subballast also allows good drainage of water. Crushed natural aggregates and sand-gravel mixtures are the most common materials used as subballast.

Subgrade: Subgrade is the foundation for the track structure, and consists of existing natural soil or placed soil. Since the subgrade provides the platform upon which the track is constructed, it must have sufficient bearing strength and stability as well as reasonable settlement behavior. The lack adequate subgrade strength often the cause of many track defects.

### 2.3 Railroad Ballast: Functions and Properties

The ballast layer is one of the main components of a conventional rail track structure comprising coarse-grained unbound particles, often as large as  $63\text{ mm}$  in size. According to Selig and Waters (1994), ideal ballast materials are angular, crushed, hard stones and rocks, uniformly graded, free of dust and dirt, and not prone to cementing action. Typically, crushed gravel, limestone, basalt, and granite have been used as ballasts for their various characteristics such as hardness, abrasion resistance, resistance to weathering action, etc.

The short- and long-term settlements of track structures under loading can be primarily attributed to deformations within different substructure layers. As shown in the Figure 2.2, the ballast layer accounts for most of the vertical deformation of a rail track. In order to reduce vertical track settlement, emphasis must be given to ensuring adequate performance of the ballast layer, which requires thorough understanding of the physical and mechanical properties of the ballast.

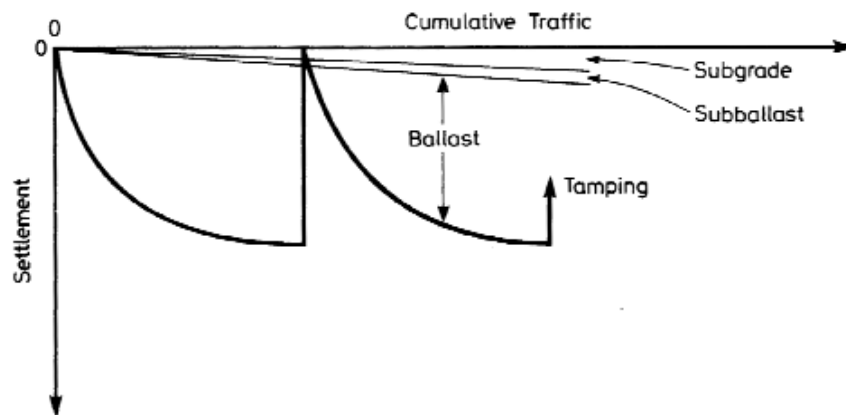


**Figure 2.2 Contributions of Different Layers towards Overall Track Settlement (Selig and Waters, 1994)**

### 2.3.1 Functions of a Ballast Layer

The main functions of a ballast layer can be summarized as follows (Selig and Waters, 1994).

- (i) To retain the track in its required position by withstanding the vertical, lateral, and longitudinal forces applied to the ties (sleepers);
- (ii) To provide the required degree of resiliency and energy absorption to the track, which in turn reduces stresses in the underlying materials to acceptable levels;
- (iii) To distribute stresses from the tie bearing area to acceptable stress levels for the subballast and subgrade, thereby, limiting permanent track settlement;
- (iv) To provide sufficient voids for storage of fouling material in the ballast, and movement of particles through the ballast;
- (v) To facilitate maintenance surfacing and lining operations (in order to adjust track geometry) through an ability to rearrange ballast particles with tamping; and
- (vi) To provide immediate drainage of water falling onto the track.

The ability of ballast to perform its functions depends on the following factors: (i) particle characteristics (e.g., particle-size, shape, angularity, hardness, surface texture, and durability), and (ii) the in-situ physical state (e.g., grain structure, and density). According to Selig and Waters (1994), no single characteristic controls ballast behavior and the overall performance of a ballast layer is the net combined effect of several characteristics.

### 2.3.2 Ballast Gradation

Gradation is a term used to describe the particle-size and distribution in a granular assembly, usually expressed as a relationship (gradation curve) between size and

percentage by weight of particles smaller than that size. Particle-size distribution (or gradation) is a key factor influencing not only the mechanical response of aggregates characterized by resilient-modulus, shear strength, and permanent deformation, but also permeability, frost susceptibility, and susceptibility to erosion (Bilodeau et al., 2007, 2008). Different particle-size distributions lead to packing order changes in the aggregate matrix, and may result in significantly different mechanical behavior. Therefore, to evaluate the shear strength behavior of granular materials such as railroad ballast, control of gradation is very important. Proper understanding of the effects of particle-size distribution and packing characteristics on ballast shear strength can potentially facilitate the optimization of track substructure design, ultimately leading to a reduction in recurrent track maintenance costs.

Typical gradations that are commonly specified by the American Railway Engineering and Maintenance-of-Way Association (AREMA) for mainline track usage in the United States are denoted as AREMA #4, and AREMA #24. Figure 2.3 shows the gradation curves for these two ballast types as specified by AREMA; Table 2.1 presents the same information in a tabular form. .

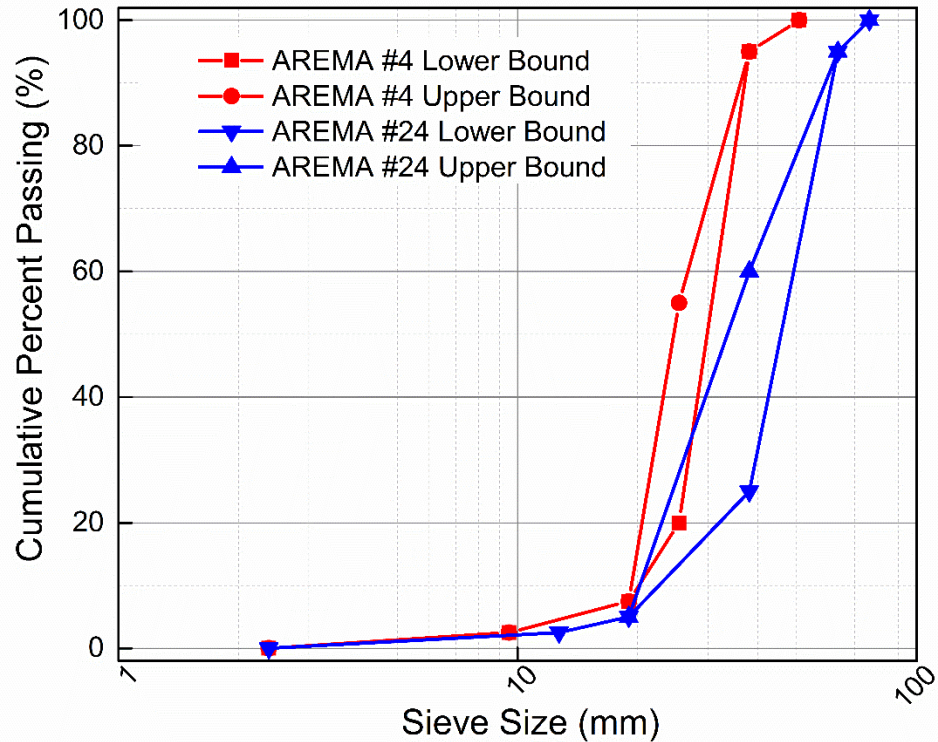


**Figure 2.3 AREMA-Recommended Gradation Bands for #4 and #24 Ballast Materials (adopted from Manual for Railway Engineering, 2016)**

**Table 2.1 Cumulative Percent Passing Individual Sieve Sizes for Typical AREMA Ballast Gradations (adopted from Manual for Railway Engineering, 2016)**

Sieve Size		AREMA #4	AREMA #24
(mm)	(in.)	Cumulative Percent Passing (%)	
76.2	3	N/A	100
63.5	2.5	N/A	90-100
50.8	2	100	N/A
38.1	1.5	90-100	25-60
25.4	1	20-55	N/A
19	¾	0-15	0-10
12.7	½	N/A	0-5
9.51	3/8	0-5	N/A
4.76	No. 4	N/A	N/A
2.36	No. 8	N/A	N/A

Note that ‘Lower Bound’ or ‘LB’ refers to any gradation conforming to the lower bound of the AREMA-specified gradation band (coarser side of the gradation band); similarly, ‘Upper Bound’ or ‘UB’ refers to the finer side of the gradation band. As can be seen from Figure 2.3 and Table 2.1, the cumulative percent passing for a particular sieve size can be significantly different for the lower and upper bounds of the specification. Therefore, it is possible for two ballast materials to have significantly different particle-size distributions, yet meet the same AREMA gradation specification. For example, the percent finer than the 38.1 mm (1.5 in.) sieve for the AREMA #24 gradation can range from 25% to 60%.

#### 2.3.2.1 Quantification Methods for Gradation

For establishing robust linkages between gradation and satisfactory unbound aggregate mechanical behavior, the development of performance-based gradation specifications is necessary (Xiao et al., 2012). Recent research efforts have attempted to quantify gradation curves as numbers on a continuous scale and relate them to mechanistic behavior trends. These analytic gradation measures can quantify the change in performance of a given aggregate material within specified gradation bands; such practices can lead to the development of optimized gradation zones (Bilodeau et al., 2007; Kim et al., 2007).

One commonly used approach to mathematically represent the particle-size distribution within a granular assembly was originally developed by Talbot and Richart (1923). The Talbot equation (Equation 2.1) describes a maximum density curve for a given maximum aggregate size (Talbot and Richart, 1923):

$$p_i = \left( \frac{D_i}{D_{\max}} \right)^n \quad \text{(Equation 2.1)}$$

where  $p_i$  = percentage of material by weight passing the  $i^{\text{th}}$  sieve size,  $D_i$  = opening size of this particular ( $i^{\text{th}}$ ) sieve,  $D_{\max}$  = maximum particle size in the aggregate material, and  $n$  = shape factor of the gradation curve. According to Equation 2.1, a given gradation curve can be represented as a point with coordinates  $(n, D_{\max})$  on a similar Cartesian plane where shape factor ( $n$ ) is on the x-axis and  $D_{\max}$  is on the y-axis.

Xiao et al. (2012) used the proportionality between gravel- and sand-sized particles (per ASTM D2487-11), as a gradation-related index property that could be related to the mechanical response of aggregate base materials under loading. Defining the proportionality as ‘Gravel-to-Sand Ratio’ (G/S Ratio), they evaluated how mechanical behavior such as shear strength and resilient-modulus characteristics of aggregate base-granular subbase materials can be quantified and related to grain-size distributions. The G/S ratio was derived from the two parameters of Talbot’s equation ( $D_{\max}$  and  $n$ ) established from the particle-size distribution (Xiao et al., 2012).

$$\frac{G}{S} = \frac{P_{75\text{mm}} - P_{4.75\text{mm}}}{P_{4.75\text{mm}} - P_{0.075\text{mm}}} = \frac{1 - \left( \frac{4.75}{D_{\max}} \right)^n}{\left( \frac{4.75}{D_{\max}} \right)^n - \left( \frac{0.075}{D_{\max}} \right)^n} = \frac{(D_{\max})^n - 4.75^n}{4.75^n - 0.075^n} \quad \text{(Equation 2.2)}$$

It can clearly be seen that the G/S ratio expression (Equation 2.2) uses parameters established from the full gradation curve, rather than only using the percent passing 4.75 mm (#4) and 0.075 mm (#200) sieve sizes. Note that the definitions for gravel and sand used by Xiao et al. (2012) follow the Unified Soil Classification System

(USCS), where any particle smaller than  $76\text{ mm}$  ( $3\text{ in.}$ ) but larger than  $4.75\text{ mm}$  ( $\#4$ ) is defined as ‘gravel’, and any particle smaller than  $4.75\text{ mm}$  ( $\#4$ ) and larger than  $0.075\text{ mm}$  ( $\#200$ ) sieve is defined as ‘sand’. However, it is important to note that the relative proportion of ‘gravel’ and ‘sand’ in the method proposed by Xiao et al. (2012) primarily governs the packing order within the mix. Although the G/S ratio developed by Xiao et al. (2012) was applied to quantify the gradation for dense-graded aggregate base and subbase materials, this approach may not be considered good while studying granular assemblies that have significantly different gradations than these dense-graded aggregates. For example, railroad ballast corresponds to significantly coarser gradations compared to dense-graded aggregates, and it is quite common for a railroad ballast material to contain no particles finer than  $4.75\text{ mm}$ . In such a case, the denominator in Equation 2.2 will become zero, thus rendering the calculation of G/S ratio impossible. In such cases, a modification to definition of G/S ratio may be warranted.

Another approach that has been used to quantify the packing within aggregate matrices is the Bailey Method. Originally developed for efficient design of asphalt mixes, the Bailey Method represents a systematic approach to blending aggregates to ensure adequate aggregate interlock as the backbone of an asphalt mix (Vavrik et al., 2002), and provides a better understanding of the relationship between aggregate gradation and voids in an asphalt mix. The Bailey Method uses two principles that are the basis of the relationship between aggregate gradation and mixture volumetrics: (1) aggregate packing, and (2) definition of coarse and fine aggregate. One unique aspect of the Bailey Method that distinguishes it from other aggregate packing studies is that in the Bailey method the definitions of ‘coarse’ and ‘fine’ particles are not based on fixed sieve sizes, but rather on

the relative distribution of particle sizes in a granular matrix. Certain sieve sizes, namely Half Sieve, Primary Control Sieve (PCS), Secondary Control Sieve (SCS), and Tertiary Control Sieve (TCS) are defined based on the Nominal Maximum Particle Size (NMPS; a Superpave® asphalt mix design terminology defined as one sieve larger than the first sieve that retains more than 10%), and amount of ‘coarse’ and ‘fine’ fractions in the matrix are calculated based on these standard sieve sizes. The combined aggregate blend is analyzed with the use of three parameters: the Coarse Aggregate Ratio (CA Ratio), Coarse Portion of the Fine Aggregate Ratio ( $FA_c$ ), and Fine Portion of the Fine Aggregate Ratio ( $FA_f$ ) (Vavrik et al., 2002). Equation 2.3 summarizes the essential equations associated with the Bailey method.

$$\text{Half sieve} = 0.5 \times \text{NMPS}$$

$$\text{PCS} = 0.22 \times \text{NMPS}; \text{SCS} = 0.22 \times \text{PCS}; \text{TCS} = 0.22 \times \text{SCS}$$

$$\text{CA Ratio} = \frac{\% \text{ passing the half sieve} - \% \text{ passing PCS}}{100\% - \% \text{ passing the half sieve}}$$

$$FA_c = \frac{\% \text{ passing SCS}}{\% \text{ passing PCS}}$$

$$FA_f = \frac{\% \text{ passing TCS}}{\% \text{ passing SCS}} \quad \text{(Equation 2.3)}$$

The PCS designates the boundary between coarse and fine particles in the blend (Vavrik et al., 2002). Note that the value of 0.22 used in the control sieve equation was determined from two- and three-dimensional analyses of the packing for different shaped particles (Vavrik et al., 2002). As the definition of ‘coarse’ and ‘fine’ fractions in an aggregate blend are not restricted to certain sieve sizes, the Bailey method can be applied

to studying the packing characteristics in both dense-graded aggregate base/subbase as well as coarser geomaterials such as railroad ballast.

### 2.3.3 Particle Shape Properties and their Effect on Railroad Ballast Behavior

Granular materials such as aggregate base/subbase and railroad ballast must meet certain specifications to be acceptable in pavement and railroad applications. Parameters that have been used to define particle shape include flakiness or flatness, elongation, and roundness or angularity (Selig and Roner, 1987). The following subsections briefly describe typical aggregate shape characteristics and their effects aggregate on shear strength.

#### 2.3.3.1 Flakiness and Elongation

Flakiness or flatness refers to the ratio of particle thickness to width (intermediate dimension), and elongation refers to the ratio of length to width (Selig and Roner, 1987). The flakiness or flatness and elongation is expressed widely using the Flat and Elongated Ratio (F & E Ratio) defined as the ratio of the longest dimension of the particle to its minimum dimension (Equation 2.4 and Figure 2.4).

$$\text{F \& E Ratio} = \frac{\text{Longest Dimension}}{\text{Shortest Perpendicular Dimension}} \quad (\text{Equation 2.4})$$

**Shortest dimension perpendicular to the longest**

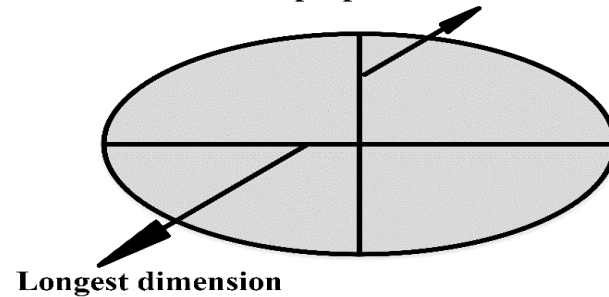


**Figure 2.4 Illustration of the Longest and Shortest Perpendicular Dimensions (for Defining F & E Ratio) (adopted from Huang, 2010)**

Per AREMA guidelines, the ballast material should be open graded with hard, angular-shaped particles providing sharp corners and cubical fragments with a minimum of flat and elongated particles (maximum 5% by weight over 3 to 1 ratio) (Tutumluer et al., 2006). Increasing the percentage of flaky particles increases the amount of breakage during compaction. This breakage leads to a change in gradation, which in turn results in reduced permeability, and potentially adverse effects on ballast shear strength.

Researchers have studied the effect of flaky particles on the shear strength of granular materials over the years. For example, Dunn and Bora (1972) tested a hard, crushed limestone aggregate (particle-size ranging from 4.8 *mm* to 38 *mm*) with a varying percentage of flaky particles in a special triaxial device. They found that, any amount of flaky particles increased the shear strength. However, the results suggested that the range of 25 to 75 percent flaky particles was better than 100 percent. Gur et al. (1967) reported that shear strength from triaxial tests was greater with flaky material than with non-flaky material. It should be noted that, flat and elongated particles have a general tendency to break during construction and under traffic loads (Huang, 2010), which is often detrimental to the structural response of the constructed layer.

#### 2.3.3.2 Angularity and Roundness

Various researchers have proposed different methods to quantify the angularity of particles. For example, the use of image analysis to quantify the angularity of coarse and fine aggregates has been studied extensively (Masad and Button, 2000; Masad et al., 2001; Sukumaran and Ashmawy, 2001; Rao et al., 2002; Pan et al., 2004, 2005). Lees (1964) proposed a method for determining the degree of angularity, which accounts not only for the roundness of corners but also how far the projection is from the inscribed

circle (see Figure 2.5). According to Lees (1964), the degree of angularity is calculated by the following equation (Equation 2.5).

$$A_i = (180^\circ - a) \times \frac{x}{r} \quad \text{(Equation 2.5)}$$

where  $A_i$  = the degree of angularity;  $a$  = measured angle;  $x$  = the distance to the tip of the corner from the center of the maximum inscribed circle, and  $r$  = radius of the maximum inscribed circle.

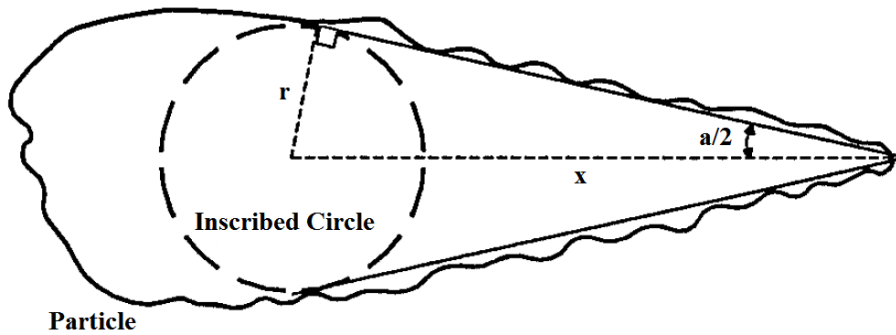


**Figure 2.5 Parameters for Determining the Degree of Angularity (after Lees, 1994)**

The total degree of angularity ( $A$ ) is the sum of all the values for all corners measured in three mutually perpendicular planes. Because of the high degree of complexity associated with this calculation approach, Lees (1964) developed a visual chart for determining the degree of angularity of particles (see Figure 2.6).

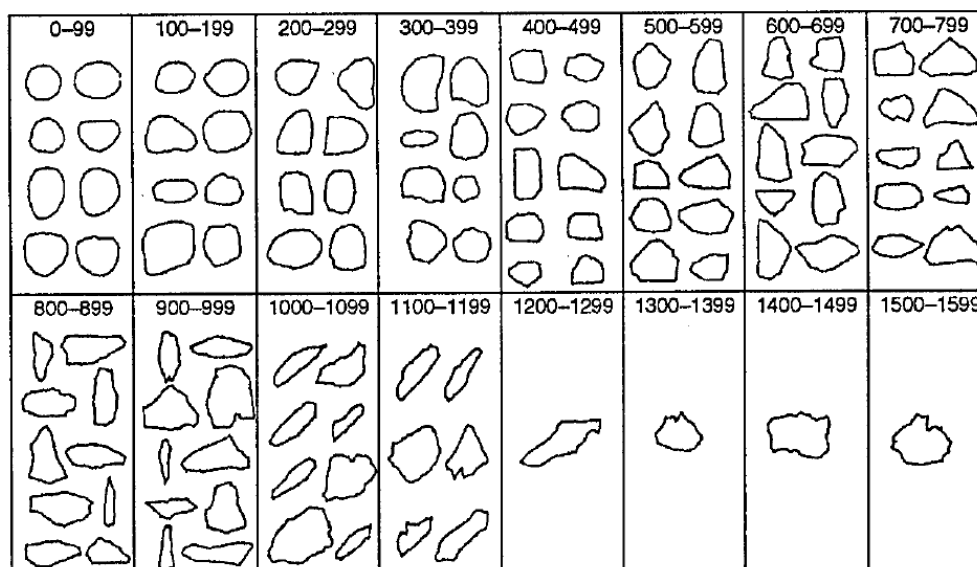


**Figure 2.6 Degree of Angularity Chart (after Lees, 1994)**

Chen (1948) conducted triaxial tests on various sands and gravels with densities ranging from loose to compact, and found that although the modulus decreased with increasing angularity, the shear strength increased. Jensen et al. (2001) reported that as the angularity increases, the angle of internal friction increases. Pan et al. (2006) reported that resilient modulus typically increases with aggregate angularity.

#### 2.3.4 Shear Strength Testing of Ballast

The shear strength of a granular material is a measure of the resistance of the material to deformation by continuous displacement of individual particles. The shear strength of an unbound granular matrix is primarily dependent on particle-to-particle interlock. Shear failure occurs when the stresses between the particles are such that they slide or roll past each other. A well-performing ballast layer should possess sufficient shear strength to resist excessive deformations as well as shear failure under train loading.

The shear strength of a soil (coarse- or fine-grained) is made up of two components: (i) frictional: due to friction between individual particles; and (ii) cohesive -

due to cohesive forces between the soil particles. The two components are combined in Coulomb's shear strength equation (Equation 2.6):

$$\tau_f = c + \sigma_N \times \tan(\phi) \quad \text{(Equation 2.6)}$$

where  $\tau_f$  is the shear strength;  $c$  is the apparent cohesion;  $\sigma_N$  is the applied normal stress on the shear plane and  $\phi$  is the angle of internal friction. Note that  $c = 0$  for cohesion-less materials such as railroad ballast.

The most commonly used laboratory-tests for characterizing the shear strength properties of granular materials such as aggregates and railroad ballasts are: (1) Direct Shear Test, and (2) Monotonic Triaxial Shear Strength Test. Brief descriptions of these two tests have been presented below.

#### 2.3.4.1 Direct Shear Strength Testing

The direct shear test is a quick and inexpensive test to obtain the shear strength parameters of both cohesive and non-cohesive soils either in undisturbed or remolded state. ASTM D 3080-98 (ASTM, 2011) specifies the test protocol commonly used to perform the direct shear test in a laboratory. The direct shear test equipment consists of a direct shear box divided into two equal halves. The soil/aggregate material being tested is sheared by moving one-half of the box horizontally while keeping constant normal pressure acting on the top surface. The test specification requires a minimum specimen thickness of six times the maximum particle diameter, and a minimum specimen diameter or width of ten times the maximum particle diameter. However, experimental and numerical evidences have shown that this criterion may not provide the true soil friction angle because the specified sizes could still impede the full growth and propagation of the shear band inside the specimen (Wang and Gutierrez, 2010). From a practical point of

view, a smaller apparatus to particle-size ratio has great advantage because it reduces the size of the specimen required for testing; from a computational point of view, a smaller specimen size corresponds to fewer particles needing to be simulated, thus significantly reducing the computational efforts (Zhou et al., 2009). Typical specimen sizes selected by researchers for direct shear testing of railroad ballast are  $400\text{ mm} \times 400\text{ mm} \times 300\text{ mm}$  (Dissanayake et al., 2016), and  $300\text{ mm} \times 300\text{ mm} \times 200\text{ mm}$  (Indraratna et al., 2012; Ngo et al., 2014).

Although the direct shear test has several limitations such as (i) rigidity condition of the top loading plate, (ii) the peak friction angle mobilized in the horizontal shear plane leading to larger values compared to triaxial test results, shear strength test parameters obtained from direct shear tests are considered useful and practically straightforward. Moreover, this test method is adopted because of its simplicity and lower testing costs compared to other sophisticated test methods.

A schematic of the direct shear test set-up is presented in Figure 2.7. As shown in the figure, the square direct shear box has a dimension of  $300\text{ mm} \times 300\text{ mm} \times 200\text{ mm}$ . The box is divided into two equal halves having a height of  $100\text{ mm}$  each. The bottom half of the box is moved horizontally in the x-direction while a constant normal stress ( $\sigma_N$ ) is applied to the top surface. In the figure, the total horizontal displacement is denoted by  $x$ .

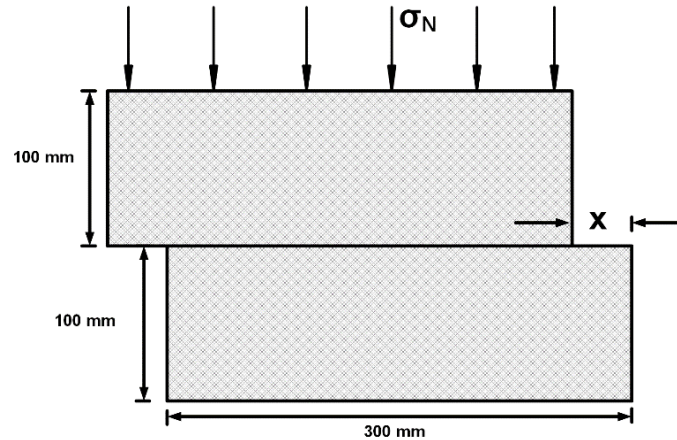


**Figure 2.7 Schematic Representation of the Direct Shear Test Setup**

#### 2.3.4.2 Triaxial Monotonic Shear Strength Testing

The triaxial test is one of the most versatile and widely performed geotechnical laboratory-tests for establishing the shear strength parameters for granular materials. The triaxial test is more complicated than direct shear testing as far as specimen preparation and equipment capabilities are concerned. Some advantages of triaxial testing over other simpler procedures are: (i) it includes the ability to control specimen drainage and take measurements of pore water pressures; and, (ii) the failure plane is not pre-defined as in direct shear testing. The triaxial procedure utilizes a cylindrical specimen of compacted soil/aggregate material that is confined along all the three directions. The test is conducted following stress paths that closely simulate the stress history of the sample in the field. As far as railroad ballast is concerned, triaxial test has been traditionally performed in the laboratory to evaluate the effects of field monotonic and repeated loading on ballast behavior (Anderson and Fair, 2008; Aursudkij et al., 2009; Indraratna et al., 2009; Lu and McDowell, 2010).

Most triaxial specimens have an approximate 2:1 height-to-diameter ratio. Owing to the large particle-size (often as large as 63 mm) of railroad ballast, significantly large specimens have to be tested in the laboratory for realistic estimation of the shear strength properties. For example, typical specimen sizes selected for triaxial monotonic shear strength tests are, 610 mm height  $\times$  305 mm diameter (Qian et al., 2013, 2015; Mishra et al., 2014a). A schematic of the stresses applied to the specimen in a triaxial test setup is shown in Figure 2.8.

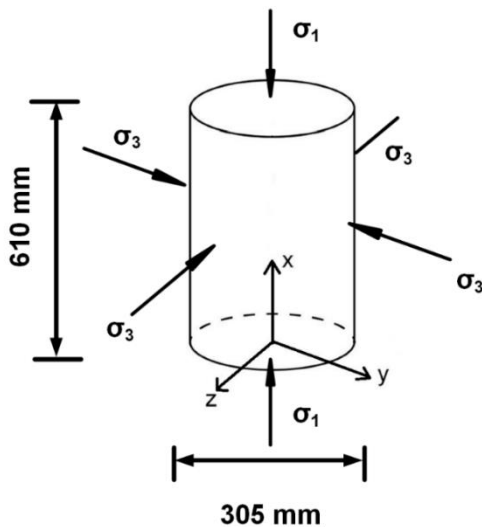


**Figure 2.8 Schematic Diagram of Triaxial Monotonic Shear Strength Test**

where

$\sigma_3 = \sigma_r$  = the confining (radial) stress (minor principle stress)

$\sigma_1 = \sigma_a$  = the axial stress (major principle stress) **(Equation 2.7)**

The shear strength parameters  $c$  and  $\phi$  can be obtained graphically from a Mohr-Coulomb plot of triaxial test results. To plot a Mohr circle from triaxial data  $\sigma_1$  and  $\sigma_3$  are obtained from the triaxial test and circle is drawn connecting the two points centered at

$\frac{\sigma_1 + \sigma_3}{2}$ . Plotting the results from three or more triaxial tests ( $\sigma_{1-A}, \sigma_{1-B}, \sigma_{1-C}, \sigma_{3-A}, \sigma_{3-B}, \sigma_{3-C}$ ) on the same graph, drawing the circles, and drawing a tangent to the circles constructs the failure envelope (Figure 2.9).

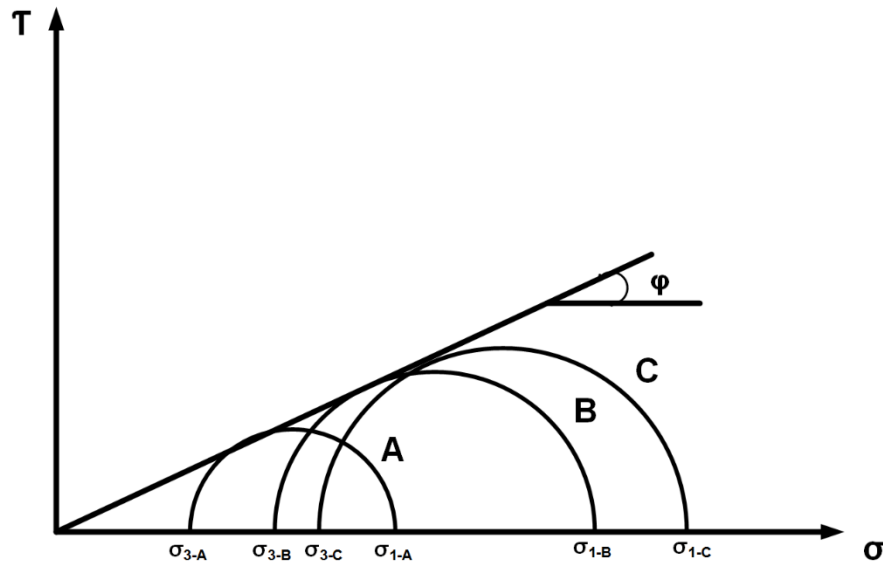


**Figure 2.9 Schematic Diagram of Mohr-Coulomb Plot**

### 2.3.5 Resilient Behavior of Railroad Ballast

The concept of resilient-modulus is commonly used to describe the response of pavement and railroad substructure layers under repeated loading. Hveem and Carmany (1948) and Hveem (1955) introduced the concept of resilient behavior. They highlighted the importance of resilient behavior in pavements, particularly in understanding the fatigue cracking of asphalt surfaces. As shown in Figure 2.10, the difference between the maximum strain under peak load and the permanent strain under unloaded condition is defined as the resilient strain. The resilient-modulus of a material is defined as the repeated deviator stress divided by the recoverable (resilient) axial strain during triaxial testing (Seed et al., 1962). Resilient modulus is an important parameter used for assessing

the structural response of track substructure layers under repeated loading. For example, the resilient properties of the subgrade have been shown to affect the degradation and rate of settlement of ballast (Raymond and Bathurst, 1987). Similarly, resilient modulus of the ballast layer is indicative of its ability to dissipate train-imposed stresses.

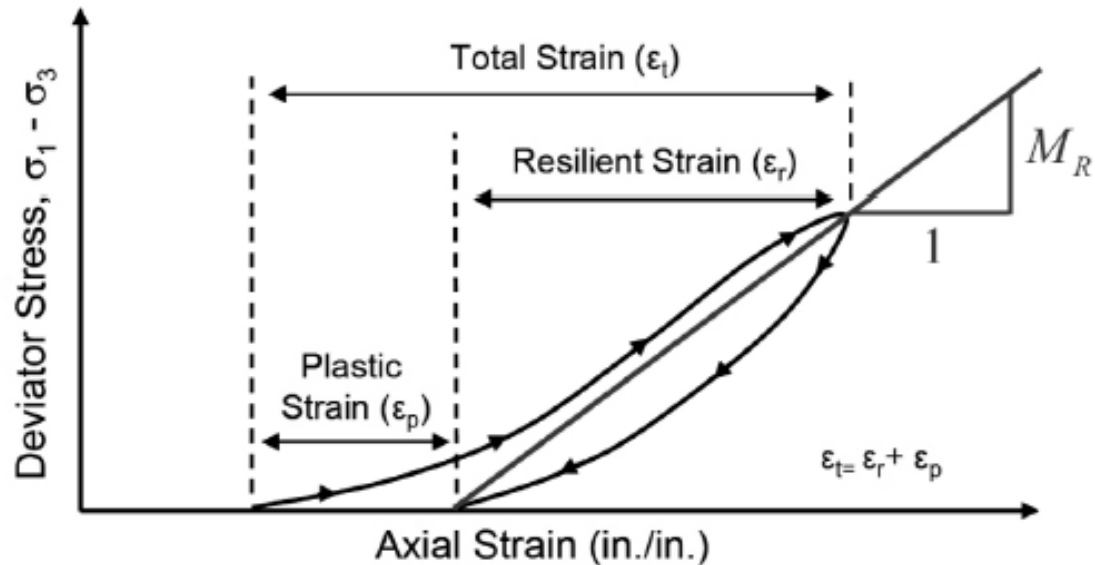


**Figure 2.10 Response of Granular Material Subjected to Triaxial Loading, and Measurement of Resilient-Modulus (Buchanan, 2007)**

The resilient-modulus of a granular material is affected by several factors, such as stress level, density, gradation, fines content, maximum grain size, aggregate type, particle shape, moisture content, stress history and number of load applications. As a stress-dependent material property, the resilient-modulus for an unbound granular layer increases considerably with increase in the confining pressure and bulk stress (Lekarp et al., 2000, Lackenby et al., 2007). Findings from repeated load triaxial tests on different granular materials conducted by Thom and Brown (1989) showed that at low strain, the resilient-modulus of granular material may be influenced by particle texture and that a correlation exists between elastic stiffness and surface friction of a material. Lackenby et

al. (2007) conducted a series of triaxial test on railroad ballast, and indicated that the resilient-modulus increased with increasing confining pressure, as shown in Figure 2.11. In-depth understanding of different factors affecting the resilient modulus of ballast will aid better design track structures comprising unreinforced or reinforced ballast layers.

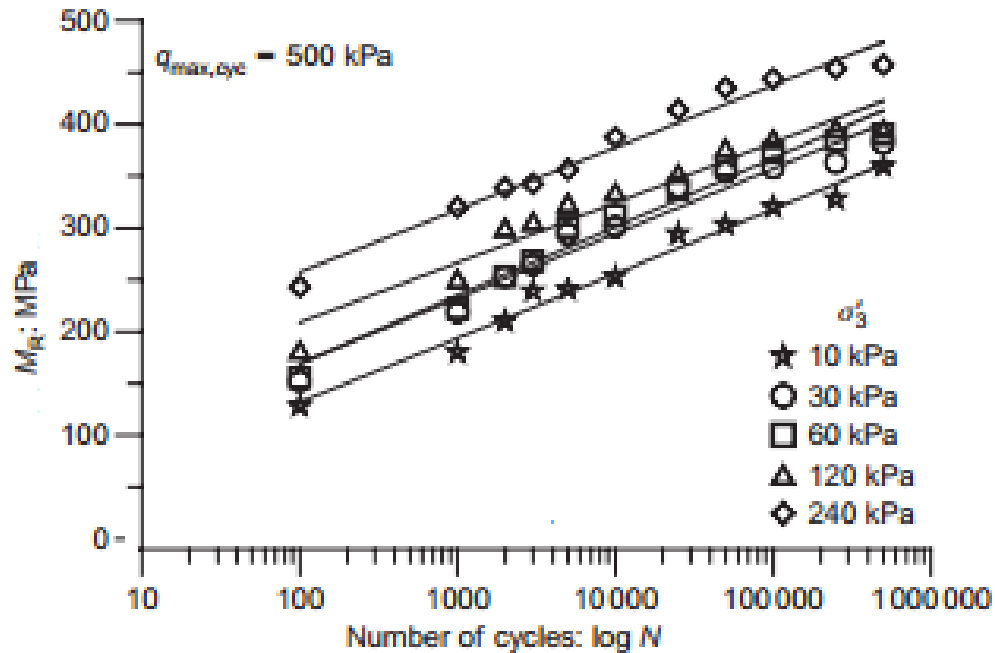


**Figure 2.11 Resilient-Modulus ( $M_R$ ) Response of Railroad Ballast under Different Stress States (after Lackenby et al., 2007)**

#### 2.4 Discrete Element Modeling of Granular Material

Conducting widely used laboratory-tests such as direct shear test and triaxial test on coarse-grained railroad ballast is often not feasible in standard geotechnical engineering laboratories due to the significantly large specimen and test set-up requirements. Moreover, due to inherent variabilities associated with specimen preparation and testing in the laboratory, parametric analyses of the test results through complete isolation of the

factor(s) of interest is often quite challenging. In such scenarios, numerical modeling and test simulation techniques are often adopted.

To describe the loading response of railroad ballast using numerical method, two main approaches can be employed: (1) continuum-based approaches such as the Finite Element Method (FEM); and (2) discrete methods such as Discrete Element Method (DEM). Due to the particulate nature of railroad ballast, its shear strength is primarily derived from particle-to-particle interaction at the granular level; this phenomenon can be better captured using DEM. The mechanics of granular materials can be analyzed at both micro and macro levels using DEM. DEM can simulate the interlocking effect between individual particles, the inherent characteristics of individual particles, and the influence of specimen porosity material behavior. In addition, it has the advantage of visual inspection of the failure plane during the shearing process. Another advantage of DEM-simulated tests over the laboratory testing is that once modeled, identical specimens can be reused for testing under different loading conditions; this is often not possible in the laboratory. Over the past few decades, DEM has been widely used by several researchers (Cundall and Strack, 1979; Rothenburg and Bathurst, 1989; Jenkins et al., 1989; Cheng et al., 2004; Lim and McDowell, 2005) to study the behavior of granular assemblies.

#### 2.4.1 Principles of Discrete Element Modeling

The Discrete Element Method (DEM), developed by Cundall in 1971 (Cundall and Strack, 1979), is a numerical method which can be used to study the motion of individual and independently moving objects. DEM allows finite displacements and rotations of discrete bodies, including complete detachment, and recognizes new contacts automatically as the calculation progresses (Cundall and Hart, 1992). As long as the

deformation of individual particles is small when compared to the deformation of the whole granular assembly, precise modeling of particle deformation is not required for obtaining a good approximation of the overall mechanical behavior. Note that this assumption generally holds true for unbound aggregates and railroad ballast, making DEM an adequate tool for studying the behavior of these materials.

In DEM, the contact forces and displacements within a particulate assembly can be found through a series of calculations by tracking the movement of individual particles. Newton's second law is used to calculate the motion of a particle because of the forces acting on it, and force-displacement law is used to find the contact forces from displacements (Cundall and Strack, 1979). Some elements come into contact and some separate at each time step during a DEM simulation. Performing this contact detection throughout the whole analysis is mandatory. For elements with simple shapes such as spheres or ellipses, contact detection can be performed analytically. However, this process of contact detection becomes significantly more involved as the shape of individual particles (discrete elements) deviates from simple shapes. Huge computational time and effort is required to calculate and update contact forces during a DEM simulation (Nezami et al., 2004). The basic components of a DEM simulation are schematically represented in Figure 2.12.

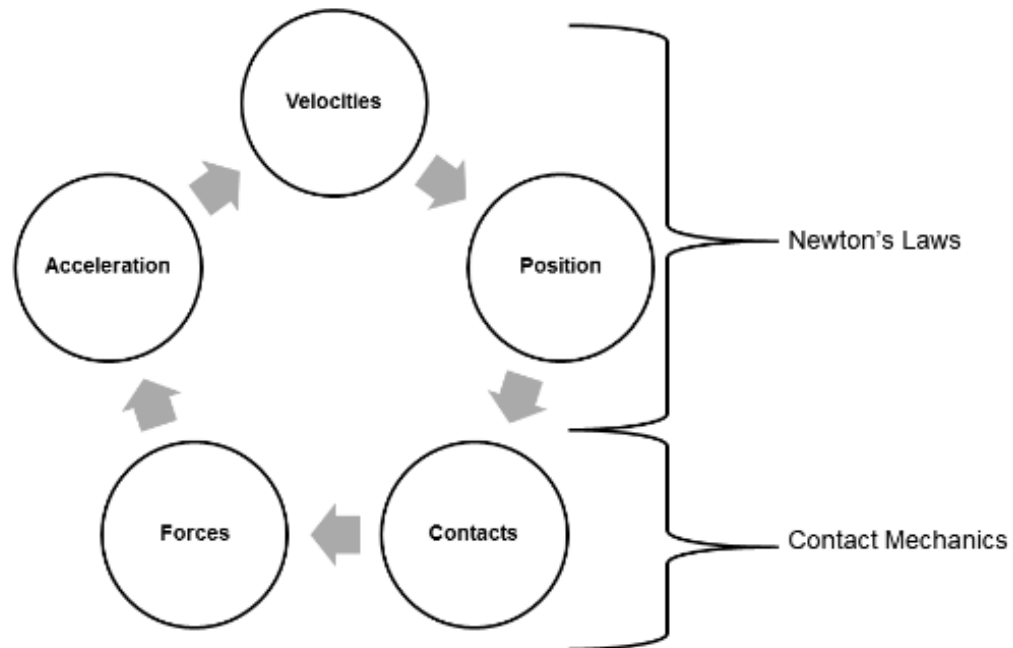


**Figure 2.12 Flow Chart Showing the Main Principles of DEM (adopted from What Is DEM Ebook, 2017)**

Several computer software programs such as BALL (Cundall and Strack, 1978), BLOCKS3D (Ghaboussi and Barbosa, 1990), EDEM (DEM Solutions, 2011), Particle Flow Code (PFC) (Itasca, 2016) and open source codes like Kratos (Santassusana Isach, 2013), LMGC90 (Dubois et al., 2011), Yade (Kozicki and Donzé, 2009), and LIGGGHTS<sup>®</sup> (by CFDEMresearch GmbH, 2017) are available for discrete element modeling. Considering that PFC is one of the most widespread general-purpose Distinct Element Modeling frameworks, this research effort used PFC for the DEM simulation tasks; a brief introduction and background on PFC is presented in the following section.

## **2.5 Introduction to PFC3D<sup>®</sup> as a DEM Tool**

The PFC3D<sup>®</sup> program provides a DEM framework that includes both a computational engine and a graphical user interface. A PFC3D<sup>®</sup> model is used to simulate the movement and interaction of a series of finite-sized rigid particles, which

interact at pair-wise contacts. The particles are assumed rigid, and the mechanical behavior of such a system is described in terms of the movement of each particle and the inter-particle forces acting at each contact point. Newton's laws of motion provide the fundamental relationship between particle motion and the forces causing that motion. PFC3D<sup>®</sup> can easily be customized and applied to a very broad range of numerical investigations where the discrete nature of the systems is of interest. PFC3D<sup>®</sup> is suitable for numerical modeling of the stress-strain response of granular materials such as aggregates and railroad ballasts, where the deformation results primarily from the sliding and rotation of the rigid particles and the interlocking at particle interfaces. It is also capable of simulating more complex behavior of granular materials by allowing the particles to be bonded together at their contact points, so that internal forces (i.e. tensile, shear or moment) are allowed to develop at the contacts.

#### 2.5.1 The PFC3D<sup>®</sup> Model

Some particle-flow model assumptions are provided below (Itasca, 2016):

1. The particles are treated as rigid bodies where the fundamental particle shape of is disk (in 2D); or sphere (in 3D), denoted as ball. However a more complex shape can be incorporated using the clump logic which supports the creation of rigidly attached disks (in 2D) or spheres (in 3D), denoted as pebbles. Each clump consists of a set of overlapping pebbles that act as a rigid body with a deformable boundary. Clumps may be of arbitrary shape.
2. Particles interact only at contacts (over a vanishingly small area) by means of an internal force and a moment. .

In order to set up a model to run a simulation with PFC3D<sup>®</sup>, four fundamental components of a problem must be specified (Itasca, 2016).

1. The model domain: it is an axis-aligned bounding box within which, all model components exist;
2. An assembly of particles: consists of the locations and size distribution of particles;
3. Contact behavior and material properties: these dictate the type of response the model will display upon disturbance. The choice of appropriate energy dissipation mechanisms is crucial at this stage; and
4. Boundary and initial conditions: these define the in-situ state (i.e., the condition before a change or disturbance in the problem state is introduced).

The PFC model consists of bodies, pieces, and contacts. The three basic entities include ball, clump, and wall. Each body is composed of one or more pieces. The internal force and moment ( $F_c$  and  $M_c$ ) act at the contact location in an equal and opposite sense on the two pieces (Figure 2.13). However, contacts may not form between two walls. Thus, contacts are either ball-ball, ball-pebble, pebble-pebble, ball-facet, or pebble-facet (Itasca, 2016). The balls, clumps, and walls interact with one another via forces that arise at contacts. Equations of motion are satisfied for each ball and clump. The compaction and confinement of the simulated granular material (as balls or clumps) is achieved through applying velocity boundary conditions using the surrounding walls.

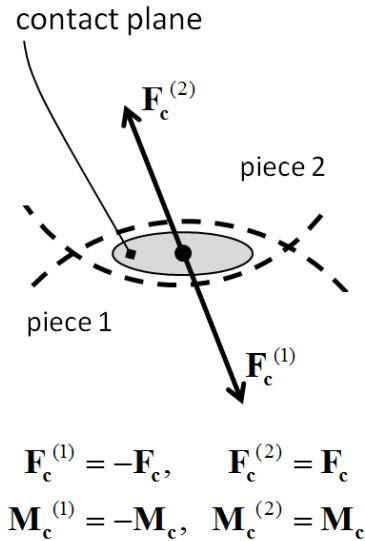


**Figure 2.13 Internal Force and Moment Acting on the Two Pieces at a Ball-Ball Contact (Itasca, 2016)**

In the PFC model framework, all deformation occurs at the contacts between the rigid bodies. It is mandatory to assign contact models that define the behavior at contacts that form between the particles and facets. The contact-model formulation provides a force-displacement law relating the generalized internal force to the relative motion at the contact. PFC can incorporate the following contact models: linear, linear contact bond, linear parallel bond, hertz contact, hysteretic contact, smooth-joint contact, flat joint, rolling resistance linear, burger's model, and hill contact model (Itasca, 2016). The behavior of each contact type is defined by a contact model.

### 2.5.2 Cycling Sequence

PFC uses an explicit time-marching method to solve the algebraic equations where the solution is reached after a series of computational steps. Figure 2.14 illustrates the simplistic representation of the primary operations that occur during each calculation cycle.

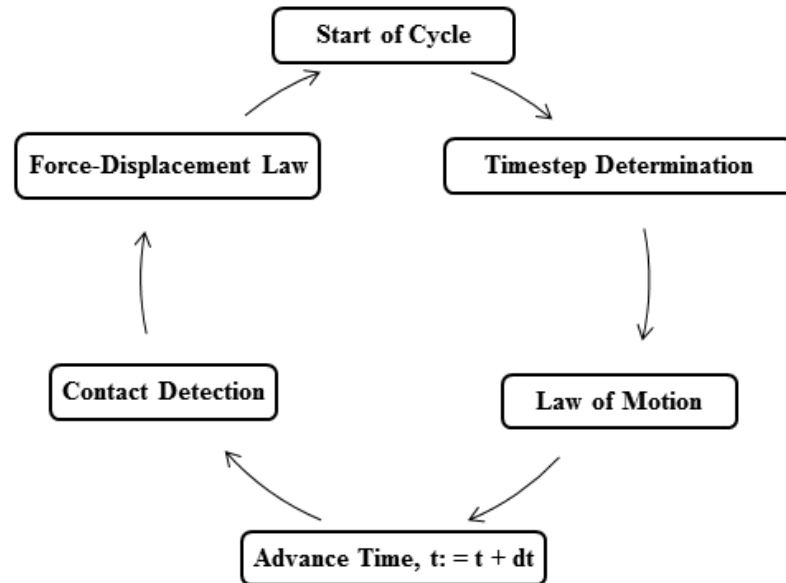


**Figure 2.14 Sequence of Primary Operations that Occur during Each Simulation Cycle, Termed as the Cycle Sequence (adopted from Itasca, 2016)**

As shown in the figure, at the start of each timestep, the contacts are updated from the particle and wall positions. The force-displacement law is then applied to each contact to update the contact forces based on the relative motion between the two contacted entities and the contact constitutive model. Subsequently, the law of motion is applied to each particle to update its velocity and position based on the resultant force and moment acting on it. Similarly, wall positions are updated based on specified wall velocities. Custom criteria may be specified to terminate a series of cycles based on the current model state. Multiple solve limits can be specified simultaneously. Once at least one of the solve limits has been met, the cycling is terminated.

#### 2.5.2.1 Force-Displacement Law

The linear model consisting of linear springs and dashpots corresponds with the model developed by Cundall and Strack (1979). At the start of each cycle, the force-displacement law is applied to each of the contacts in order to obtain new contact forces.

The contact force vector  $F_i$  can be resolved into normal and shear components with respect to the contact plane as expressed in Equation 2.8.

$$F_i = F_i^n + F_i^s \quad \text{(Equation 2.8)}$$

where  $F_i^n$  and  $F_i^s$  denote normal and shear components of the contact force vector, respectively. The force-displacement law relates these two components of force to the corresponding components of the relative displacement via the normal ( $k_n$ ) and shear stiffness ( $k_s$ ) at the contact. The normal contact force vector is calculated by:

$$F_i^n = K^n U^n n_i \quad \text{(Equation 2.9)}$$

where  $K^n$  = the normal stiffness,  $U^n$  = the overlapping displacement magnitude of two contacting entities and  $n_i$  = the unit normal vector. The orientation of the normal vector depends on the element type used; (i) for ball-to-ball contact, the normal vector is directed along the line between ball centers, and (ii) for ball-to-wall contact, normal vector is directed along the line defining the shortest distance between the ball center and the wall. The shear contact force is however computed in an incremental fashion. When the contact is formed, the total shear contact force is initialized to zero. Relative shear displacement at the contact point of two contacting pieces will result in an increment in shear force. The shear force-increment vector is calculated by:

$$\Delta F_i^s = -K^s V_i^s \Delta t \quad \text{(Equation 2.10)}$$

where  $K^s$  = the shear stiffness [force/displacement] at the contact and  $V_i^s$  = the shear component of the contact velocity and  $\Delta t$  = the timestep. Finally, the new shear contact force is calculated by summing the previous shear force vector existing at the start of the timestep with the shear elastic force-increment vector (see Equation 2.11).

$$F_i^s = \{F_i^s\}^{[previous]} + \Delta F_i^s \quad \text{(Equation 2.11)}$$

### 2.5.2.2 Law of Motion

The motion of a single particle is governed by the resultant force and moment vectors acting upon it. The equations of motion can be expressed as two vector equations. One of the equations of motion relates the resultant force to the translational motion, as:

$$F_i = m \left( \ddot{x}_i - g_i \right) \quad \text{(Equation 2.12)}$$

where  $F_i$  = the resultant force or the sum of all externally applied forces acting on the particle;  $m$  = the mass of the particle;  $\ddot{x}_i$  = the acceleration of a particle;  $g_i$  = the body force acceleration vector (the gravitational loading). The fundamental equation of rotational motion for a rigid body is:

$$L_i = I \omega_i \quad \text{(Equation 2.13)}$$

where  $L_i$  = the angular momentum;  $I$  = the inertia tensor;  $\omega_i$  = the angular velocity.

At each timestep, the equations of motion given by Equations 2.12 and 2.13 are integrated to get updated velocities and new positions for each particle in a timestep of  $\Delta t$ . The translational velocity ( $\dot{x}_i$ ) and angular velocity ( $\omega_i$ ) are computed at the mid-intervals of  $(t \pm \frac{n\Delta t}{2})$ , where (n) is a positive integer. The position ( $x_i$ ), translational acceleration ( $\ddot{x}_i$ ), angular acceleration ( $\dot{\omega}_i$ ), resultant force ( $F_i$ ) and resultant moment ( $M_i$ ) are computed at the primary intervals of  $(t \pm n\Delta t)$ .

$$\ddot{x}_i^{(t)} = \frac{1}{\Delta t} \left( \dot{x}_i^{(t+\frac{\Delta t}{2})} - \dot{x}_i^{(t-\frac{\Delta t}{2})} \right) \quad \text{(Equation 2.14)}$$

$$\dot{\omega}_i^{(t)} = \frac{1}{\Delta t} \left( \omega_i^{(t+\frac{\Delta t}{2})} - \omega_i^{(t-\frac{\Delta t}{2})} \right) \quad \text{(Equation 2.15)}$$

Inserting these expressions (Equation 2.14 and 2.15) into Equation 2.12 and 2.13 and solving for the velocities result in:

$$\dot{x}_i^{(t+\frac{\Delta t}{2})} = \dot{x}_i^{(t-\frac{\Delta t}{2})} + \left( \frac{F_i^{(t)}}{m} - g_i \right) \Delta t \quad \text{(Equation 2.16)}$$

$$\omega_i^{(t+\frac{\Delta t}{2})} = \omega_i^{(t-\frac{\Delta t}{2})} + \left( \frac{M_i^{(t)}}{I} \right) \Delta t \quad \text{(Equation 2.17)}$$

Finally, the position of the particle center is updated using velocities as follows:

$$x_i^{(t+\Delta t)} = x_i^{(t)} + \dot{x}_i^{(t+\frac{\Delta t}{2})} \Delta t \quad \text{(Equation 2.18)}$$

### 2.5.3 Contact Constitutive Models

A simple constitutive model consisting of a stiffness model, a slip model and a bonding model acting at contacts simulates the constitutive behavior of a material in PFC3D<sup>®</sup>. The ‘Stiffness Model’ provides an elastic relationship between the contact forces and displacements using the Force-Displacement Law.

#### 2.5.3.1 Stiffness Model

The stiffness model relates the contact forces and relative displacements in the normal and shear directions via the force-displacement law. Two types of contact stiffness models can be incorporated in PFC3D<sup>®</sup>: (i) linear model, and (ii) Hertz-Mindlin model.

The linear contact-stiffness model, which is defined by the normal ( $k_n$ ) and shear stiffness ( $k_s$ ) of two contacting entities (ball to ball or ball to wall), assumes that the stiffness of the two contacting entities act in series. The contact stiffness for the linear contact model can be calculated using the following equations.

$$K^n = \frac{K_n^{[A]} K_n^{[B]}}{K_n^{[A]} + K_n^{[B]}} \quad \text{(Equation 2.19)}$$

$$K^s = \frac{K_s^{[A]} K_s^{[B]}}{K_s^{[A]} + K_s^{[B]}} \quad \text{(Equation 2.20)}$$

where the superscripts  $[A]$  and  $[B]$  denote the two entities in contact.

The simplified Hertz-Mindlin model is defined by the elastic properties of the two contacting balls: i.e. shear modulus ( $G$ ) and Poisson's ratio ( $\nu$ ). For the Hertz-Mindlin model in PFC3D<sup>®</sup> model, the normal and shear stiffness are ignored, and walls are assumed to be rigid. Hence, only the elastic properties of the ball are used for ball-to-wall contacts, and the mean values of the elastic properties of the two contacting balls will be used for the ball-to-ball contacts. Moreover, tensile force is not defined in Hertz-Mindlin model meaning the model is not compatible with any type of bonding model. It should also be noted that, contact between a ball with the linear model and a ball with the Hertz model is not allowed within PFC3D<sup>®</sup>.

### 2.5.3.2 Slip Model

The slip model limits the shear force between two contacting entities where balls and walls can each be assigned a friction coefficient ( $\mu$ ) at the contact. The slip model is deactivated in the presence of a contact bond and automatically activated when the bond

breaks. The maximum elastic shear force ( $F_s^{\max}$ ) that the contact can sustain before sliding occurs is given by:

$$F_s^{\max} = \mu |F_i^n| \quad \text{(Equation 2.21)}$$

where  $F_i^n$  is the normal force at the contact.

### 2.5.3.3 Bonding Model

PFC3D<sup>®</sup> allows particles to be bonded together at contacts. The bonded model serves to limit the total normal and shear forces that a contact can carry by enforcing bond strength limits. Two bonding models are supported in PFC3D<sup>®</sup>: (i) contact bond model, and (ii) parallel bond model. Once a bond is formed at a contact between two particles, the contact continues to exist until the bond is broken.

A contact bond can be envisaged as a pair of elastic springs with specified constant normal and shear stiffness acting at the contact point. The contact bond breaks when the contact force exceeds either the normal contact bond strength or the shear contact bond strength. The particles bonded together with a contact bond cannot slip but they can roll over each other. On the contrary, a parallel bond can be envisaged as a disc of elastic glue lying on the contact plane. The parallel bond can transmit both forces and moments between particles, while contact bonds can only transmit forces acting at the contact point. The parallel bond breaks when the stress in any part of the bond exceeds the parallel bond strength. The linear parallel bond model can have two states: bonded, and unbonded. In the unbonded state, linear model exists between the two entities of PFC3D<sup>®</sup> model.

## 2.6 Use of Geosynthetics in Transportation Structures

It is desirable that once built, transportation structures such as pavements and railroads should perform well during their entire design life and limited maintenance activities should be required throughout this period. Therefore, ensuring adequate performance of these systems, while at the same time controlling the lifecycle cost is the primary challenge in front of transportation engineers. Use of geosynthetics could be very useful in this purpose. Geosynthetics are products manufactured from plastics, and are used in conjunction with soils and aggregates in construction of transportation structures such as railroads and pavements. Examples of different geosynthetic materials include geotextiles (woven and non-woven); geomembranes; geogrids; geonets; geowebbs and geocomposites. Among all the geosynthetic types stated above, the concept of geogrid reinforcement of railroad ballast has been described in the following subsections.

### 2.6.1 Introduction to Geogrids

In the 1950's, Dr. Brian Mercer developed the Netlon<sup>®</sup> process in which, plastics were extruded into a net-like process in one stage (Das, 2010). He founded Netlon Ltd. in the United Kingdom in 1959. They were the first manufacturer of geogrids. Based on Dr. Mercer's further innovative research and development work on extruded net technology, some polymer straps and strips were formed into grid-like products during the 1970's. The first integral geogrids were developed in the late 1970's. In 1982, the Tensar Corporation (presently Tensar International) introduced geogrids in the United States (Tensar<sup>®</sup> Geogrids, 2017).

Koerner (1998) defines a geogrid as a geosynthetic material consisting of connected parallel sets of tensile ribs with apertures of sufficient size to allow strike-

through of surrounding soil, stone, or other geotechnical material. Geogrids are made from polymeric materials (mostly high-density polyethylene, polypropylene, or polyester).

#### 2.6.1.1 Primary Functions

Das (2010) discussed the primary functions of geogrids to be: (i) reinforcement and (ii) separation. Reinforcement refers to the mechanism of mechanically improving the engineering properties of composite soil/aggregate, whereas separation it refers to the physical isolation of dissimilar materials (for example: ballast and sub-ballast or sub-ballast and subgrade) so that they do not commingle.

Ballast reinforcement using geogrids improves its structural response under loading, limits lateral movement of aggregate particles, and reduces vertical settlement through effective geogrid–aggregate interlocking. This is achieved through improved shear strength and resilient modulus properties. . Walls and Galbreath (1987) showed that, the periods between maintenance operations in railroads could be increased by as much as 12 times by the application of geogrid reinforcement to the ballast. During railroad track applications, geogrids can be placed either within the subballast or within the ballast layer. The position geogrid within the ballast layer is often dictated by the length of tamping tines, with the primary objective being to prevent damage to the geogrid layer during tamping operations.

#### 2.6.1.2 Types of Geogrid

Geogrids have longitudinal and transverse ribs, which form apertures that interlock with the surrounding aggregate particles. The interlocking between geogrid and aggregate forms a confined zone below and above the geogrid (Love, 1984; Haas et al.,

1988; Giroud and Han, 2004; Brown et al., 2007). The aperture shape might be square, rectangular or triangular. Geogrids with square or rectangular apertures are often referred to as biaxial geogrids, because their tensile strength and stiffness values are mobilized mainly along two directions (i.e., machine and cross-machine directions).

According to McGown et al. (2005), there are two classes of geogrid reinforcement: (i) uniaxial geogrids, which develop tensile stiffness and strength primarily in one direction; (ii) biaxial geogrids, which develop tensile stiffness and strength in two orthogonal directions. Apart from these, woven geogrids, welded geogrids and triaxial geogrids are also commercially available in different countries. Typical geogrids manufactured commercially are shown in the Figure 2.15.

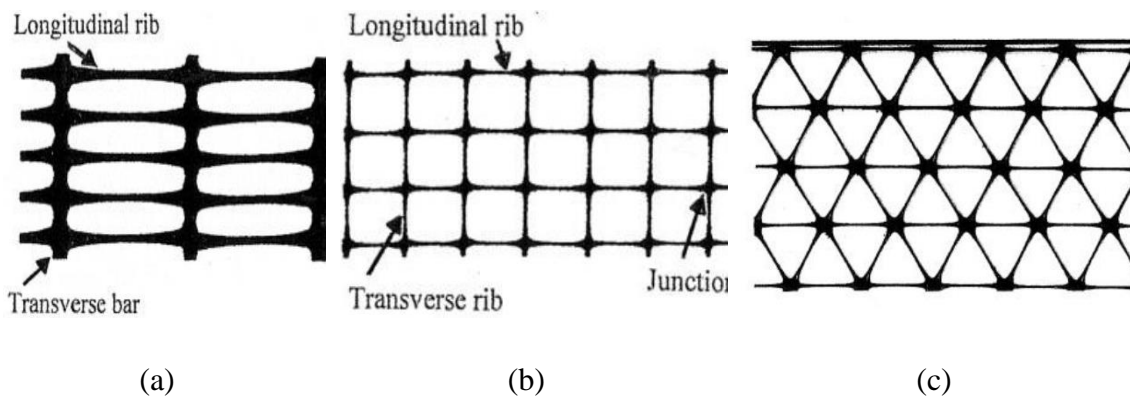


**Figure 2.15 Schematics Illustrating Typical Geogrid Types: (a) Uniaxial Geogrid; (b) Biaxial Geogrid; (c) Triaxial Geogrid (Das, 2010)**

### 2.6.1.3 Mechanism of Geogrid Reinforcement

When an unbound aggregate layer is placed on top of the geogrid, the coarser particles partially penetrate through the apertures and lock into position; this effect is commonly referred to as mechanical interlock, which leads to lateral confinement of the unbound aggregate, and a general stiffening of the layer (Penman and Priest, 2009). The mechanism of interlock in geogrids is shown in Figure 2.16. Different factors affecting

the interlocking between geogrids and aggregate particles are aggregate size and shape properties, geogrid types and properties, compaction efforts during installation, and loading conditions (Qian et al., 2014).

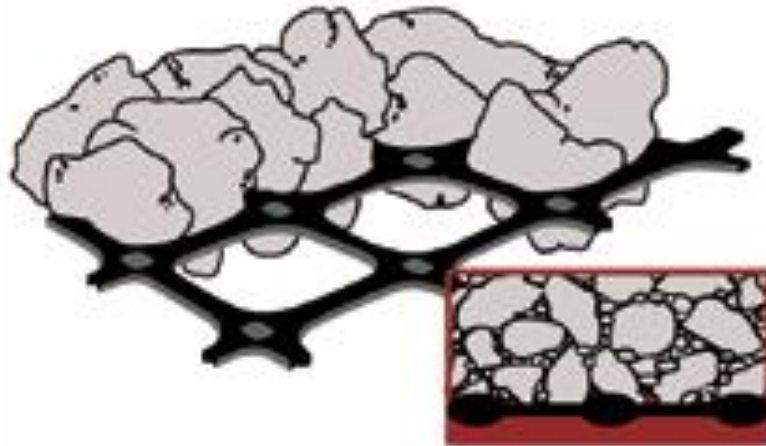


**Figure 2.16** A Schematic Illustrating the Mechanism of Aggregate-Geogrid Interlocking (after Penman and Priest, 2009)

#### 2.6.1.4 Geogrid Reinforcement of Railroad Ballast and Subballast Layers

The use of geogrid reinforcement in the subballast and ballast layers has gained widespread acceptance in many parts of the world. For example, in the United Kingdom, the national rail authority (Network Rail) has been using geogrids beneath its main line tracks since the early 1990s (Penman and Priest, 2009). On the other hand, national rail authorities in some European countries have gone so far as to providing formal guidance on the use of geogrids in their own design codes. In the United States, formal guidance on the use of geogrids in rail applications has been provided by AREMA.

The benefits of geogrid reinforcement have been highlighted by several laboratory research efforts, numerical simulations, as well as field implementation programs (Bathurst and Raymond, 1987; Indraratna et al., 2006; Brown et al., 2007; Tutumluer et al., 2009; Mishra et al., 2014a). Results from a full-scale experimentation program at the

University of Nottingham, UK aimed at investigating the potential for wider and improved use of geogrid reinforcement of ballast to reduce track settlements have been described briefly in the following paragraphs.

The primary objectives of the above-mentioned research effort were to reduce track settlement rates, and to understand how grids interact with the ballast particles under moving wheel loads. A special apparatus, known as the Composite Element Test (CET), was designed to study the development of settlement under simplified full-scale conditions representative of the field situation. The ballast used in this study was a uniformly graded, crushed hard stone which was durable, angular, equidimensional in shape and relatively non-flaky. A variety of geogrids with different aperture sizes and tensile strengths were used. It should be noted that, all the geogrids had square apertures (Brown et al., 2007). Key findings from this study were: (i) the presence of geogrids reduced settlement; (ii) for a ballast material with 50 *mm* maximum particle-size, the desired geogrid aperture size should be 60 to 80 *mm*; (iii) within the range of optimum dimension (60 to 80 *mm*) for two grids having same tensile strength but different aperture sizes, the geogrid with greater aperture size perform better for minimizing settlement, this suggests a lack of interlock with the aggregate particles in case of the relatively small aperture size. These results confirmed the potential of geogrids for reducing the frequency of track maintenance operations.

### 2.6.2 Introduction to Geogrid Gain Factor

Note that most of the research studies cited above focused on studying the effect of geogrids on ballast shear strength and/or permanent deformation behavior. Potyondy et al. (2016) proposed the ‘Geogrid Gain Factor’ concept to quantify the structural benefits

of geogrid inclusion in unsaturated granular layers. The geogrid gain factor was introduced as a means to modify the Minnesota Department of Transportation's pavement design program (MnPAVE) to account for the presence of geogrid within aggregate base layers (Siekmeier et al., 2016). The geogrid gain factor is defined as the ratio of resilient-modulus of the aggregate base with geogrid to resilient-modulus of the aggregate base without geogrid. The estimation of geogrid gain factor has been carried out using numerical (PFC3D<sup>®</sup>) modeling of repeated load triaxial tests of an aggregate base, both with and without geogrid. The current master's thesis effort extends the concept of geogrid gain factor to railroad ballast reinforcement.

## **2.7 Summary**

This chapter presented findings from an extensive review of published literature on topics pertinent to the research objectives. First, an overview of conventional ballasted railroad track components was presented, followed by an overview of ballast functions and properties. The objective was to identify factors that would affect the performance of a ballast layer as the primary load bearing component in ballasted railroad tracks. Subsequently, different tests to characterize the stress-strain behavior of railroad ballast pertinent to the response of railroad track under loading and potential problems in performing those tests in standard laboratory were discussed. The Discrete Element Method (DEM) was then presented as a logical alternative to model the behavior of particulate media such as railroad ballast. The Particle Flow Code (PFC) was introduced as a software tool for Discrete Element Modeling of granular materials. Finally, a brief discussion on geogrid reinforcement of railroad ballast was presented. The primary focus was to identify the factors that affect the mechanism of geogrid-ballast interaction.

The next chapter (Chapter 3) of this thesis document will present findings from DEM simulations of direct shear testing of railroad ballasts.

## CHAPTER 3: DISCRETE ELEMENT MODELING OF DIRECT SHEAR STRENGTH TEST ON RAILROAD BALLAST

### 3.1 Introduction

This chapter presents findings from DEM simulations of direct shear testing of railroad ballasts undertaken within the scope of this Master's Thesis effort. First, details on the procedure adopted to simulate direct shear testing of railroad ballast have been presented. The discussions include considerations related to specimen size selection, specimen preparation, test variable selection, etc. This is followed by analyses of typical stress-strain curves generated through these simulated tests, and their comparisons against laboratory-test data obtained from the literature. Subsequently, results from parametric analyses conducted to study the effects of different material, specimen and test parameters on ballast shear strength response have been presented. A new gradation parameter termed as "Coarse-to-Fine Ratio" (C/F Ratio) has been introduced as an indicator of packing conditions within the ballast matrix, and the effect of this parameter on ballast shear strength has been analyzed. Finally, limitations associated with the current modeling approach have been discussed, with suggestions for improvements.

### 3.2 DEM Simulation of Direct Shear Test (DST)

DEM simulation of Direct Shear Test has been widely used to study the shear strength behavior of granular materials (Ni et al., 2000; O'Sullivan et al., 2004; Liu, 2006; Yan, 2009; Jo et al., 2011; Indraratna et al., 2009; 2012; Kang et al., 2013; Kim et al., 2014, 2016; Ngo et al., 2014, 2015; Wang et al., 2015). Brief discussion on the direct

shear testing procedure in the lab was provided in Section 2.3.4.1. The approach adopted in the current study for DEM simulation of Direct Shear Tests on railroad ballast has been described in the following subsections.

### 3.2.1 Specimen Preparation and Testing

The first step in DEM simulation of any laboratory test procedure requires defining the particle shape and size distribution, specimen geometry and dimensions, as well as the loading conditions. Once a “primary” specimen is created and tested under simulated loading conditions, the resulting stress-strain curve is compared against actual laboratory test results, and different model parameters are adjusted in an effort to calibrate the numerical model. Subsequently, different specimen and test parameters can be changed during parametric analyses to quantify their individual effects on the test results.

#### 3.2.1.1 Ballast Shape Used

Ballast particles in DEM simulation can be represented as: (a) spheres (Lim and McDowell 2005, Lu and McDowell 2007); (b) clumps (Indraratna et al., 2012; Ngo et al., 2014, 2015; Wang et al., 2015); or (c) polyhedral particles (Huang et al, 2009; Qian et al., 2013). Decisions regarding the particular approach to use are primarily dependent on (1) capabilities of the modeling software used, and (2) nature of the granular assemblies being modeled. PFC, the modeling software used in the current study, is based on spheres as the primary building block for 3D simulations. Accordingly, this study has used spheres and “clumps” for conducting the parametric analysis on ballast shear strength behavior. Note that the sphere is a simplistic representation of a typical railroad ballast particle, whereas, the clumps approach relies on combining multiple spheres of different sizes to simulate complex-shaped particles (over-lapping among different particles is

allowed). Although the clumps approach has been widely used by researchers to simulate complex particles, it is important to note that this is not the same as simulating “true” polyhedral particles. The clumps in this study were generated using two different approaches inherent to PFC3D<sup>®</sup> (1) using the ‘*pebcalculate*’ command, and (2) using the ‘*surfacecalculate*’ command.

Generation of Clumps Using the “*Pebcalculate*” Command: In this approach, (i) first, different clump templates having the desired radius values are created using one pebble (single sphere), and the volume of each of the templates is calculated; (ii) next, clumps (equal in number as the number of templates generated in the first step) are created with the desired number of pebbles (i.e. 2-ball, 4-ball, 8-ball or any n-ball) and radius values; (iii) the diameters of the clumps created during the second step are scaled so that the volume of a single sphere and the corresponding n-ball clump are the same. Once created, the clumps are distributed into the box targeting the desired porosity and volume fraction maintaining the size distribution. The particle shapes created in this study using the ‘*pebcalculate*’ feature were named as: (1) 2-ball clump, (2) 4-ball clump, and (3) 8-ball clump (see Figure 3.1). Among these clump shapes, the 2-ball clump had the least angularity whereas the 8-ball clump had the highest angularity. The properties of the clump shapes are listed in Table 3.1. Note that the “visual” approach by Lees (1964) (as shown in Figure 2.6) was used as a guideline in this research study to simulate particle geometries.

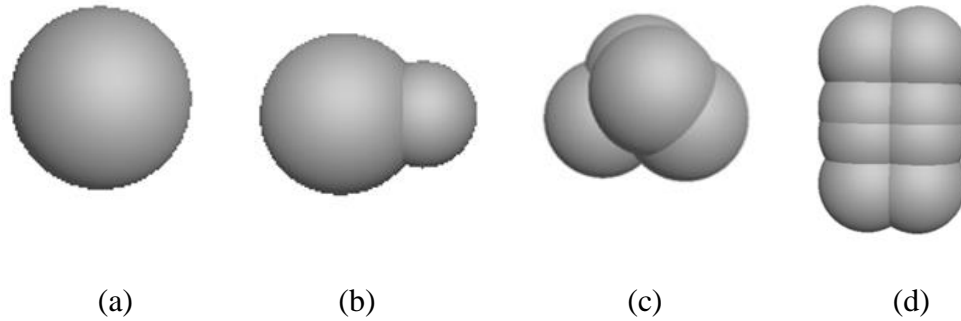


**Figure 3.1 Ballast Particle Shapes used for Discrete Element Modeling of Direct Shear Strength Tests in the Current Study: (a) Spherical; (b) 2-ball clump; (c) 4-ball clump; and (d) 8-ball clump**

**Table 3.1 Relative Radius Magnitudes Associated with Different Ballast Shapes used in the DEM Simulations of DST**

Ballast Particle Shape	Radius of Balls in the Clump
Single Sphere	$R_0$
2-ball clump	$R_1 = R_0 * 0.94$ ; $R_2 = R_0 * 0.625$
4-ball clump	$R_1 = R_0 * 0.705$
8-ball clump	$R_1 = R_0 * 0.588$

\*where  $R_0, R_1, R_2$  : Ball radius values specified in different clump templates

Generation of Clumps Using the “Surface-Calculate” Command: In this approach, desired ballast shapes were first modeled using a computer aided drawing software. Subsequently, the representative shapes were imported as geometries into the PFC3D<sup>®</sup> environment. Clump templates were created from the imported geometry file using the ‘bubble-pack’ algorithm. These clump templates were then used to generate the desired number of clumps. Figure 3.2 and Figure 3.3 present images of particle shapes generated using the ‘surfacecalculate’ feature in PFC3D<sup>®</sup> to represent particles with different F&E ratios and degrees of angularity, respectively. Between the two approaches

of clumps generation, more realistic shape of the ballast particles can be simulated using this approach.

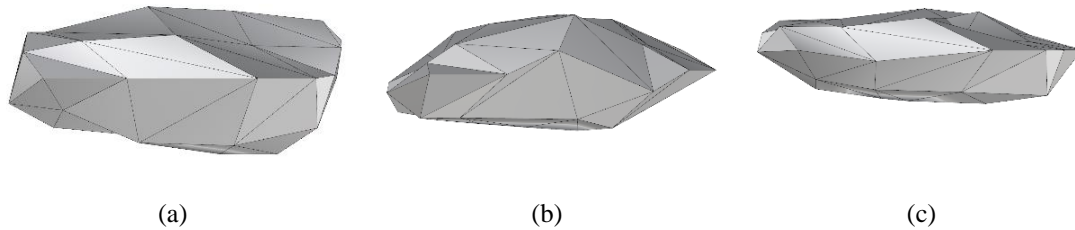


**Figure 3.2** Ballast Shapes Generated Corresponding to Different Flat and Elongated Ratio Values (a) F&E = 2.3; (b) F&E = 3.0; (c) F&E = 3.5

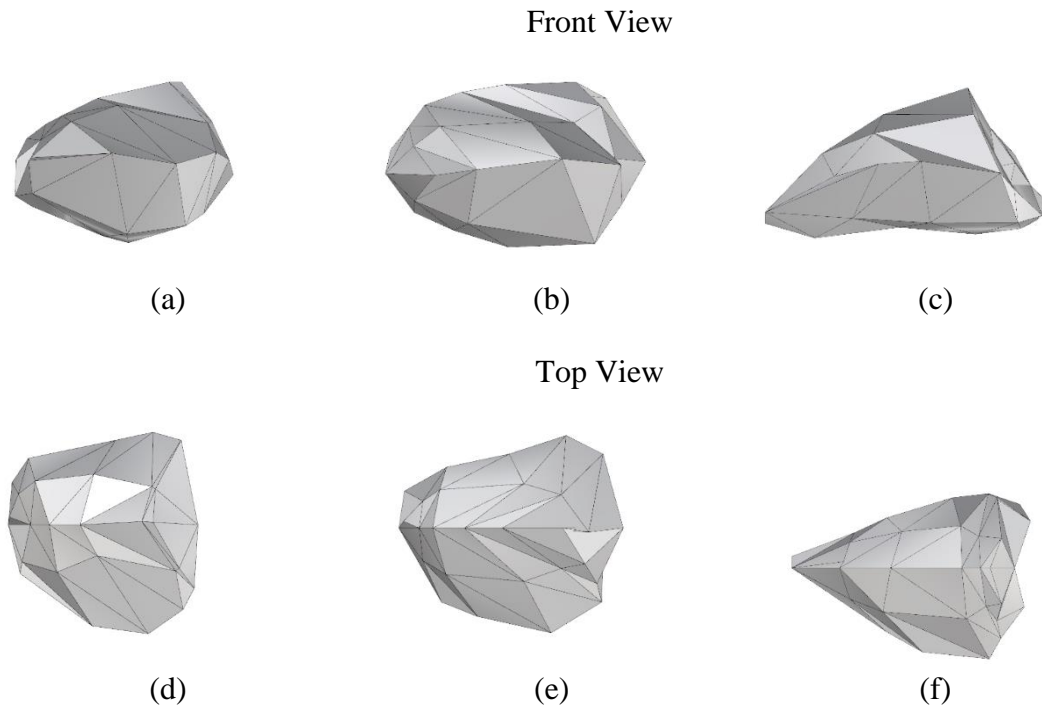


**Figure 3.3** Ballast Shapes Generated Corresponding to Different Angularity Values: Front View of (a) A = 300 to 399; (b) A = 600 to 699; (c) A = 900 to 999; Top View of (d) A = 300 to 399; (e) A = 600 to 699; (f) A = 900 to 999

Note that by increasing the number of pebbles (balls), the desired shape could be matched very closely with the geometries imported (see Figure 3.4). However, the use of

increased number of pebbles also leads to significantly increased computational times. Therefore, in this study, the number of balls assembled to create individual clumps was limited to approximately 20.

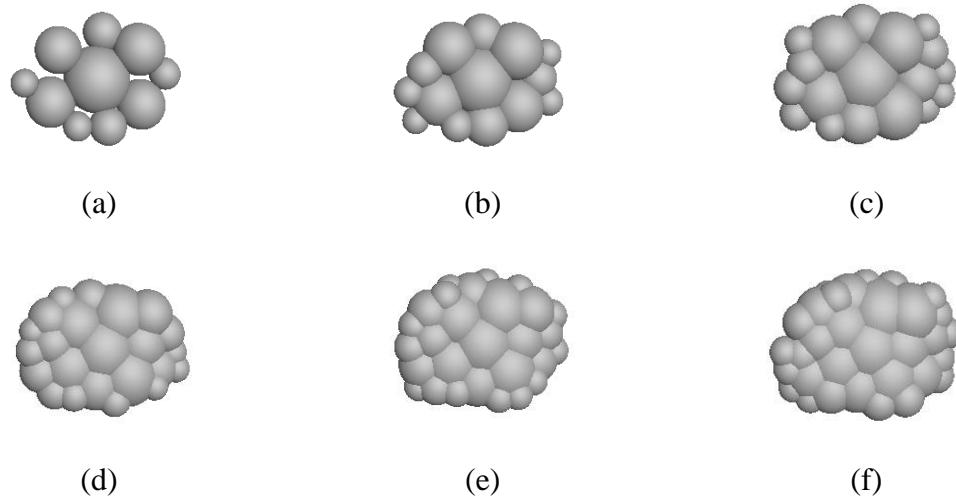


**Figure 3.4 Ballast Shapes Generated using Different Number of Pebbles (NOP) per the “Surface-Calculate” Command: (a) NOP = 10; (b) NOP = 15; (c) NOP = 20; (d) NOP = 25; (e) NOP = 30; (f) NOP = 34**

#### 3.2.1.2 Ballast Gradations Used

The ballast gradations simulated in this study correspond to typical gradations specified by AREMA, denoted as AREMA #4, and AREMA #24. One of the primary objectives of this research effort was to evaluate the effect of particle-size distribution characteristics on ballast shear strength. Accordingly, different particle-size distributions conforming to typical AREMA-specified gradations were created, and tested for shear strength properties through simulated shear strength tests. Figure 3.5 shows the gradation curves for different ballast materials tested in this research effort. Table 3.2 lists the percent passing individual sieve sizes for the different ballast gradations modeled.

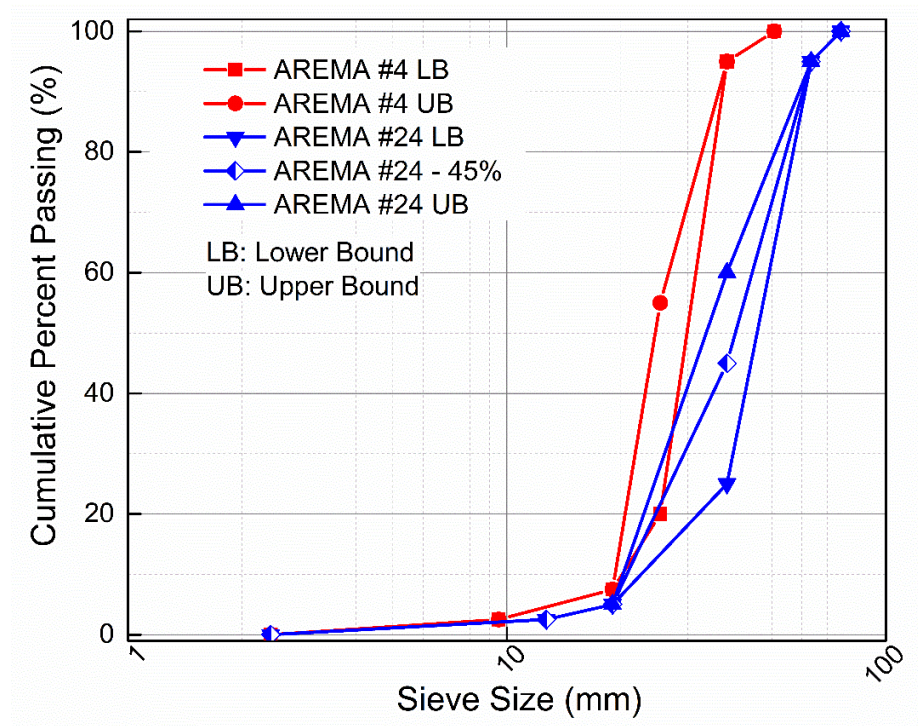


**Figure 3.5 Ballast Gradations Used for Direct Shear Tests in this Research Study**

**Table 3.2 Cumulative Percent Passing Individual Sieve Sizes for the Ballast Gradations used in the Current Study**

Sieve Size (mm)	Sieve Size (in.)	#4 LB	#4 UB	#24 LB	#24 – 45%	#24 UB
		Cumulative Percent Passing (%)				
76.2	3	N/A	N/A	100	100	100
63.5	2.5	N/A	N/A	95	95	95
50.8	2	100	100	N/A	N/A	N/A
38.1	1.5	95	95	25	45	60
25.4	1	20	55	N/A	N/A	N/A
19	¾	7.5	7.5	5	5	5
12.7	½	N/A	N/A	2.5	2.5	2.5
9.51	3/8	2.5	2.5	N/A	N/A	N/A
4.76	No. 4	N/A	N/A	N/A	N/A	N/A
2.36	No. 8	0	0	0	0	0

Note that ‘LB’ refers to any gradation conforming to the lower bound (coarse-end) of a particular AREMA-specified gradation band. Similarly, ‘UB’ refers to the Upper Bound (fine-end) of a particular specification. In other words, the particle-size distribution curve for a gradation marked as “UB” lies above the corresponding “LB” variant, and therefore is a relatively “finer” gradation. As can be seen from Figure 3.5, the percent passing specifications for a particular sieve size can be significantly different for the lower and upper bounds of the specification. Therefore, it is possible for two ballast materials to have significantly different particle-size distributions, yet meet the same AREMA gradation specification. For example, the percent finer than the 38.1 *mm* (1.5 *in.*) sieve for the AREMA #24 gradation can range from 25% to 60%. Considering that the shear strength of railroad ballast is primarily derived from particle-to-particle interaction, it is quite possible that this large difference in the percent passing a particular sieve will lead to significantly different shear strengths. To study the effect of such variations on ballast shear strength, this study focused on modeling the lower bound (LB) and upper bound (UB) gradations for the AREMA #4 and #24 gradations. Moreover, one additional gradation termed AREMA #24-45%; a representative AREMA #24 gradation with 45% by weight passing the 38.1 *mm* (1.5 *in.*) sieve has been modeled. The aggregate top-sizes for AREMA #4 and AREMA #24 are 50 *mm* (2 *in.*) and 76 *mm* (3 *in.*), respectively.

#### 3.2.1.3 Contact Model Used

Considering that the Discrete Element Method is based on the principle of solving equations of motion from forces and moments generated at contact points between different bodies (balls or facets), the overall response of the model is largely dependent

on the physical properties assigned to different contact points. A linear contact model was assigned to the ball-ball and ball-facet contacts in this simulation effort. The linear model consisting of linear springs and dashpots corresponds with the model developed by Cundall and Strack (1979). In this model, the linear (spring) and dashpot components act parallel to one another. The linear (spring) component ( $F^l$ ) accounts for linear elastic frictional behavior, whereas the dashpot component ( $F^d$ ) models the viscous behavior acting over a vanishingly small area (see Figure 3.6). It should be noted that the linear model does not resist relative rotation; accordingly, the contact moment ( $M_c$ ) equals zero. The linear force is produced by linear springs with constant normal and shear stiffness,  $k_n$  and  $k_s$ , respectively. While, the dashpot force is produced by dashpots with viscosity properties defined in terms of the normal and shear critical-damping ratios,  $\beta_n$  and  $\beta_s$ , respectively.

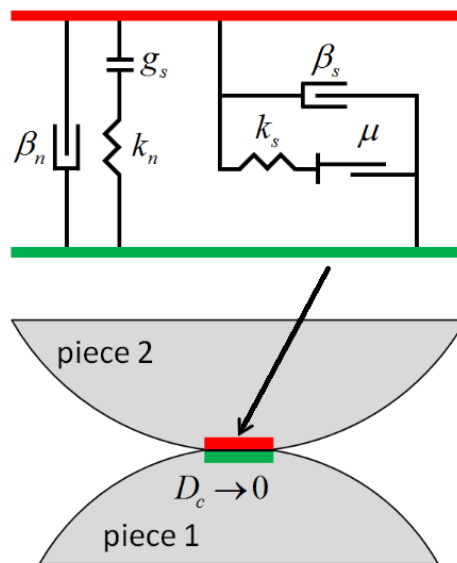


**Figure 3.6 Schematic Representation of the Linear Contact Model Incorporated in PFC (Itasca, 2016)**

The contact is active only when the surface gap ( $g_s$ ) between two surfaces is less than or equal to zero. The linear springs cannot sustain tension, and the slip is accommodated by imposing a Coulomb limit on shear force using the friction coefficient ( $\mu$ ). The force-displacement law for the linear model updates the contact force ( $F_c$ ) and moment ( $M_c$ ) as follows:  $F^c = F^l + F^d$  and  $M_c = 0$ . Details about the mechanics of the linear model can be found elsewhere (Itasca, 2016).

#### 3.2.1.4 Specimen Preparation

The direct shear box simulated in this study is enclosed by 10 rigid boundaries (walls) and is divided horizontally into two equal halves. The top-half of the box consists of 5 walls: one horizontal wall at the top, and four vertical walls at the front, rear, left, and right of the specimen; similarly, the bottom-half of the box consists of 5 walls: one horizontal wall at the bottom, and four vertical walls at the front, rear, left, and right of the specimen. In addition to the ten walls, two more walls (one on the left and one on the right) were added at mid-height of both sides of the box. During the shearing process, the bottom-half of the box was moved to the right at a constant velocity; this was accompanied by the left-wall at mid height moving in the same direction with the same velocity. This is a necessary step to ensure that the particles from the top-box do not escape while the shearing process is in progress.

After creation of the direct shear box, the ballast particles were distributed at random orientations in different bins to simulate the targeted AREMA gradations. The mechanical interaction between the particles was modeled using the linear model; the following parameters were required to define the model properties: particle-size distribution (grain distribution), density, inter-particle friction coefficient, damping

constant and contact stiffness. The model particle density and local damping ratio were chosen as  $2600 \text{ kg}/\text{m}^3$  and 0.7, respectively (typical values found from literature). Note that the damping ratio governs the energy dissipation of the model assembly. The void ratio of the assembly representing the initial condition of the test specimen was controlled at 0.67 (i.e. initial porosity of 0.4). Since, the linear force is produced by linear springs with constant normal and shear stiffness values, these are important model parameters. The ball-ball normal and shear stiffness values were set to  $k_n = 0.5 \times 10^6 \text{ N}/\text{m}$  and  $k_s = 0.5 \times 10^6 \text{ N}/\text{m}$ , respectively. For the ball-facet contact, both the normal and shear stiffness values were set to  $k_n = k_s = 1.0 \times 10^6 \text{ N}/\text{m}$ . Choosing these stiffness values in lower or higher order can significantly affect the stress-strain behavior. Note that it is extremely difficult (and often impractical) to measure the  $k_n$ ,  $k_s$  and damping values for individual particles in the laboratory. Accordingly, it is common practice to iteratively change these values until the simulation results match the stress-strain curves measured in the lab. The direct shear test is performed on both loose and dense samples depending on the desired granular packing. This desired packing can be achieved by adjusting the value of friction coefficient at the ball-ball contacts. Note that iterations were performed during the calibration process by changing these values with an objective to match laboratory-measured stress-strain plots. Making the inter-particle friction coefficient value small results in a denser packing of the granular matrix. The friction coefficient at the ball-ball contact was set to be 0.4, and the ball-facet contact was assumed frictionless.

Distributing the particles inside the shear box can lead to significant overlaps between the particles, thus resulting in high amounts of stored energy at the particle contacts. This stored energy leads to a system that is not in equilibrium. Therefore, by

“cycling” the particle assembly it was ensured that the system attained an equilibrium stage through dissipation of any unbalanced forces in the system. Note that in the current study, the model average ratio was chosen as the criterion of for attending equilibrium conditions. The average ratio is defined as the ratio of the average value of the unbalanced force magnitude (i.e., magnitude of the sum of the contact forces, body forces, and applied forces) over all bodies to the average value of the sum of the magnitudes of the contact forces, body forces and applied forces over all bodies. Once equilibrium was achieved, the cycling of the assembly was stopped. To simplify the calculations, the contact forces were initially set to zero to create an internal stress free state. Moreover, the rotation/spin of each ball was fixed to zero to ensure that the shear stress calculation is only based on the friction. A set of micromechanical parameters adopted for DEM simulation of direct shear tests are given in Table 3.3.

**Table 3.3 Parameters used for DEM Simulations of Direct Shear Strength Tests**

<b>Model Parameters</b>	<b>Values</b>
Specimen Size	Length = 300 mm; Width = 300 mm; Height = 200 mm
Ball-Ball Normal Stiffness	$0.5 \times 10^6 \text{ N/m}$
Ball-Ball Shear Stiffness	$0.5 \times 10^6 \text{ N/m}$
Ball-Ball Inter-Particle Friction Coefficient	0.4
Ball-Facet Normal Stiffness	$1.0 \times 10^6 \text{ N/m}$
Ball-Facet Shear Stiffness	$1.0 \times 10^6 \text{ N/m}$
Ball-Facet Friction Coefficient	0
Density of Particles	$2600 \text{ kg/m}^3$
Normal Stress	103.4, 137.9 and 206.8 kPa (15, 20 and 30 psi)
Shearing Velocity	0.5 cm/sec

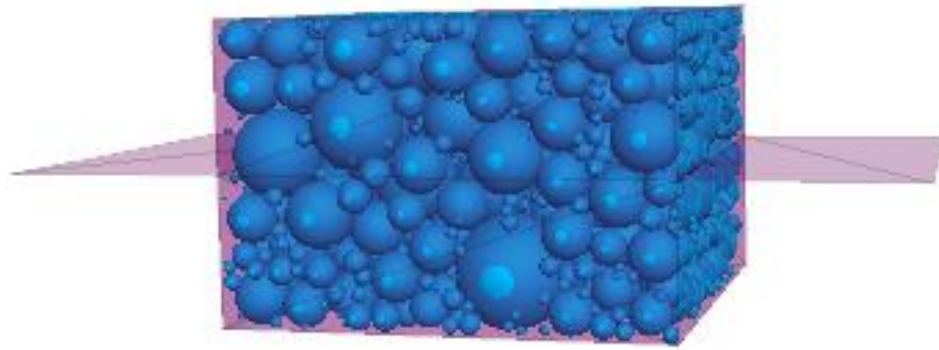
The top plate in the DST model was modeled using a ‘servomechanism’ to apply a specified target normal stress throughout the shearing process. Target normal stresses simulated in this study were 103.4, 137.9 and 206.8 *kPa* (15, 20 and 30 *psi*, respectively). The servomechanism controls the wall position by changing its velocity so that the targeted normal stress can be achieved. Once achieved, the targeted normal stress was kept constant throughout the shearing process.

#### 3.2.1.5 Shearing

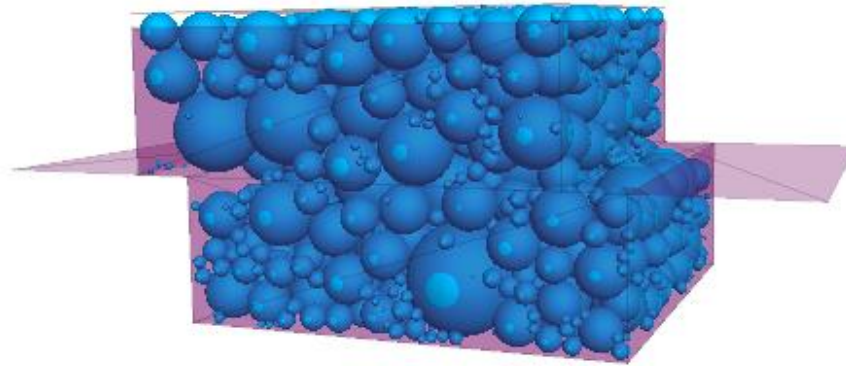
Prior to the shearing process, the two left-walls, the two right-walls, the two back-walls and the two front-walls remain co-planar (Figure 3.7a). During shearing, the bottom half of the box was moved laterally at a constant velocity while keeping the top half fixed. Each specimen was sheared to a horizontal strain of 10% (total horizontal displacement of 30 *mm*; Figure 3.7b). During shearing, the displacement of the top plate was monitored to determine the associated vertical deformation of the specimen. A shearing rate of 0.5 *cm/sec* was used (similar to Liu, 2006 and Tamás et al., 2016). Note that the “primary” specimen was prepared using spherical particles only.

#### 3.2.2 Monitoring

Different subroutines were implemented in the code to monitor the horizontal force on the right wall in the top half of the shear box, and the horizontal displacement of the bottom half of the box. Moreover, the coordination number for a certain zone of the specimen near the failure plane was monitored. Note that coordination number is defined as the average number of contacts that one particle makes with its neighbors (Gu and Yang, 2013).



(a)



(b)

**Figure 3.7 Model Direct Shear Strength Test Specimen Generated: (a) Before Shearing; (b) After Shearing**

### 3.2.3 Visualization of Shear Band

As mentioned earlier, the direct shear test simulation was performed by moving the bottom half of the direct shear box to achieve a horizontal strain of 10%. The shear band can be visualized by tracking the inter-particle contact forces throughout the specimen. As shown in Figure 3.8, the shear band is formed along the shear plane region, which is expected for direct shear tests (as the failure plane is pre-defined).

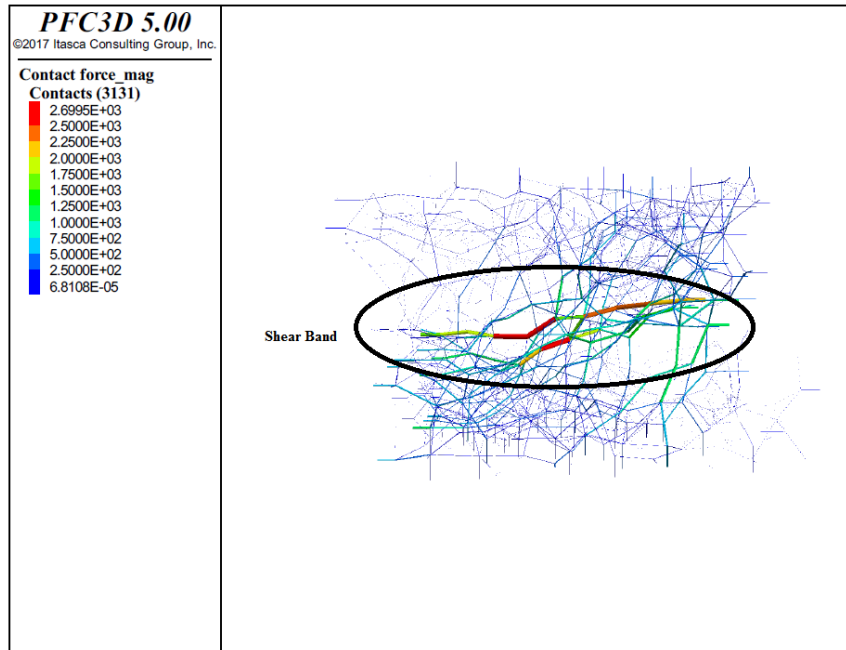


**Figure 3.8 Visualization of the Shear Band in Direct Shear Strength Testing Simulation**

### 3.3 Model Calibration Using Laboratory-Test Data

Once DEM simulation of the “primary” specimen for Direct Shear Testing of ballast was complete, the next task involved calibrating the model using laboratory-test data. The simulated model was validated using laboratory data reported by Huang et al. (2009, 2010, and 2011). A brief background on the laboratory testing effort reported by Huang et al. (2009, 2010, and 2011) is given below.

The ballast material tested was a clean granite aggregate with a specific gravity of 2.62. The granite aggregate size distribution conformed to AREMA #24 specification with  $D_{\max} = 63.5 \text{ mm}$ ,  $D_{\min} = 25.4 \text{ mm}$ , and  $D_{50} = 45 \text{ mm}$ . The test device was a square box with side dimensions of  $305 \text{ mm}$  (12 in.) and a specimen height of  $203 \text{ mm}$  (8 in.). The initial porosity value was calculated to be 0.43. The ballast samples were sheared horizontally in the shear box under normal stress values of 172, 241 and  $310 \text{ kPa}$

(25, 35 and 45 *psi* respectively). Figure 3.9 shows the laboratory direct shear strength testing setup used by Huang et al. (2009).



**Figure 3.9** Photograph of Direct Shear Test Equipment at the University of Illinois at Urbana-Champaign (Huang et al., 2009)

While calibrating the model, the same ballast gradation, direct shear box size, initial porosity as the laboratory were used. Ballast particles were simulated using both spherical balls and 2-ball clumps. Other model parameters were adjusted match the DEM-simulated stress-strain curves with those generated during the laboratory testing effort.

### 3.3.1 Model Calibration - Using Spheres

The ball-ball normal and shear stiffness values were set to  $k_n = 1.5 \times 10^6 \text{ N/m}$  and  $k_s = 1.5 \times 10^6 \text{ N/m}$ , respectively. Similarly, both of the ball-facet normal and shear

stiffness values were set to  $k_n = k_s = 3.0 \times 10^6 \text{ N/m}$ . Note that these stiffness values will be retained for further simulations during the parametric analyses. The friction coefficient at the ball-ball contact was set to be 0.3, while keeping the ball-facet friction coefficient values to be 0. Since 310 kPa (45 psi) is a considerably large value of applied normal stress that may not be representative of actual field conditions, it was omitted from the calibration efforts. Figure 3.10 shows the results of model calibration using the laboratory-test data, where a close match between the laboratory-test and DEM simulation results was found. All the model parameters used while calibrating the model are tabulated in Table 3.4.

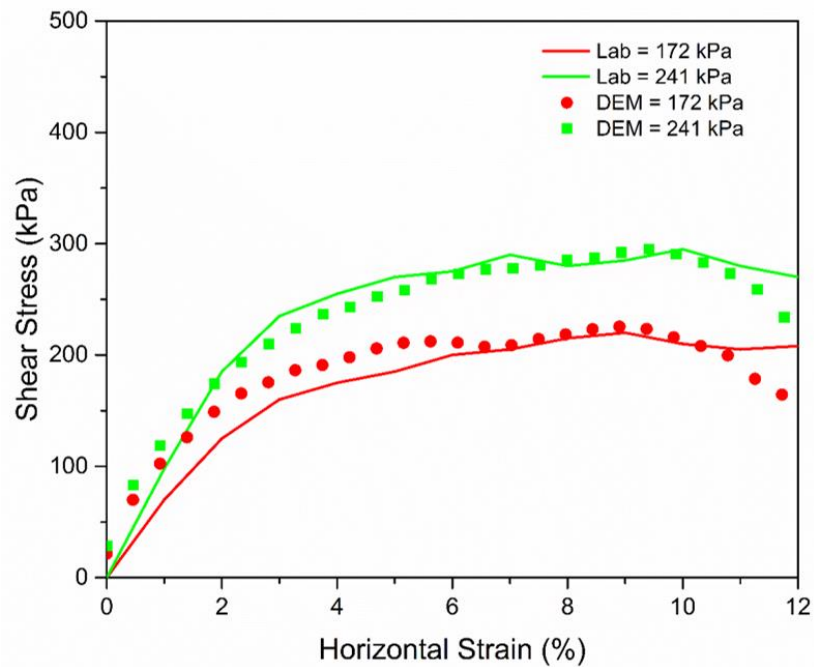


**Figure 3.10 Model Calibration using Laboratory-Test Data (Ballast Particles Simulated as Spherical Balls)**

**Table 3.4 Parameters used in Calibrating the DEM Model of Direct Shear Tests (Ballasts Simulated as Spherical Balls)**

<b>Model Parameters</b>	<b>Parameter Values Established after Model Calibration</b>
Contact Model	Linear
Ball-Ball Normal Stiffness	$1.5 \times 10^6 \text{ N/m}$
Ball-Ball Shear Stiffness	$1.5 \times 10^6 \text{ N/m}$
Ball-Ball Inter-Particle Friction Coefficient	0.3
Ball-Facet Normal Stiffness	$3.0 \times 10^6 \text{ N/m}$
Ball-Facet Shear Stiffness	$3.0 \times 10^6 \text{ N/m}$
Ball-Facet Friction Coefficient	0
Coefficient of Local Damping	0.7
Shearing Velocity	$0.5 \text{ cm/sec}$

### 3.3.2 Model Calibration - Using 2-ball Clumps

The pebble-pebble normal and shear stiffness values were set to  $k_n = 1.5 \times 10^6 \text{ N/m}$  and  $k_s = 1.5 \times 10^6 \text{ N/m}$ , respectively. Similarly, both the pebble-facet normal and shear stiffness values were set to  $k_n = k_s = 3.0 \times 10^6 \text{ N/m}$ . The friction coefficient at the pebble-pebble contact was set to be 0.2, while keeping the pebble-facet friction coefficient values to be 0. As with the case with spherical particles, the normal stress level of  $310 \text{ kPa}$  ( $45 \text{ psi}$ ) was omitted from the calibration efforts. Figure 3.11 shows the results of model calibration using the laboratory-test data, where a close match between the laboratory-test and DEM simulation results was found. Hence, it is proved that the simulated direct shear strength testing model can be validated with any number of balls. However, it should be noted that other model parameters needs to be changed accordingly. Note that the primary difference between the model comprising spherical

particles (Figure 3.10) and the model comprising 2-ball clumps (Figure 3.11) was in the assigned friction coefficient at the pebble-pebble contact (0.3 for the model with spheres; 0.2 for the model with 2-ball clumps).

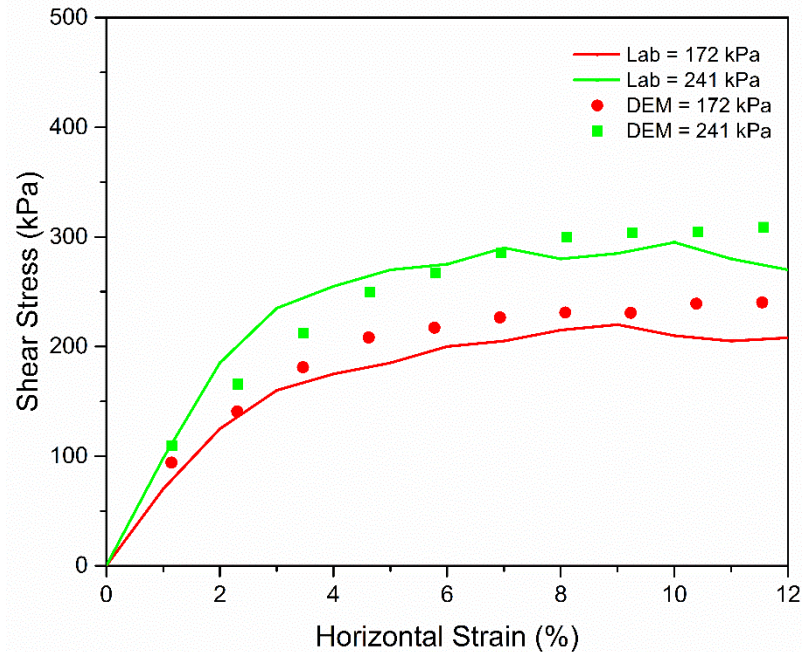


**Figure 3.11 Model Calibration using Laboratory-Test Data (Ballast Particles Simulated as 2-ball Clumps)**

### 3.4 Parametric Study on Direct Shear Test (DST) Results

A series of simulations were performed to establish the effects of different material (i.e. particle-size distribution), specimen, and test parameters on ballast shear strength behavior. Different parameters studied were: ballast specific gravity and initial porosity, inter-particle friction coefficient, and applied normal stress levels. The “control specimen” having AREMA #24 - 45% ballast gradation and a specific gravity of 2.60 was simulated using spherical shaped ballast particles. The specimen size was set to  $300\text{ mm} \times 300\text{ mm} \times 200\text{ mm}$ , initial porosity was set to 0.4, and the target normal stresses were: 103.4, 137.9 and 206.8  $kPa$  (15, 20 and 30  $psi$ , respectively). Note that during the

parametric analysis, all model parameters were kept constant, except for the parameter of interest being studied. As shown in Figure 3.12, the shear strength parameters ( $c$  and  $\phi$ ) were calculated using the Coulomb's equation (Equation 2.6). Note that the cohesion intercept was set to zero ( $c = 0$ ) for the cohesion-less ballast material.

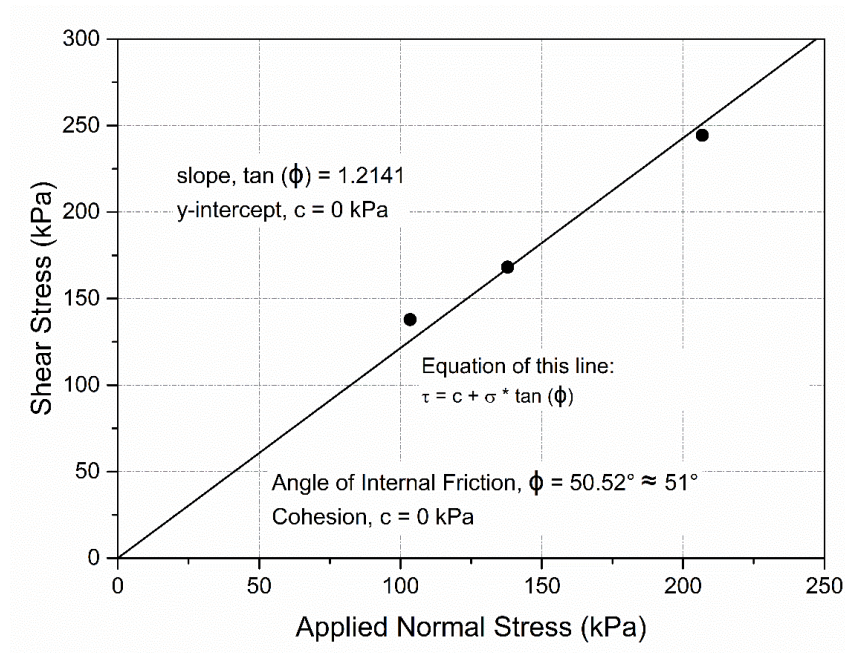
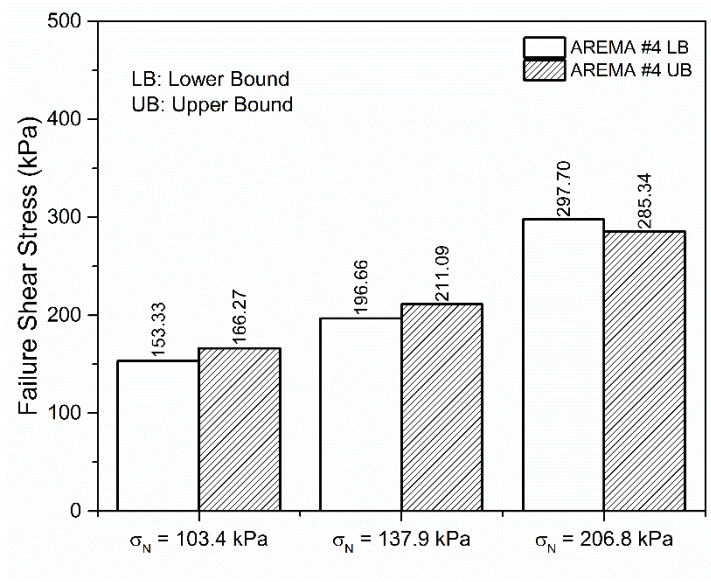


**Figure 3.12** Calculating the Shear Strength Parameters (Results Presented for the Control Specimen Comprising Spherical Particles)

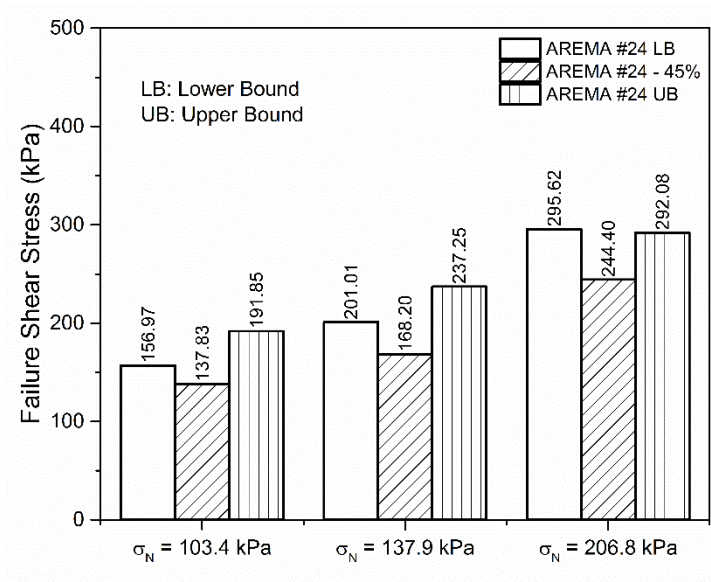
#### 3.4.1 Effect of Ballast Gradations

The effect of particle-size distribution (or gradation) was studied using five different ballast gradations satisfying AREMA gradation specifications for mainline tracks. When simulated, the number of particles for AREMA #4 LB, #4 UB, #24 LB, #24 - 45%, and #24 UB specimens was 2839, 3261, 1205, 1355, and 1445 respectively. For both AREMA #4 and #24 gradations, moving from lower bound (coarse-end) to upper bound (fine-end) of the gradation band, the number of particles increases, with the top

size remaining the same. Figure 3.13 shows the comparative evaluation of the effects of gradation on the failure shear stress.



(a)



(b)

**Figure 3.13 Comparative Evaluation of Failure Shear Stress for (a) AREMA #4 and (b) AREMA #24 Ballast Gradations**

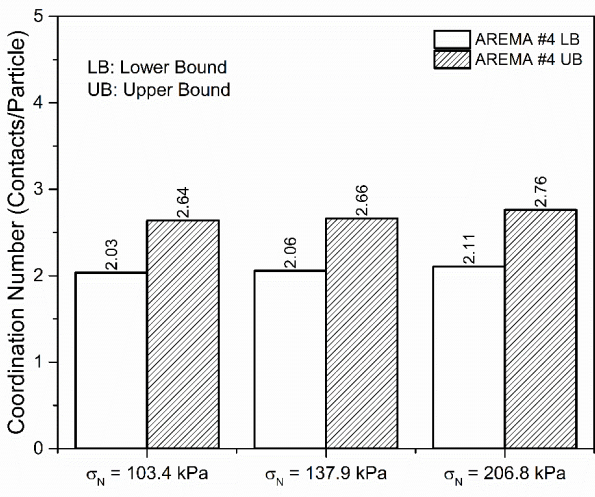
As seen from Figure 3.13, both for AREMA #4 and #24 materials, the UB results in higher failure shear stresses compared to the LB for normal stress levels of 103.4 *kPa* and 137.9 *kPa*. However, the trend is reversed at the highest normal stress level (206.8 *kPa*). It is important to note that normal stress levels of 206.8 *kPa* (30 *psi*) may be unrealistic for field conditions. Therefore, trends for the lower to normal stress levels may be more representative of track behavior under train loading. The increase in failure shear stress as we move from the LB to UB can be attributed to the higher number of particles, which leads to increased resistance against shearing. For the AREMA #24 gradation, it can be observed that the failure shear stress decreases from LB to 45%, and then increases from 45% to UB (see Figure 3.13b). No logical explanation to this trend could be found during this study. From Table 3.5, the angle of internal friction was found to be 55° for AREMA #4 material, and ranged between 51° and 57° for the AREMA #24 material.

**Table 3.5 Angle of Internal Friction Values for Different Ballast Gradations Established through DEM Simulation of Direct Shear Tests**

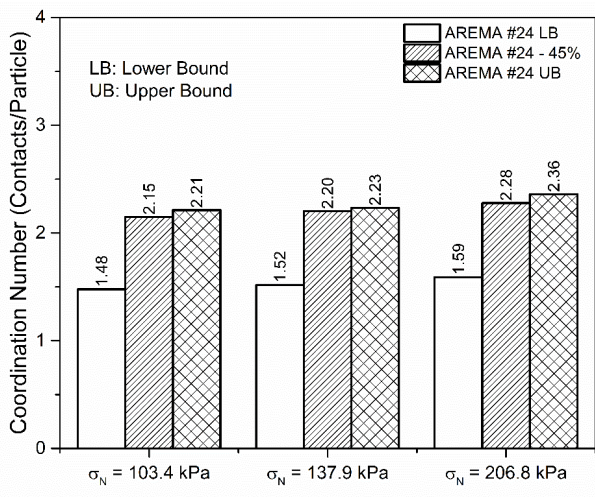
	For AREMA #4		For AREMA #24		
	#4 LB	#4 UB	#24 LB	#24 - 45%	#24 UB
$\phi$	55°	55°	55°	51°	57°

The coordination number (average number of contacts per particle) was monitored throughout the direct shear test simulation, and the results are shown in Figure 3.14. For models with #4 LB, #4 UB, #24 LB, #24 - 45%, and #24 UB gradations, the average coordination number values were 2.07, 2.69, 1.53, 2.22, and 2.27, respectively. Note that the average coordination number values listed here were calculated by averaging the coordination numbers under all three applied normal stress levels. From the

result trends as shown in Figure 3.14a and Figure 3.14b, it can be inferred that, for any particular gradation, as the number of particles increases, the average coordination number increases. For both AREMA #4 and #24 ballast gradations, from lower bound to upper bound, there is an increasing trend of average coordination number. As the normal stress increases, the coordination number increases; similar trends were reported by Gu and Yang (2013).



(a)



(b)

**Figure 3.14 Comparative Evaluation of Coordination Number for (a) AREMA #4 and (b) AREMA #24 Gradations**

### 3.4.2 Effect of Flat & Elongated Ratio

In this study, four different Flat and Elongated (F&E) ratio values were chosen (1.0, 2.3, 3.0 and 3.5), and ballast particles were created with the help of the “clump logic” to match these target F&E ratios. Note that the specimen designated with an F&E ratio value of 1.0 comprises spherical particles. Column plots showing the change in failure shear stress value with F&E ratio value at different normal stress levels are presented in Figure 3.15. As shown in the figure, a significant increase in the failure shear stress values was observed with increasing F&E ratio values. As the F&E ratio value changed from 1.0 to 3.5, the friction angle ( $\phi$ ) value changed from  $51^\circ$  to  $81^\circ$  (see Table 3.6).

It is important to note that although increasing F&E ratio values appear to be beneficial in terms of increasing the shear strength of the ballast material, they are not recommended for use in the field. This is primarily because flat and elongated particles are more susceptible to breaking under loading. Once the particles break under loading, the overall particle-size distribution of the ballast can change significantly. Excessive breakage of particles can lead to highly fouled ballast gradations, which in turn can deteriorate the shear strength significantly. The simulated direct shear tests comprising flat and elongated particles resulted in significantly high failure stress values because the models developed under the current study did not accommodate breakage of individual ballast particles.

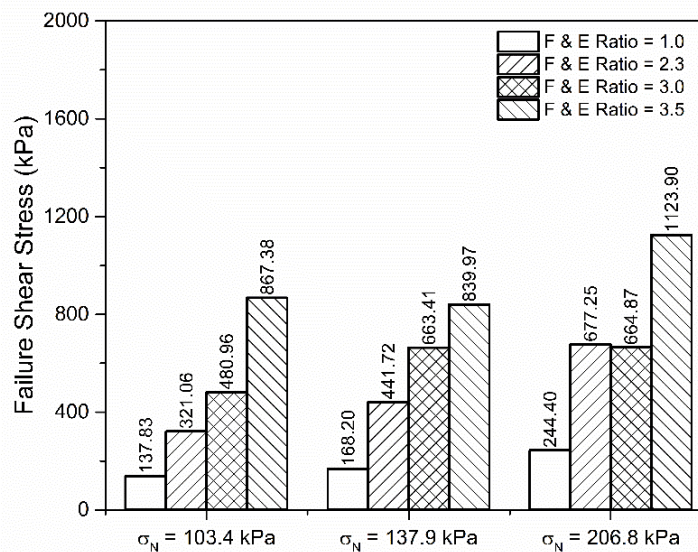


**Figure 3.15 Comparative Evaluation of Failure Shear Stress for Specimens Comprising Particles with Different F & E Ratio**

**Table 3.6 Comparative Evaluation of Angle of Internal Friction Showing the Effect of F & E Ratio**

	F & E Ratio			
	1.0	2.3	3.0	3.5
$\phi$	51°	73°	75°	81°

### 3.4.3 Effect of Particle Angularity

As already mentioned, this research study utilized the method proposed by Lees (1964) to visually quantify the angularity of different ballast particles. Four different degrees of angularity ranges were selected ( $A = 0$  to 99;  $A = 300$  to 399;  $A = 600$  to 699 and  $A = 900$  to 999), and ballast particles were created to visually match these angularity values. Direct shear specimens were then prepared with particles corresponding to the target angularity values. The specimen comprising spherical particles corresponded to an angularity range of 0 to 99. Figure 3.16 shows the change in failure shear stress values mobilized during the simulated DSTs. Increasing angularity values lead to increasing

failure shear stress values. The simulation results show that internal friction angles as high as  $66^\circ$  can be achieved for highly angular ballast particles (see Table 3.7).

Similar conclusions can be drawn by comparing the increase in failure shear stresses achieved by using clumps comprising different number of ‘balls’ (see Figure 3.17). As shown in the figure, as the number of balls in the clump increases, the failure shear stress values increase.

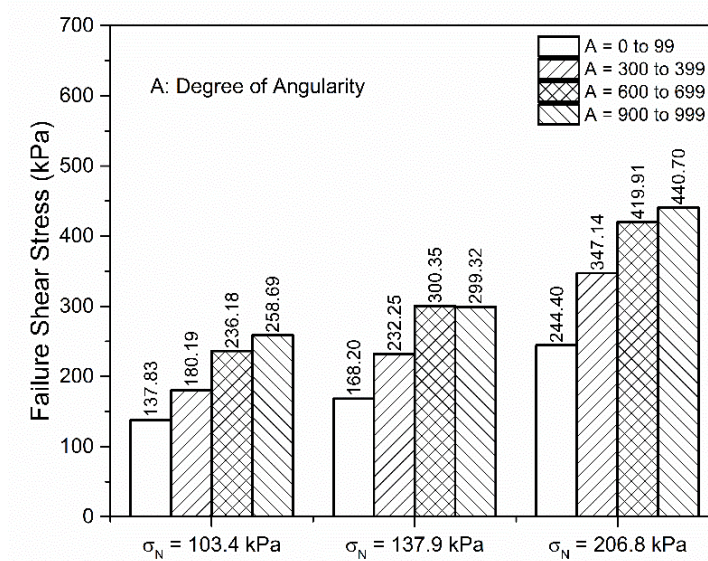


**Figure 3.16 Comparative Evaluation of Failure Shear Stress for Different Degree of Angularity of Ballasts**

**Table 3.7 Comparative Evaluation of Angle of Internal Friction Showing the Effect of Degree of Angularity**

	Degree of Angularity ('A' Value) Range			
	0 to 99	300 to 399	600 to 699	900 to 999
$\phi$	$51^\circ$	$60^\circ$	$65^\circ$	$66^\circ$

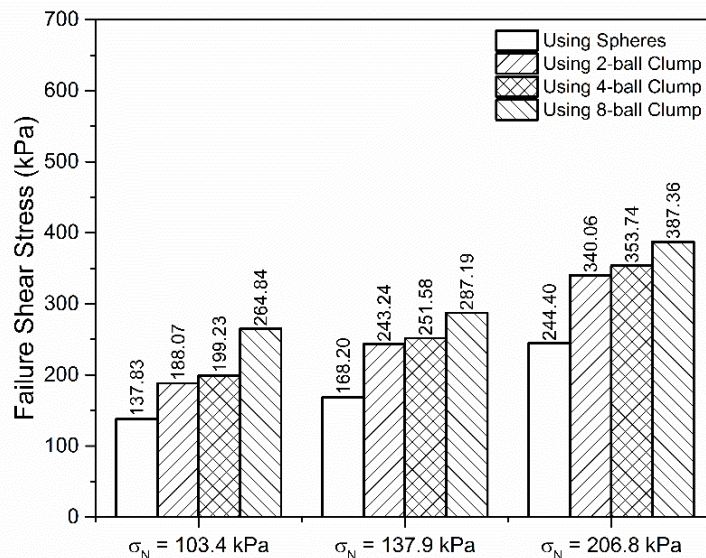


**Figure 3.17 Comparative Evaluation of Failure Shear Stress for Different Particle Shapes**

The effect of number of balls in the clump on ballast shear strength was also reflected by an increase in the friction angle ( $\phi$ ) values. It should be noted that the most significant jump in the friction angle values is observed as one moves from spherical particles to 2-Ball clumps (an increase from  $51^\circ$  to  $60^\circ$ ) (see Table 3.8). As the number of balls in the clumps is subsequently increased to 4 and 8, the increase in the friction angle value is less drastic. This indicates that for unbound aggregate materials such as railroad ballast, the most significant improvement in shear strength is achieved as one moves from rounded particles to angular particles. Subsequent increase in the degree of angularity does not result in significant shear strength increase.

**Table 3.8 Comparative Evaluation of Angle of Internal Friction Showing the Effect of Particle Shapes**

	Particle Shapes			
	Spheres	2-ball Clumps	4-ball Clumps	6-ball Clumps
$\phi$	$51^\circ$	$60^\circ$	$61^\circ$	$64^\circ$

### 3.4.4 Effect of Aggregate Top-Size

Three different ballast gradations having aggregate top-size of 38, 50 and 76 mm were tested, and the simulation results have been presented in Figure 3.18 and Table 3.9. The simulation results indicated that, with an increase of aggregate top-size, both failure shear stress and angle of internal friction increases. For the lowest (38 mm) and highest (76 mm) top sizes the angle of internal friction values were found to be 53° and 57°, respectively. From these results, it can be inferred that the higher the aggregate top-size, the higher will be the shear strength.

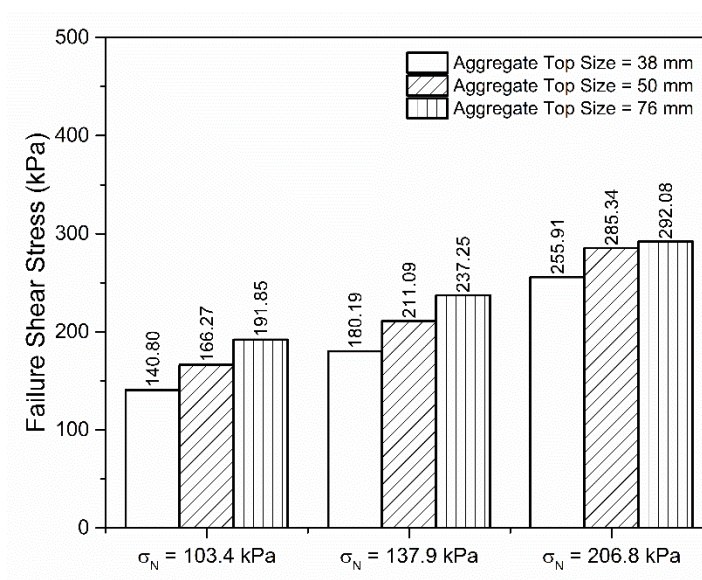


**Figure 3.18 Comparative Evaluation of Failure Shear Stress for Different Aggregate Top Sizes**

**Table 3.9 Comparative Evaluation of Angle of Internal Friction Values for Different Aggregate Top Sizes**

	Aggregate Top Size		
	38 mm	50 mm	76 mm
$\phi$	53°	55°	57°

### 3.4.5 Effect of Material Specific Gravity

The material specific gravity was varied from 2.6 to 2.7, and its effect on the railroad ballast shear strength was studied. Note that all the other parameters of the control specimen were kept constant. As shown in Figure 3.19 and Table 3.10, an increasing trend in failure shear stress and angle of internal friction was observed with increasing material specific gravity.

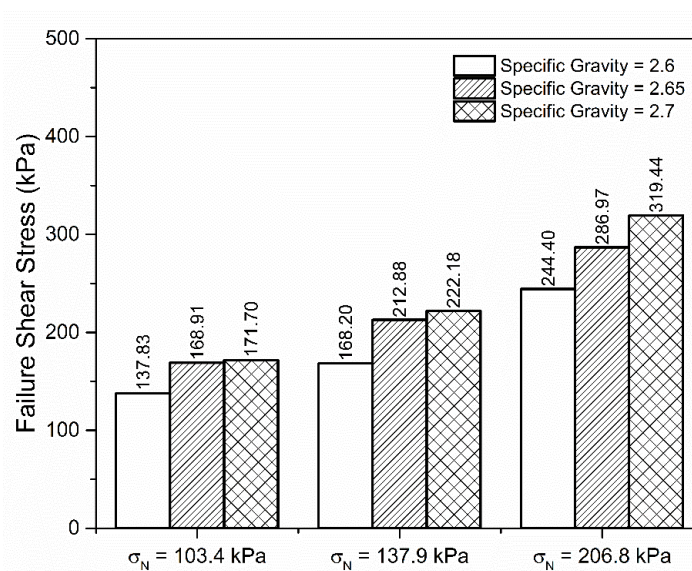


**Figure 3.19 Comparative Evaluation of Failure Shear Stress Showing the Effect of Material Specific Gravity**

**Table 3.10 Comparative Evaluation of Angle of Internal Friction for Different Material Specific Gravity**

	Material Specific Gravity		
	2.6	2.65	2.7
$\phi$	51°	56°	58°

### 3.4.6 Effect of Specimen Porosity

Specimen porosity is defined as the fraction of the total volume that is taken up by pore space. The effect of specimen porosity on the railroad ballast shear strength was

studied by varying the specimen porosity from 0.30 to 0.40 (corresponds to void ratio range between 0.43 and 0.67) while keeping the other parameters of the control specimen constant. Simulation results are presented in Figure 3.20 and Table 3.11.

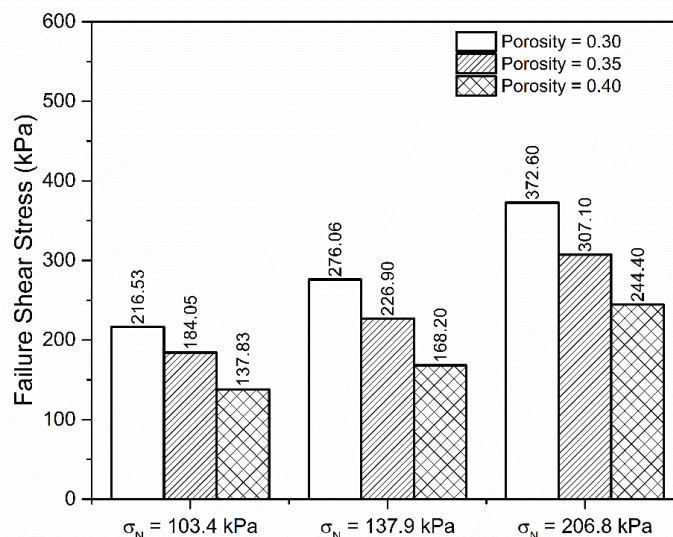


**Figure 3.20** Comparative Evaluation of Failure Shear Stress Showing the Effect of Specimen Porosity

**Table 3.11** Comparative Evaluation of Angle of Internal Friction for Different Specimen Porosity

	Specimen Porosity		
	0.30	0.35	0.40
$\phi$	62°	58°	51°

As seen from Figure 3.20 and Table 3.11, as the specimen porosity increases, both the failure shear stress and the angle of internal friction values decrease. This is because small porosity values correspond to tightly packed granular matrices that comprise better particle-particle interlock. Although, a ballast layer with higher porosity corresponds to higher permeability values, packing condition in such a granular matrix often leads to significantly lower shear strength values. However, it should be kept in mind that the

construction of a ballast layer with low porosity values may require significant compaction efforts, which may not be feasible in practice.

### 3.4.7 Effect of Coefficient of Inter-Particle Friction

The direct shear test can be performed on loose or dense specimens depending on the desired granular packing. In DEM simulation, the desired packing stage of a sample can be achieved by adjusting the friction coefficient value at the ball-ball contacts. In this study, the ball-ball coefficient of friction was varied from 0.2 to 0.5 while keeping the rest of the values same as the control specimen parameters. Note that making the inter particle friction coefficient value too small results in denser packing, because smoother particles let each other slip past each other. From the test results, (see Figure 3.21) it can be observed that as the ball-ball friction coefficient increases, the failure shear stress value also increases. Besides, for any ball-ball friction coefficient value, the failure shear stress value increases with increasing applied normal pressure.

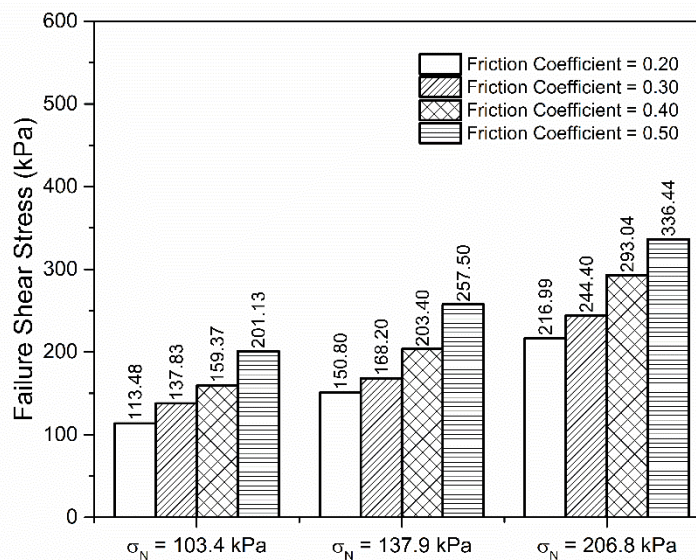


**Figure 3.21 Comparative Evaluation of Failure Shear Stress Showing the Effect of Inter-particle Friction Coefficient**

Table 3.12 compares the angle of internal friction ( $\phi$ ) values determined for specimens comprising ballast particles with different friction coefficient values. The  $\phi$  value was found to be within the range of  $47^\circ$  to  $60^\circ$ , and increased with increasing friction coefficient values. During the packing stage, a low coefficient of friction value helps in denser-packing; however, after completion of the packing stage, higher friction coefficient values results in higher shear strength values.

**Table 3.12 Comparative Evaluation of Angle of Internal Friction Showing the Effect of Coefficient of Inter-particle Friction**

	Coefficient of Inter-Particle Friction			
	0.20	0.30	0.40	0.50
$\phi$	$47^\circ$	$51^\circ$	$55^\circ$	$60^\circ$

#### 3.4.8 Effect of Applied Normal Stress Level

The effect of applied normal stress on ballast shear strength behavior was studied by varying the normal stress value during direct shear testing between  $34.5 \text{ kPa}$  ( $5 \text{ psi}$ ) and  $206.8 \text{ kPa}$  ( $30 \text{ psi}$ ). As shown in Figure 3.22, the failure shear stress increases with increase in the normal stress value. This establishes that the DEM model is capable of capturing the right trends in the unbound granular material behavior. It should be noted that similar trends were reported by Indraratna et al. (2012), Ngo et al. (2014 and 2015), and Wang et al. (2015). During the current simulation effort, it was observed that increasing the normal stress from  $34.5$  to  $206.8 \text{ kPa}$ , resulted in an increase in the failure shear stress value by 305%.

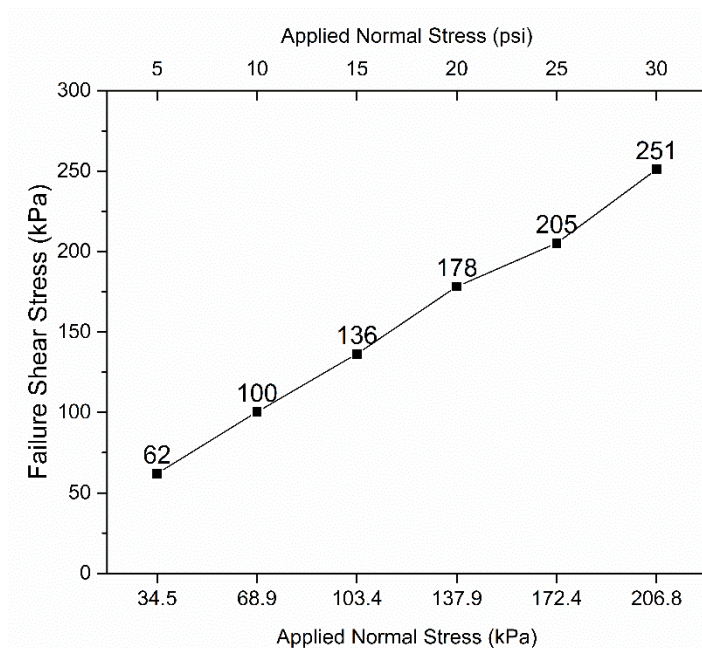


**Figure 3.22 Comparative Evaluation of Failure Shear Stress Showing the Effect of Applied Normal Stress Level**

Upon completion of the parametric analysis of direct shear strength test results, the next task involved in-depth analysis of packing conditions within the ballast matrix to identify particle size proportions that would maximize the shear strength. Details of this task have been presented in the following section.

### **3.5 Study of Ballast Packing Conditions Using the Concept of Coarse to Fine Ratio**

The range of aggregate particle sizes commonly observed in pavement base/subbase layers is significantly different from those observed in railroad ballast. As evident from Figure 2.3 and Table 2.1, railroad ballast typically comprises particles ranging in size from  $9.5 \text{ mm}$  ( $\frac{3}{8} \text{ in.}$ ) to  $76 \text{ mm}$  ( $3 \text{ in.}$ ). Typical unbound aggregate base and subbase materials used in pavement applications on the other hand, comprise particles as large as  $25.4 \text{ mm}$  ( $1 \text{ in.}$ ) to a certain fraction finer than  $0.075 \text{ mm}$

(#200 sieve). Accordingly, the definition of ‘coarse’ and ‘fine’ particles can be different for railroad ballast and pavement base/subbase materials. As discussed in Chapter 2, Xiao et al. (2012) used the concept of Gravel to Sand Ratio (G/S Ratio) to quantify the packing characteristics for dense-graded pavement base materials. The primary underlying principle for such an analysis approach is that ‘gravel’ particles create voids in the granular matrix, and ‘sand’ particles fill those voids. Therefore, based on the relative proportion of ‘gravel’ and ‘sand’ particles, the aggregate matrix can attain maximum shear strength. Extending this analysis approach to railroad ballast can shed some light on the importance of different size fractions in a ballast matrix. However, considering that particle size ranges in a ballast matrix are significantly different from those in a dense-graded aggregate base material, the concept of G/S ratio proposed by Xiao et al. (2012) cannot be directly applied to study the packing conditions in ballast. Two different alternatives to define a gradation parameter similar in concept to the G/S Ratio were explored in the current research effort, and have been discussed in the following section.

### 3.5.1 Development of a Coarse to Fine Ratio Gradation Parameter for Railroad Ballast - Alternative – 1

As already described, the definition of ‘coarse’ and ‘fine’ particles in an aggregate matrix should be based on the relative size of individual grains in the matrix, rather than being based on certain fixed sieve sizes. For example, the Unified Soil Classification System (USCS) uses the 4.75 mm sieve opening size (#4 sieve) as the boundary between coarse and fine particles. Particles larger than 4.75 mm are classified as ‘coarse’, whereas particles smaller than 4.75 mm are classified as ‘fine’. However, applying these definitions to railroad ballast can be erroneous, as most particles in a ballast material are

larger than  $4.75\text{ mm}$ , therefore indicating the absence of any ‘fine’ particles. However, depending on relative distribution of particle sizes within the ballast matrix, certain particles serve to create voids (coarse fraction), and certain particles serve to fill the voids (fine fraction). Accordingly, rather than using the standard definitions of ‘gravel’ and ‘sand’, analysis of packing conditions in a ballast matrix may be better served by using relative definitions of ‘coarse’ and ‘fine’ particles.

To define the ‘coarse’ and ‘fine’ particles in a ballast mix, an approach similar to the one described by the Bailey Method can be used. As already discussed in Chapter 2, the Bailey method defines coarse particles as those larger than the Primary Control Sieve (PCS); similarly, particles smaller than the PCS can be categorized as ‘fine’. Figure 3.23 shows a visual representation of relative particle sizes in an aggregate mix. Based on the relative definitions of ‘coarse’ and ‘fine’ particles as illustrated in Figure 3.23, a new gradation parameter known as the coarse-to-fine ratio can be defined as in Equation 3.1:

$$\frac{C}{F} = \frac{p_{NMPS} - p_{PCS}}{p_{PCS} - p_{TCS}} \quad \text{(Equation 3.1)}$$

where  $p_{NMPS}$  = percentage of material by weight passing the NMPS sieve size,

$p_{PCS}$  = percentage of material by weight passing the PCS,  $p_{TCS}$  = percentage of material by weight passing the TCS.

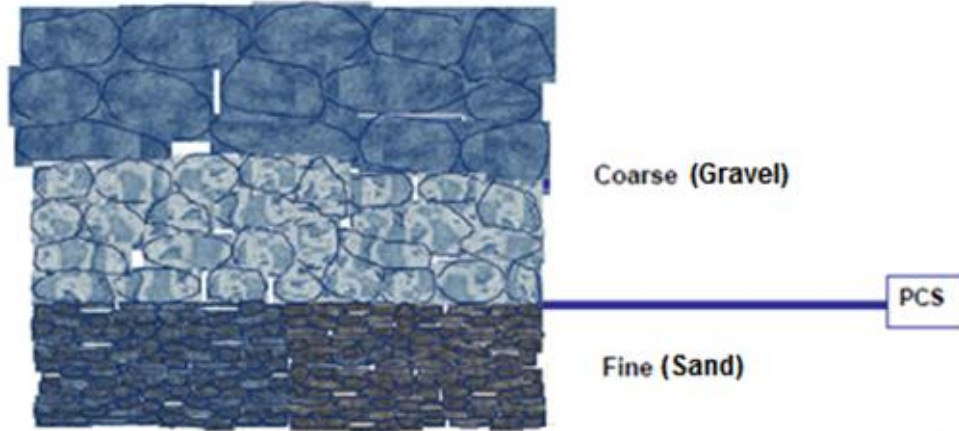


**Figure 3.23 Schematic of Particles in a Box (figure not drawn to scale) (adopted from Vavrik et al., 2002)**

Three different gradation blends were chosen satisfying the AREMA#24 gradation specification (Table 3.13). The NMPS, PCS, and TCS sieve sizes for AREMA #24 were 63.5, 19, and 2.36 mm, respectively. According to the definition presented in Equation 3.1, the selected gradations corresponded to C/F ratio values of 8, 17, and 35, respectively. Since the three gradations did not contain any material finer than 2.36 mm,  $p_{TCS}$  value was zero, meaning the  $p_{TCS}$  would have no effect in the definition of ‘fine’ particles for any AREMA #24 gradation.

**Table 3.13 Examples of the Coarse-to-Fine Ratio Concept for Railroad Ballasts – For AREMA #24 Gradations**

Sieve Size ( <i>mm</i> )	Sieve Size ( <i>in.</i> )	AREMA #24 - Variant 1	AREMA #24 – Variant 2	AREMA #24 – Variant 3
		Cumulative Percent Passing (%)		
76.20	3	100.0	100.0	100.0
63.50	2.5	90.0	90.0	90.0
38.10	1.5	45.0	45.0	45.0
19.00	3/4	10.0	5.0	2.5
12.70	1/2	2.5	2.5	0.0
2.38	0.0937 (No. 8)	0.0	0.0	0.0
<b>C/F Ratio</b>		<b>8.0</b>	<b>17.0</b>	<b>35.0</b>

Similarly, three different gradation blends were chosen satisfying the AREMA#4 gradation specification (Table 3.14). The NMPS, PCS, and TCS sieve sizes for the AREMA #4 gradations were 38.1, 9.5, and 0.6 *mm*, respectively. Per Equation 3.1, the C/F ratio values were 8.5, 23, and 37, respectively. Similar to the AREMA #24 gradation,  $p_{TCS}$  would have no effect in the definition of fine particles for any AREMA #4 gradation; an improved definition of the ‘fine’ fraction in the ballast mix was therefore desired.

**Table 3.14 Examples of the Gravel-to-Sand Ratio Concept for Railroad Ballasts – For AREMA #4 Gradations**

Sieve Size (mm)	Sieve Size (in.)	AREMA # 4 - Variant 1	AREMA # 4 - Variant 2	AREMA # 4 - Variant 3
		Cumulative Percent Passing (%)		
50.80	2	100.0	100.0	100.0
38.10	1.5	95.0	90.0	95.0
25.40	1	37.5	37.5	35.0
19.00	3/4	12.5	12.5	7.5
9.50	3/8	10.0	3.75	2.5
2.38	0.0937 (No. 8)	0.0	0.0	0.0
<b>C/F Ratio</b>		<b>8.5</b>	<b>23.0</b>	<b>37.0</b>

### 3.5.2 Development of a Coarse to Fine Ratio Gradation Parameter for Railroad Ballast - Alternative – 2

As discussed in the previous sub-section, the  $p_{TCS}$  term used in the definition of C/F ratio per Equation 3.1 did not have any impact on the calculated value for the gradation parameter. Accordingly, a modified approach was developed where particles larger than the median sieve size is classified as ‘coarse’, whereas particles smaller than median sieve are classified as ‘fine’. The modified C/F Ratio definition can therefore be presented as in Equation 3.2:

$$\frac{C}{F} = \frac{p_{NS} - p_{MS}}{p_{MS} - p_{SS}} \quad \text{(Equation 3.2)}$$

where  $p_{NS}$  = percentage of material by weight passing the nominal maximum sieve size,  $p_{MS}$  = percentage of material by weight passing the median sieve size,  $p_{SS}$  = percentage of material by weight passing the smallest sieve size. As before, the nominal

sieve size is defined as one sieve larger than the first sieve that retains more than 10%, smallest sieve is defined as one sieve larger than the first sieve that retains 100% of the material, and median sieve is the median sieve size between lowest and highest sieve in any gradation.

The primary advantage of this approach over the one presented in Alternative # 1 is that the definitions of coarse and fine are based on the relative distribution of particles in the mix, and not on a fixed set of sieve sizes. Two different gradation blends were chosen satisfying the AREMA#24 gradation band (Table 3.15). The NS, MS, and SS sieve sizes were 63.5 mm, 38.1 mm, and 12.7 mm, respectively. Per Equation 3.2, the C/F ratio values were calculated to be 0.83, and 1.28, respectively.

**Table 3.15 Examples of the Coarse-to-Fine Ratio (C/F Ratio) Concept for Railroad Ballasts – For AREMA #24 Gradations**

Sieve Size (mm)	Sieve Size (in. )	AREMA # 24 – Variant 1	AREMA # 24 – Variant 2
		Cumulative Percent Passing (%)	
76.20	3	100.0	100.0
63.50	2.5	97.5	97.5
38.10	1.5	55.0	45.0
19.00	3/4	8.0	8.0
12.70	1/2	4.0	4.0
2.38	0.0937 (No. 8)	0.0	0.0
<b>C/F Ratio</b>		<b>0.83</b>	<b>1.28</b>

Similarly, two different gradation blends were chosen satisfying the AREMA # 4 specifications (see Table 3.16). The NS, MS, and SS sieve sizes were 38.1 mm, 25.4 mm, and 9.5 mm, respectively. Calculated values of the C/F ratio were 1.88, and 2.93, respectively.

**Table 3.16 Examples of the Coarse-to-Fine Ratio (C/F Ratio) Concept for Railroad Ballasts – For AREMA #4 Gradations**

Sieve Size (mm)	Sieve Size (in.)	AREMA # 4 – Variant 1	AREMA # 4 – Variant 2
		Cumulative Percent Passing (%)	
50.80	2	100.0	100.0
38.10	1.5	95.0	92.5
25.40	1	35.0	25.0
19.00	3/4	7.5	5.0
9.50	3/8	3.0	2.0
2.38	0.0937 (No. 8)	0.0	0.0
<b>C/F Ratio</b>		<b>1.88</b>	<b>2.93</b>

### 3.5.3 Effect of C/F Ratio on Ballast Shear Strength

Once a modified definition of the C/F Ratio was finalized, the next task involved simulating direct shear strength tests on ballast materials corresponding to different C/F Ratio values; direct shear tests on specimens satisfying both AREMA #24 and AREMA #4 gradation specifications were simulated during this task. For AREMA #24 gradation, four different particle-size distributions with C/F Ratio values of 0.83, 1.28, 1.51, and 2.23, respectively were chosen (see Figure 3.24). Results from direct shear test simulations on these four gradations are summarized in Figure 3.25. As seen from Figure 3.25, specimens corresponding to C/F = 1.51 yielded the highest failure stress values. Table 3.17 lists the friction angle ( $\phi$ ) values for the four different gradations. As with the failure shear stress value, the specimen corresponding to C/F = 1.51 yielded the highest friction angle value ( $\phi = 62^\circ$ ).

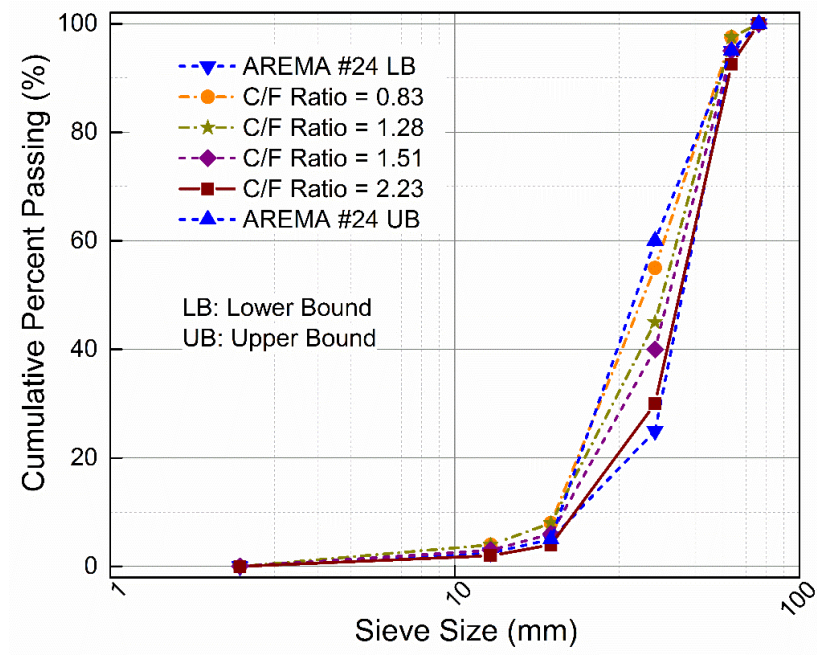


**Figure 3.24 Ballast Gradation used in this Research to Study the Effect of Coarse-to-Fine Ratio (for AREMA #24 Gradations)**

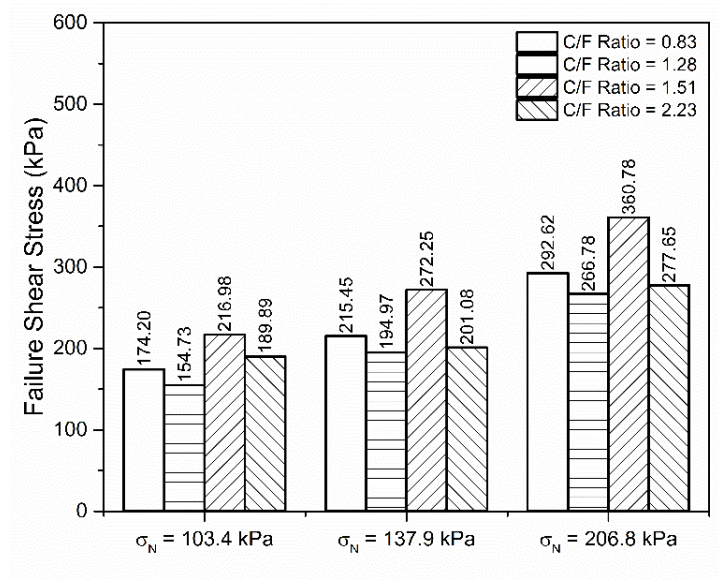


**Figure 3.25 Comparative Evaluation of Failure Shear Stress Showing the Effect of Coarse-to-Fine Ratio (for AREMA #24 Gradations)**

**Table 3.17 Comparative Evaluation of Angle of Internal Friction Showing the Effect of Coarse-to-Fine Ratio (for AREMA #24 Gradations)**

	<b>C/F Ratio</b>			
	<b>0.83</b>	<b>1.28</b>	<b>1.51</b>	<b>2.23</b>
$\phi$	56°	54°	62°	55°

Similarly, for AREMA #4 gradation, four different gradations corresponding to C/F ratio values of 1.04, 1.27, 1.88, and 2.93 were chosen (see Figure 3.26). Note that due to differences in the sieve sizes used to specify the gradation limits, it was not possible to generate gradations with the exact same C/F Ratio values within the AREMA #24 and AREMA #4 gradation bands. Significant effort was spent to ensure gradations with relatively close C/F Ratio values could be simulated for the two different ballast types. Figure 3.27 shows results obtained from DEM simulation of direct shear strength tests for the four different AREMA # 4 gradations. From the figure it is apparent that C/F = 1.27 yields the highest failure shear stress value. Corresponding friction angle ( $\phi$ ) values are listed in Table 3.18; the highest  $\phi$  value was obtained for the gradation with C/F = 1.27.

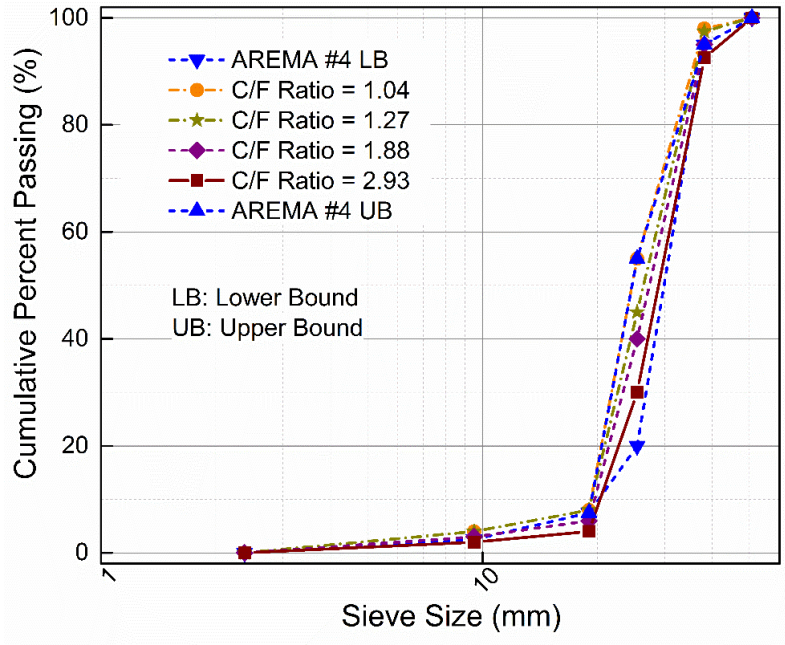


Figure 3.26 Ballast Gradation used in this Research to Study the Effect of Coarse-to-Fine Ratio (for AREMA #4 Gradations)

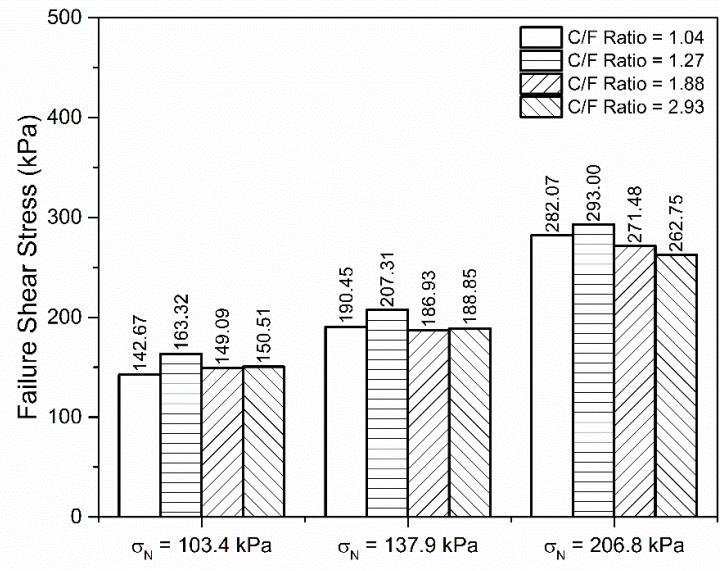


Figure 3.27 Comparative Evaluation of Failure Shear Stress Showing the Effect of Coarse-to-Fine Ratio (for AREMA #4 Gradations)

**Table 3.18 Comparative Evaluation of Angle of Internal Friction Showing the Effect of Coarse-to-Fine Ratio (for AREMA #4 Gradations)**

	C/F Ratio			
	1.04	1.27	1.88	2.93
$\phi$	54°	56°	53°	53°

From the results presented above, it is apparent that shear strength properties for both AREMA #24 and AREMA # 4 ballast materials were affected by the value of the C/F Ratio gradation parameter. However, maximum shear strength was achieved for the two ballast materials at different values of the C/F Ratio parameter (C/F = 1.51 for AREMA # 24; C/F = 1.27 for AREMA #4). Close inspection of the friction angle values (Tables 3.17 and 3.18) also establishes that the shear strength of AREMA #24 ballast was more sensitive to variations in the C/F Ratio value, compared to that for AREMA#4 ballast. No particular justification for this trend could be found during the current research effort.

### 3.6 Limitations of the Direct Shear Testing

This section highlights the limitations associated with the discrete element modeling of ballast direct shear strength tests as performed in the current study. The objective is to present avenues for improvements for follow-up research efforts.

1. In reality, ballast particles are irregular (polyhedral) in shape. In PFC3D<sup>®</sup>, the irregular shape of particles can be simulated using clumps where any number of overlapping spheres are connected together; this is not strictly a ‘true’ simulation of polyhedral particles. Another DEM software, BLOKS3D, developed at the University of Illinois (Zhao et al., 2006), uses rigid, non-deformable, three-dimensional polyhedrons or blocks as the basic elements to realistically simulate

interactions such as interlock/contact of actual angular particles. However, BLOKS3D is not commercially available for use. Use of ‘true’ polyhedral particles in place of clumps can lead to improved simulation results.

2. The surface texture (roughness) of individual particles is an important factor governing mechanical response of ballast, because it determines how well the particles slip past each another. DEM simulation is not capable of accommodating the surface texture of particles directly. For example, in PFC3D<sup>®</sup>, a rough particle texture is simulated by changing friction coefficient values assigned to individual particles. Note that these values have to be iteratively changed during model calibration efforts to ensure that the resulting stress-strain plots match those obtained from laboratory-tests.
3. All simulations of direct shear strength tests carried out during the current study correspond to dry conditions; ballast behavior under wet conditions was not considered. This assumption can be justified by the fact that all ballast gradations considered in the current study were relatively coarse in nature, and such materials are usually free draining; water accumulation in such materials generating excess pore water pressure is not commonly observed.
4. To reduce the computational effort required, fine particles are often excluded from DEM simulations. This is achieved by totally removing the fines from a particle-size distribution (Potyondy et al., 2016) or using higher particle-size distribution as large as 10 times from the actual gradation (Kim et al., 2014). One possible way of incorporating the lubricating effect of the fine particles between the coarse particles in the modeled system may involve reducing the friction coefficient value assigned

to individual particles. (Potyondy, 2016). Nevertheless, simulation of gradations containing all particle sizes is likely to result in improved predictions of material behavior.

### **3.7 Summary of Results of Direct Shear Strength Testing of Railroad Ballast**

This chapter presented details on DEM simulation of direct shear tests on railroad ballast. A summary of major findings from this effort is presented below.

1. For both AREMA #4 and AREMA #24 gradations, the finer gradation (UB) resulted in higher failure shear stress values compared to the coarser gradation (LB) for the two lower normal stress values (103.4 *kPa* and 137.9 *kPa*); the trend was reversed for the highest normal stress value (206.8 *kPa*).
2. Increasing the Flat and Elongated (F&E) ratio numbers led to significant increase in the ballast shear strength, with the maximum friction angle ( $\phi$ ) value approaching 81°. However, it should be noted that these results can be misleading as the simulations do not account for the breakage of flat and elongated particles under loading. In real world application, using flat and elongated particles can have detrimental effects on ballast shear strength (due to increased fouling caused by ballast breakage). Per the simulation results, in a case where the flat and elongated particles do not break under loading, significant increase in the shear strength may be realized.
3. Increasing the angularity of ballast particles led to significant increase in the ballast shear strength also reflected though increasing friction angle values. The simulation results showed that the maximum increase in shear strength is realized

as one moves from spherical particles to angular particles. Subsequent increase in the degree of angularity values does not lead to as drastic jumps on the friction angles.

4. As the aggregate top-size was varied from 38 to 76 mm, it was observed that the higher the aggregate top size, the higher the shear strength.
5. An increasing trend of failure shear stress and angle of internal friction was found with the increase in specimen specific gravity.
6. As the porosity value was increased, both the failure shear stress and the angle of internal friction decreased.
7. A higher coefficient of friction between the particles led to a higher shearing resistance and angle of internal friction angle values.
8. The failure shear stress increased with increase in applied normal stress values. An increase of 305% in the failure shear stress value was achieved as the normal stress was increased from 34.5 to 206.8 kPa .
9. The effect of particle packing on ballast shear strength was studied using a newly developed gradation parameter, referred to as the Coarse-to-Fine Ratio (C/F Ratio). DEM simulation results established that C/F values affected ballast shear strength behavior, with the effect being more significant for AREMA #24 compared to that for AREMA #4. C/F ratio of 1.51 exhibits the densest packing among the four gradations chosen in case of AREMA #24, which is evident from the failure shear stress for this C/F ratio. However, C/F ratio of 1.27 almost yields the best shear stress-displacement relations for all the different normal stresses of AREMA #4 gradation.

The next chapter (Chapter 4) of this document will present results from triaxial monotonic shear strength testing of railroad ballast.

## CHAPTER 4: DISCRETE ELEMENT MODELING OF TRIAXIAL MONOTONIC SHEAR STRENGTH TESTS

### **4.1 Introduction**

This chapter presents findings from DEM simulations of triaxial monotonic shear strength testing of railroad ballasts undertaken within the scope of this Master's Thesis effort. First, details on the procedure adopted to simulate triaxial monotonic shear strength tests on railroad ballast have been presented. The discussions include considerations related to specimen size selection method, specimen preparation, test variable selection, etc. This is followed by details on model calibration using laboratory-test data obtained from the literature. Subsequently, results from parametric analyses conducted to study the effects of different material, specimen, and test parameters have been presented. Finally, limitations associated with the DEM simulation of triaxial shear strength testing of railroad ballasts have been discussed.

### **4.2 DEM Simulation of Triaxial Monotonic Shear Strength Tests (TXT)**

The triaxial shear strength test is traditionally performed in the laboratory to evaluate the effects of monotonic and repeated loading on ballast behavior (Indraratna et al., 1998, 2009; Suiker et al., 2005; Aursudkij et al., 2009; Lu and McDowell, 2010; Qian et al., 2013, 2014, 2015; Mishra et al., 2014a; McDowell and Li, 2016; Ngo et al., 2016). Simulation of the triaxial shear strength tests carried out in this research effort was performed using a recently released "Material-Modeling Support Package" for PFC 5.0 (Potyondy, 2017a) as the basic framework. Details regarding the specimen preparation

and testing discussed in the following sections follow the basic framework provided in the technical a memorandum by Potyondy (2017a).

#### 4.2.1 Specimen Preparation and Testing

This section provides details about the specimen size used, ballast particle shapes and gradations simulated, and also the parameters specified during specimen preparation and testing using DEM. It should be noted that at first, a “primary” specimen was created, and tested under monotonic loading. Results from this test were compared against available laboratory-test data and the model parameters were adjusted in an effort to calibrate the model. Subsequently, different specimen and test parameters were varied to study their effects on the test results.

##### 4.2.1.1 Ballast Shape Used

The particle shapes used in this study using are shown in Figure 4.1, while the properties of the clump shapes are given in Table 4.1. Note that these shapes are based on a recent study conducted at the University of California, Berkeley, and are different from the ballast shapes used in Chapter 3 for DEM simulations of direct shear testing of railroad ballasts.

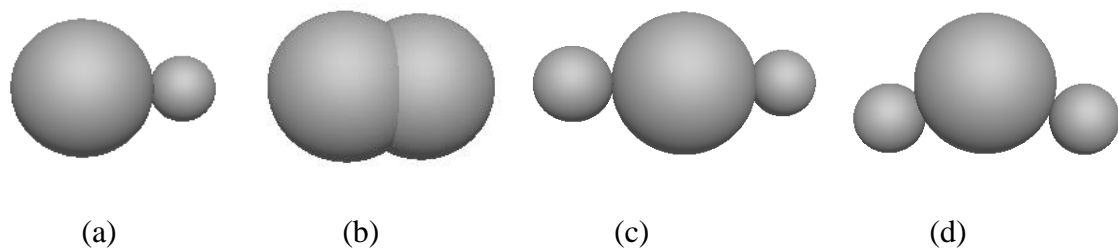


**Figure 4.1 Ballast Particle Shapes used for Discrete Element Modeling of Triaxial Shear Strength Tests in the Current Study: (a) 2-ball Clump\_1; (b) 2-ball Clump\_2; (c) 3-ball Clump\_1; and (d) 3-ball Clump\_2**

**Table 4.1 Relative Radius Magnitudes Associated with Different Ballast Shapes used in the DEM Simulations of Triaxial Shear Strength Tests**

<b>Ballast Particle Shape</b>	<b>Radius of balls in the clump</b>
2-ball Clump_1	$R_1 = 1.0; R_2 = 0.50$
2-ball Clump_2	$R_1 = 0.50; R_2 = 0.50$
3-ball Clump_1	$R_1 = 1.0; R_2 = 0.50; R_3 = 0.50$
3-ball clump_2	$R_1 = 1.0; R_2 = 0.50; R_3 = 0.50$

\*where  $R_1, R_2$ : Ball radius values specified in different clump templates

#### 4.2.1.2 Ballast Gradation Used

Just like the direct shear test simulations discussed in Chapter 3, the ballast gradations used to simulate triaxial shear strength tests conformed to AREMA #4, and AREMA #24 specifications. However, to reduce the computational effort required for models with very high number of particles, the gradations were truncated to exclude the finest particles. Note that this approach is consistent with that reported in the literature. Table 4.2 lists the percent passing individual sieve sizes for the different ballast gradations modeled.

**Table 4.2 Cumulative Percent Passing Individual Sieve Sizes for the Ballast Gradations used for Simulating Triaxial Shear Strength Tests**

Sieve Size (mm)	Sieve Size (in.)	#4 LB	#4 UB	#24 LB	#24 – 45%	#24 UB
		Cumulative Percent Passing (%)				
76.2	3	N/A	N/A	100	100	100
63.5	2.5	N/A	N/A	95	95	95
50.8	2	100	100	N/A	N/A	N/A
38.1	1.5	95	95	25	45	60
25.4	1	20	55	N/A	N/A	N/A
19	¾	7.5	7.5	5	5	5
12.7	½	N/A	N/A	0	0	0
9.51	3/8	0	2.5	N/A	N/A	N/A

#### 4.2.1.3 Contact Model Used

Particle-to-particle contact behavior during the triaxial test simulations was modeled using the recently developed Hill contact model (Potyondy, 2016), capable of simulating contact response for unsaturated granular materials. To simulate the contact behavior of two particles using the Hill model, the following input parameters need to be defined: (1) local radii of particles, (2) Young’s moduli, (3) Poisson’s ratios and densities of particles, (4) friction coefficient, (5) damping constant, and (6) moisture gap.

Originally developed to simulate the behavior of dense-graded aggregate bases, the Hill contact model accounts for the coarse particle-size distribution as well as the effects of moisture and fine particles (Tan et al., 2014).

The Hill contact model may exist only at a particle-particle contact that is simulated as the contact between two locally elastic spheres with a “liquid bridge”. The “liquid bridge” is meant to represent any moisture present in the granular matrix. The

liquid bridge is present if the moisture state is “wet”, and absent if the moisture state is “dry”. The Hill contact model provides the behavior of an infinitesimal, nonlinear elastic (no tension) and frictional interface that carries a compressive surface-interaction force and may carry a tensile moisture force (Figure 4.2). The contact force ( $F_c$ ) is the sum of the surface-interaction ( $F_s$ ) and moisture force ( $F_m$ ), and the contact moment ( $M_c$ ) is zero. Note that the surface-interaction force model is based on Hertz-Mindlin contact theory along with a damping mechanism and Coulomb sliding friction (Tsuji et al., 1992). The surface-interaction force consists of Hertzian and dashpot components with the Hertz-Mindlin springs acting in parallel with the dashpots (Potyondy, 2016). The moisture force ( $F_m$ ) is present only if the moisture state is wet; otherwise, it is equal to zero. The moisture effect is accounted for in the Hill material by considering the suction (negative pore pressure) associated with surface tension that holds pore water at the inter-particle contacts in unsaturated granular material. In-depth details of the Hill contact model can be found elsewhere (Potyondy, 2016).

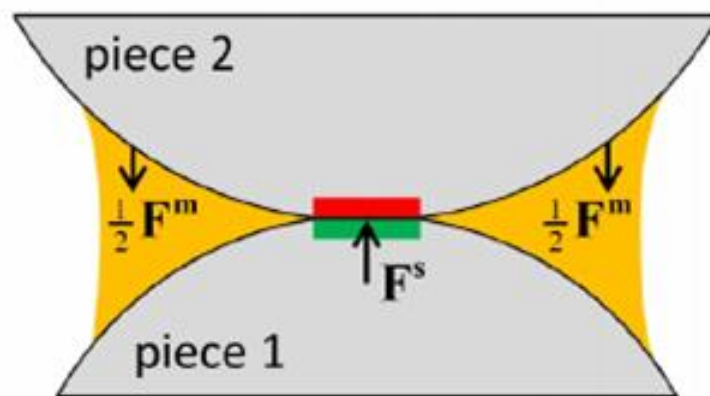


**Figure 4.2 Schematic Representation of the Hill Contact Model between Two Spheres (Potyondy, 2016)**

#### 4.2.1.4 Specimen Preparation

The first step in specimen preparation is known as the “Material Genesis” step. During this step, the granular matrix is created with a pre-defined contact type (Hill contact in this study). This step creates the specimen to be tested consisting of a homogeneous, isotropic and well-connected particle assembly with a specified non-zero material pressure (Potyondy, 2017a). In this study, a physical vessel having cylindrical shape was used (see Figure 4.3).

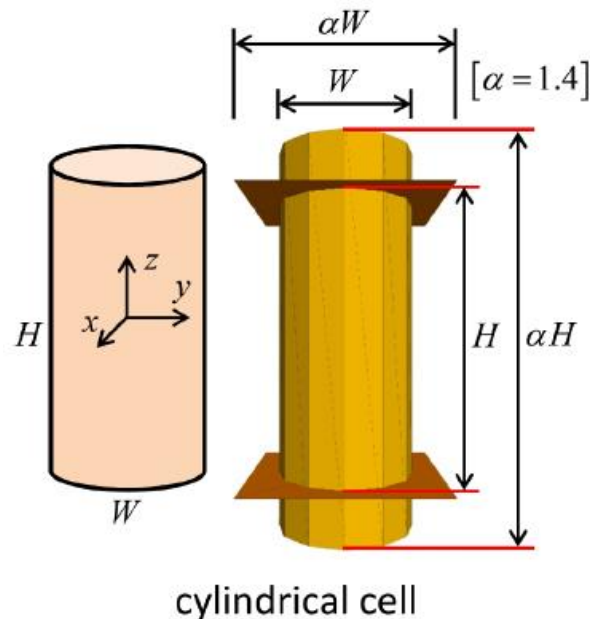


**Figure 4.3** Cylindrical Shaped Physical Vessel used in DEM Simulation of Triaxial Shear Strength Test (modified from Potyondy, 2017a)

The material-genesis procedure consists of two phases: a packing phase followed by a finalization phase (Potyondy, 2017a). The ‘boundary-contraction’ packing procedure, adapted from McDowell et al. (2006) was used in this study. In this procedure, confinement is applied by moving the vessel walls under control of the servomechanism. Note that the material friction coefficient chosen during confinement application (denoted

as  $\mu_{CA}$ ) can be adjusted to achieve a dense or loose packing configuration. The boundary-contraction procedure involves the following steps (Potyondy, 2017a):

1. Generate a cloud of particles having a porosity of  $n_c$ .  $n_c = \frac{V_v - V_g}{V_g}$ , where  $V_v$  is the volume of the material vessel and  $V_g$  is the total volume of grains. This porosity does not account for overlaps. In other words, the total volume of particles in the specimen is calculated by summing the volumes of individual particles; any overlaps between the generated particles is not taken into account. Therefore, the ‘actual’ porosity of the specimen at this stage is usually higher than the ‘cloud porosity’ specified during material genesis. This is later addressed in the next step by removing the overlap between particles. The particles are drawn from the specified size distribution, and then placed at arbitrarily chosen positions within bins that lie fully within the material vessel (i.e. the cylindrical shaped triaxial shear strength test box) such that there may be large particle-particle overlaps (Figure 4.4a).
2. Set the material friction coefficient to zero, and then allow the particles to rearrange until either the mean stress is near zero (within 0.1% of desired confinement,  $P_m$ ) or static-equilibrium is obtained. This step eliminates the large overlaps and should provide an isotropic state. Note that the static equilibrium is obtained if “mechanical a-ratio” falls below the specified equilibrium ratio or the number of steps exceeds the specified step limit. As previously mentioned, the “mechanical a-ratio” is the maximum unbalanced force magnitude (over all particles) divided by the average force intensity (over all particles). The unbalanced force is the vector sum of all

forces acting on the particle, and the force intensity is the sum of the force magnitudes. The specimen state at the end of this step is shown in Figure 4.4b.

3. Set the material friction coefficient to  $\mu_{CA}$ , and then apply confinement of  $P_m$  by moving the vessel walls under control of the servomechanism until the wall pressures are within the specified pressure tolerance of the material pressure and static-equilibrium has been obtained (Figure 4.4c). Note that setting  $\mu_{CA} = 0$  gives the densest packing, and progressively looser packing is obtained by increasing this.

It should be noted that as shown in the Figure 4.4, the porosity changes in every step, with the final porosity value at the end of Step 3 ( $n_c = 0.38$ ) being significantly lower than that at the end of Step 1 ( $n_c = 0.58$ ). From Figure 4.4 it can also be seen that significant amounts of particle overlap exist in Step 1; the overlap is gradually removed in Steps 2. The specimen at the end of Step 3 comprises particles that are closely packed under the pre-determined confining pressure (material pressure).

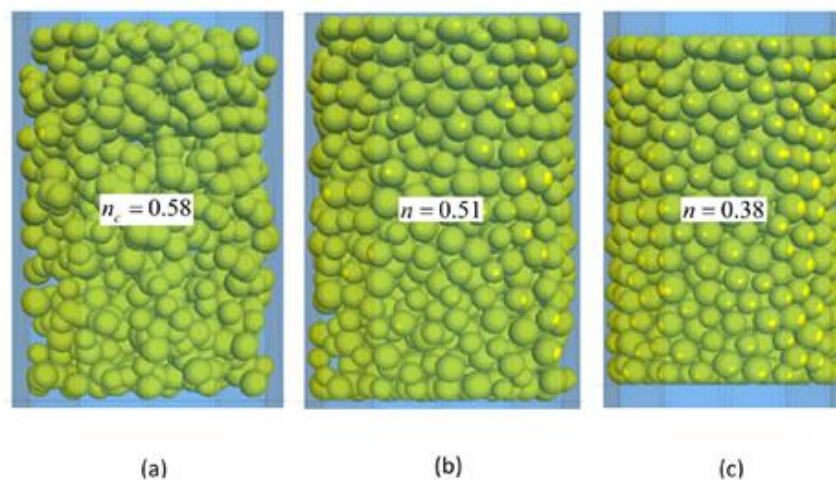


**Figure 4.4** Boundary-contraction Packing Procedure: (a) Initial Particle Cloud at End of Step 1, (b) Relaxed Particle Cloud at End of Step 2, and (c) Compacted Granular Assembly at End of Step 3 (Potyondy, 2017a)

The large-scale triaxial tests simulated in the current study comprised a cylindrical specimen consisting of two planar walls and a cylindrical wall having a diameter of  $305\text{ mm}$  ( $12\text{ in.}$ ) and height of  $610\text{ mm}$  ( $24\text{ in.}$ ). The top and bottom walls simulate top and bottom loading platens in a typical triaxial test set-up (see Figure 4.5). Note that the walls of the physical vessels were expanded to prevent particles from escaping if the walls are moved outwards during subsequent compression testing. Moreover, the wall-wall overlap was ignored, because within a PFC model wall-to-wall interaction is not taken into consideration.

For specimens formed in a physical vessel, the linear contact model was installed at the particle-wall contacts and the walls were kept frictionless. Clump-shaped ballast particles were generated conforming to target AREMA gradations. The Hill contact model was used for contact assignment. The model particle density and local damping ratios were chosen as  $2650\text{ kg/m}^3$  and 0.7, respectively (typical values found from literature). The cloud porosity of the assembly representing the initial condition of the test specimen was controlled at 0.58. The Young's modulus and Poisson's ratio of the particles were chosen to be  $29\text{ GPa}$  and 0.20, respectively. The friction coefficient was set to 0.6. The suction was  $0\text{ kPa}$  to simulate dry condition of the material. During the packing phase, the desired material pressure of  $150\text{ kPa}$  was obtained by boundary contraction packing procedure.

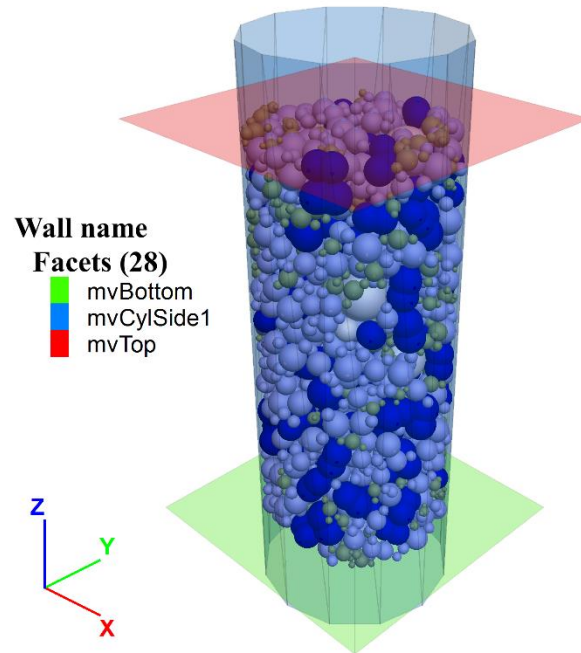


**Figure 4.5 Cylindrical Triaxial Monotonic Shear Strength Testing Specimen Generated using DEM (after Material-Genesis Procedure)**

#### 4.2.1.5 Triaxial Testing and Monitoring

Once the specimen with desired porosity and gradation was generated, the triaxial monotonic shear strength testing was performed by confining the specimen in all directions. The two planar walls (i.e. the top and bottom walls) acted as loading platens, and the velocities of the cylindrical walls were controlled by a servomechanism with a pressure boundary conditions in all directions to maintain pre-defined constant target confining pressure levels. The confining pressure levels simulated in this research effort were: 34.5, 68.9 and 103.4 *kPa* (5, 10 and 15 *psi*, respectively). Details about the servo-control mechanism can be found elsewhere (Itasca, 2016). Axial strain was applied by moving the axial walls at a specified strain rate of  $0.1 \text{ s}^{-1}$  while keeping the confining pressure constant. This strain rate is assumed to be slow enough to produce quasi-static response of the specimen. The loading was continued until the axial strain level achieved

equaled 5%. The deviator stress and the axial strain magnitudes were monitored throughout the loading phase.

#### 4.2.2 Model Calibration Using Laboratory-Test Data

Once the specimen preparation and testing procedures were finalized, the next task involved calibrating the model using laboratory-test data. The simulated model was calibrated using laboratory data extracted from research study conducted by Qian et al. (2013). The ballast material tested by Qian et al. (2013) was a clean limestone with 100% crushed aggregates. The particle-size distribution conformed to the typical

AREMA #24 ballast gradation having a coefficient of uniformity  $\left( C_u = \frac{D_{60}}{D_{10}} \right)$  of 1.46, a

coefficient of curvature  $\left( C_c = \frac{D_{30}^2}{D_{60} \times D_{10}} \right)$  of 0.97. The cylindrical large-scale triaxial test

specimen had dimensions of 305 mm (12 in.) diameter and 610 mm (24 in.) height. The target void ratio of 0.68 was achieved. The ballast samples were sheared under confining stress levels of 68.9, 137.8 and 206.7 kPa (10, 20 and 30 psi, respectively). The particle-size distribution used for model calibration is shown in Figure 4.6.

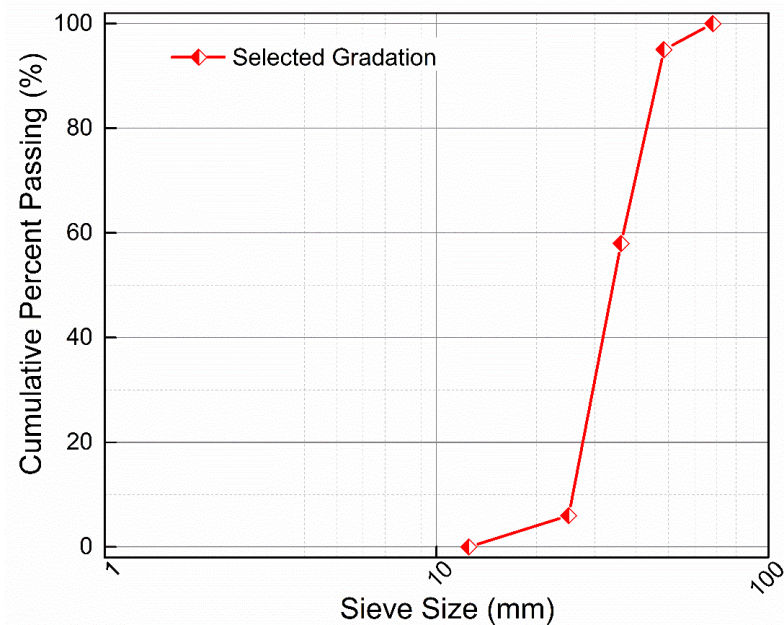


**Figure 4.6 Ballast Gradation Used in this Research Study for Triaxial Monotonic Shear Strength Testing Model Calibration using Lab Data**

While calibrating the model, the same ballast gradation, cylindrical specimen size, target void ratio as the laboratory were used. Figure 4.7 shows the particle-size distribution generated within PFC3D<sup>®</sup>. Other model parameters needed for the DEM simulation were adjusted in an effort to match the laboratory generated stress-strain curves, and have been listed in Table 4.3. The Hill material properties were set to Young's Moduli, and Poisson's ratios of  $29 \text{ GPa}$  and  $0.20$ , respectively. The friction coefficient of the hill material was set to  $2.0$ . An axial strain rate of  $0.35 \text{ s}^{-1}$  was used. The calibration procedure followed a trial-and-error approach with the model parameters varied between realistic boundaries. Figure 4.8 shows the results of model calibration using the laboratory-test data, where a close match between the laboratory-test and DEM simulation results was found. Once the model calibration was complete, different material, specimen, and test parameters were varied, and the resulting effects on ballast stress-strain behavior were studied.

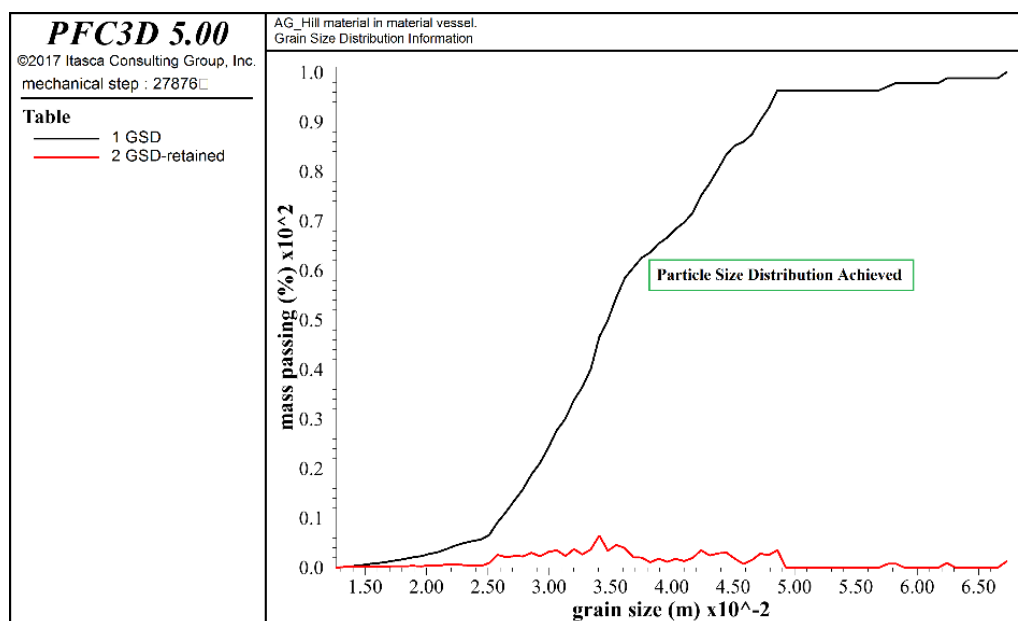


**Figure 4.7 Particle-Size Distribution Achieved during the Triaxial Monotonic Shear Strength Test Model Calibration**

**Table 4.3 Parameters used in Calibrating the DEM Model of Triaxial Monotonic Shear Strength Tests**

Model Parameters	Parameter Values Established after Model Calibration
Contact Model	Hill Contact
Specimen Size	305 mm (12 in.) diameter and 610 mm (24 in.) height
Young's Modulus	29 GPa
Poisson's Ratio	0.2
Friction Coefficient	2.0
Specific Gravity of Particles	2.65
Confining Pressure	68.9, 137.8 and 206.7 kPa (10, 20 and 30 psi, respectively)
Axial Strain Rate	0.35 s <sup>-1</sup>

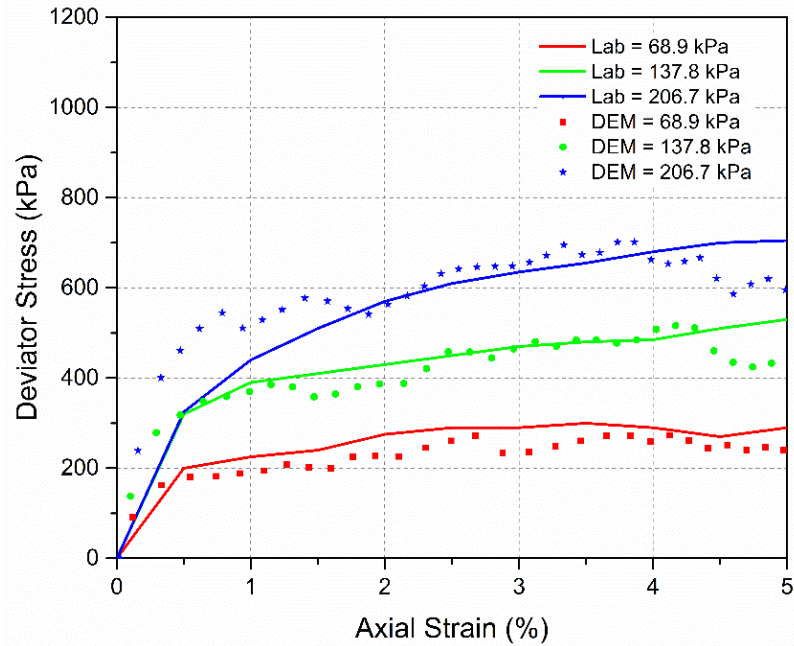


**Figure 4.8 Triaxial Monotonic Shear Strength Test Model Calibration Using Laboratory-Test Data**

### 4.3 Effect of Different Material, Specimen, and Test Parameters on Triaxial Shear Strength Test (TXT) Results

A series of triaxial test simulations were performed to determine the effects of different material (i.e. particle-size distribution), specimen, and test parameters on ballast shear strength behavior. Different test parameters studied were: (1) ballast specific gravity, and (2) porosity (after material genesis stage), (3) inter particle friction coefficient, and (4) applied confining pressure levels. As during the simulation of direct shear tests, the ballast gradation used during this parametric analysis was AREMA #24 – 45% (Table 3.2). All other model parameters, except for the one being evaluated, were kept constant at the values listed in Table 4.3. Mohr's circles were drawn from the shear strength data, and values of the shear strength parameters ( $c$  and  $\phi$ ) established (see Figure 4.9). For the figure shown, a cohesion intercept ( $c$ ) value of  $20\text{ kPa}$  and angle of

friction ( $\phi$ ) value of  $37^\circ$  was found. Note that non-zero values for the cohesion intercept ( $c$ ) can be attributed to linear interpolation of the non-linear failure envelope.

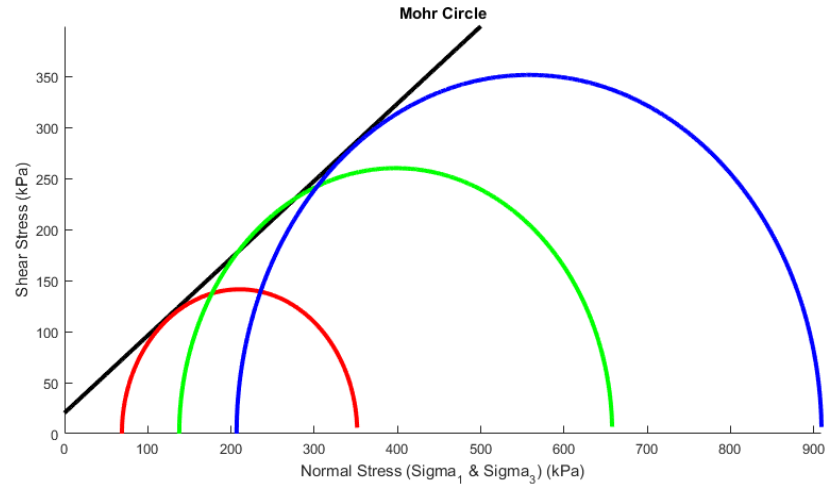
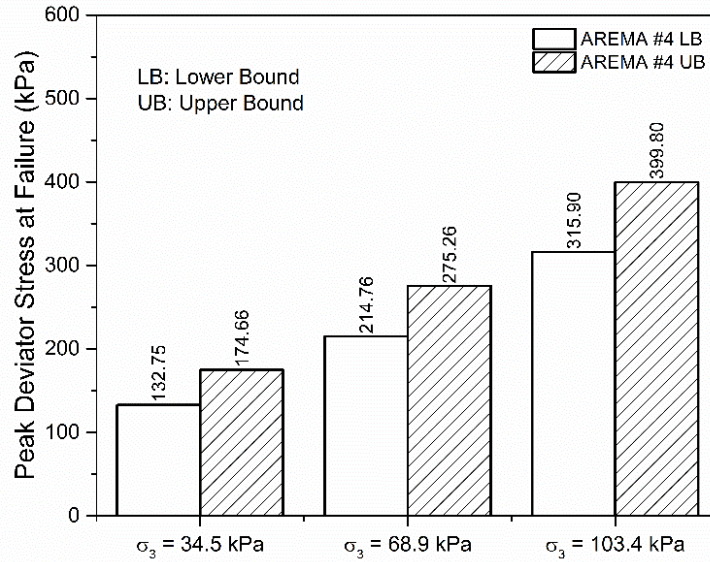


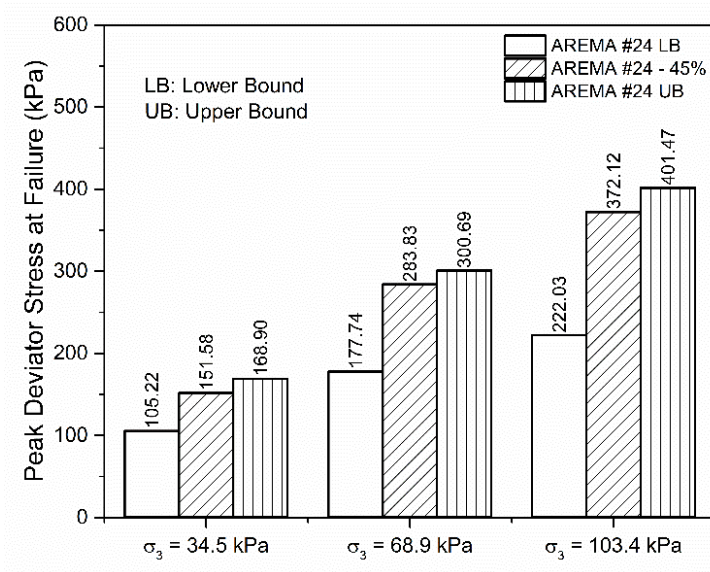
**Figure 4.9 Typical Mohr's Circle Drawn from Triaxial Monotonic Shear Strength Testing of Railroad Ballasts for Calculating the Shear Strength Parameters (Results Illustrated for the Calibrated Model using Lab Data)**

#### 4.3.1 Effect of Ballast Gradations

The effect of particle-size distribution (or gradation) was studied through simulation of five different ballast gradations falling under the AREMA specifications. When simulated, the number of particles for AREMA #4 LB, #4 UB, #24 LB, #24 - 45%, and #24 UB was 1724, 2501, 787, 864, and 1052 respectively. For both AREMA #4 and #24 gradations, the number of particles increased as one moved from the lower bound (coarse-end) of the gradation to the upper bound (fine-end) for the same top size. Figure 4.10 shows the comparative evaluation of the effects of gradation on the peak deviator stress (at failure) values measured through the simulated triaxial shear strength tests.



(a)



(b)

**Figure 4.10 Comparative Evaluation of Peak Deviator Stress at Failure for Two Different AREMA Gradations: (a) AREMA #4 and (b) AREMA #24**

As seen from Figure 4.10, the UB gradation consistently yields higher peak deviator stress at failure values compared to the LB gradation. This was observed for both AREMA #4 and AREMA #24 gradations. From Table 4.4, the angle of internal

friction value was found vary between  $35^\circ$  to  $38^\circ$  for AREMA #4, and  $34^\circ$  to  $39^\circ$  (for AREMA #24). Note that similar conclusions were drawn from the direct shear test results presented in Chapter 3 (for the two lower normal stress levels).

**Table 4.4 Comparative Evaluation of Shear Strength Parameters for Different Ballast Gradations**

	For AREMA #4		For AREMA #24		
	#4 LB	#4 UB	#24 LB	#24 - 45%	#24 UB
$c$ (kPa)	10	14	27	12	14
$\phi$	$35^\circ$	$38^\circ$	$34^\circ$	$38^\circ$	$39^\circ$

#### 4.3.2 Effect of Material Specific Gravity

The material specific gravity was varied from 2.6 to 2.7, and its effect on the railroad ballast shear strength was studied. As shown in Figure 4.11 and Table 4.5, no specific trend was observed from this parametric study, hence no conclusion could be inferred from this. However, an increasing trend of failure shear stress and angle of internal friction was found with the increase in material specific gravity in case of the direct shear test results as discussed in Chapter 3.

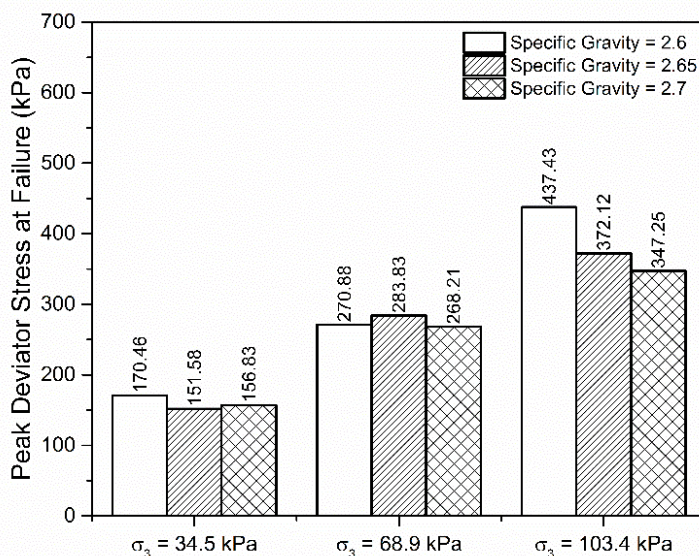


**Figure 4.11 Comparative Evaluation of Peak Deviator Stress at Failure Showing the Effect of Material Specific Gravity**

**Table 4.5 Comparative Evaluation of Shear Strength Parameters for Different Material Specific Gravity**

	Material Specific Gravity		
	2.6	2.65	2.7
$c$ (kPa)	6	12	17
$\phi$	41°	38°	35°

#### 4.3.3 Effect of Specimen Porosity

Specimen porosity is defined as the fraction of the total volume that is taken up by pore space. The effect of specimen porosity on the railroad ballast shear strength was studied by varying the specimen porosity within 0.40 to 0.48 while keeping the other parameters constant. From the results (Figure 4.12 and Table 4.6), it can be seen that as the porosity increases, the values of both the peak deviator stress (at failure) and the angle of internal friction decrease. Similar trends were found from the direct shear test simulations, and have been presented in Chapter 3.

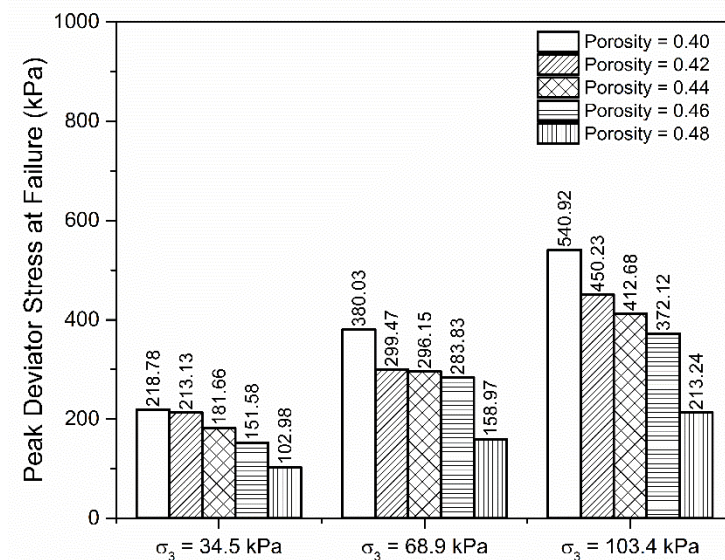


**Figure 4.12 Comparative Evaluation of Peak Deviator Stress at Failure Showing the Effect of Specimen Porosity**

**Table 4.6 Comparative Evaluation of Shear Strength Parameters for Different Specimen Porosity**

	Specimen Porosity				
	0.40	0.42	0.44	0.46	0.48
$c$ (kPa)	12	20	16	12	15
$\phi$	44°	39°	39°	38°	26°

#### 4.3.4 Effect of Coefficient of Inter-Particle Friction

The coefficient of inter-particle friction was varied from 1.0 to 3.0, and its effect on the ballast shear strength behavior was studied. Figure 4.13 shows the results from this parametric analysis. As seen from the figure, as the ball-ball friction coefficient increases, the peak deviator stress (at failure) also increases. Besides, for any ball-ball friction coefficient value, the peak deviator stress (at failure) value increases with the increase in the applied confining pressure. Table 4.7 lists the angle of internal friction angle values

for the same tests; the  $\phi$  value was found to vary between  $31^\circ$  to  $38^\circ$ . Similar trends for the direct shear tests were reported in Chapter 3.

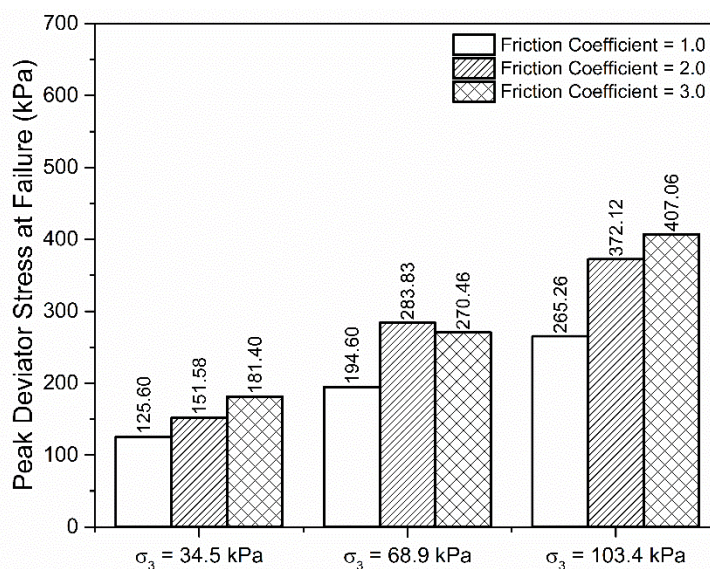


**Figure 4.13 Comparative Evaluation of Peak Deviator Stress at Failure Showing the Effect of Inter-particle Friction Coefficient**

**Table 4.7 Comparative Evaluation of Shear Strength Parameters Showing the Effect of Coefficient of Inter-particle Friction**

	Coefficient of Inter-particle Friction		
	1.0	2.0	3.0
$c$ (kPa)	16	12	17
$\phi$	$31^\circ$	$38^\circ$	$38^\circ$

#### 4.3.5 Effect of Applied Confining Pressure Levels

The confining pressure value was varied between  $34.5 \text{ kPa}$  ( $5 \text{ psi}$ ) to  $206.8 \text{ kPa}$  ( $30 \text{ psi}$ ), and the resulting effect on ballast shear strength behavior was studied. As shown in Figure 4.14, the peak deviator stress (at failure) increases with increasing confining pressure levels. Similar trends were reported by Indraratna et al. (1998);

Aursudkij et al. (2009); Lu and McDowell (2010); Qian et al. (2013). Increasing the confining pressure from 34.5 *kPa* to 206.8 *kPa* led to a 334% increase in the peak deviator stress value at failure.

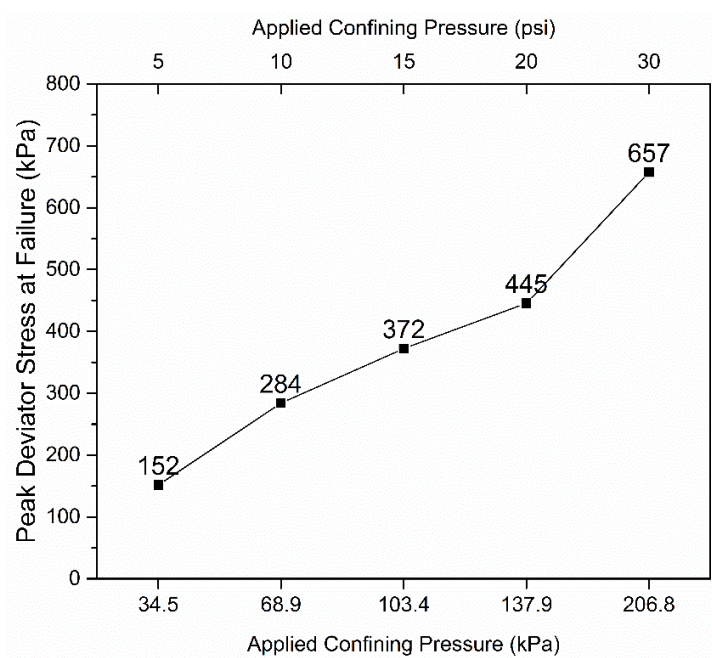


**Figure 4.14 Comparative Evaluation of Peak Deviator Stress at Failure Showing the Effect of Applied Confining Pressure Levels**

#### 4.3.6 Effect of Moisture (Suction Pressure)

As previously mentioned, the Hill contact model used in this study is capable of accounting for moisture effects in the granular matrix. The effect of moisture (suction pressure) on the ballast shear strength was studied by varying the suction pressure value from 10 to 30 *kPa*. For this parametric analysis, the ballast gradation used corresponded to the gradation used during the model calibration. As shown in Figure 4.15, the peak deviator stress (at failure) increases with increasing suction pressure values. Table 4.8 lists the shear strength parameter ( $c$  and  $\phi$ ) values for the same tests. The angle of internal friction angle was found to be within the range of 34° to 40°. Note that some of

the trends observed for the friction coefficient ( $\phi$ ) values are different from those observed for the peak deviator stress at failure. This is primarily due to the fact that the shear failure envelop is represented using two shear strength parameters ( $c$  and  $\phi$ ), and increase in the ballast shear strength may be reflected by increase in value of either or both of these parameters.

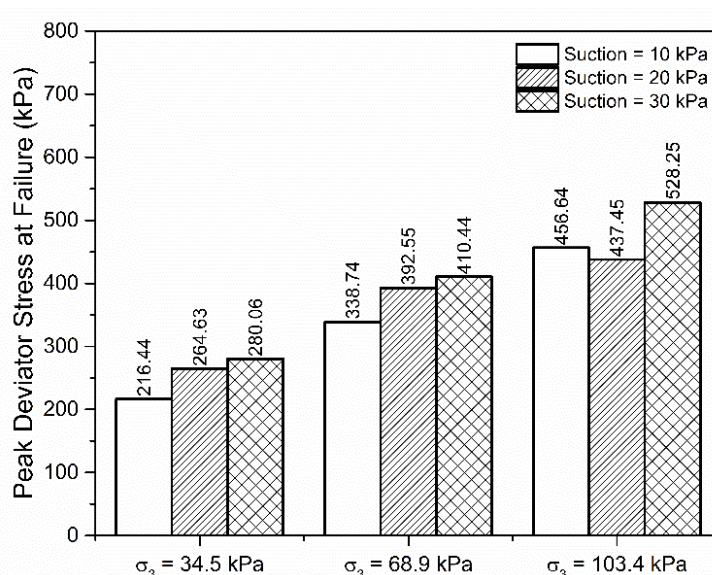


**Figure 4.15 Comparative Evaluation of Peak Deviator Stress at Failure Showing the Effect of Applied Suction Pressure (Results Illustrated for the Calibrated Model using Lab Data)**

**Table 4.8 Comparative Evaluation of Shear Strength Parameters Showing the Effect of Suction Pressure (Results Illustrated for the Calibrated Model using Lab Data)**

	Suction Pressure ( <i>kPa</i> )		
	10	20	30
$c$ ( <i>kPa</i> )	22	51	37
$\phi$	39°	34°	40°

#### 4.4 Limitations of the Triaxial Monotonic Shear Strength Testing of Railroad Ballast

The DEM simulation of triaxial monotonic shear strength testing on railroad ballast undertaken in this research effort has the following limitations.

1. In reality, ballast particles are irregular (polyhedral) in shape. In PFC3D<sup>®</sup>, the irregular-shaped particles can be simulated using clumps where any number of overlapping spherical ballast are connected together, which still is a limitation of this DEM tool. The use of ‘true polyhedral’ particles may improve the model accuracy.
2. As discussed in Chapter 3, the surface texture of individual particles is accommodated by adjusting the inter-particle friction coefficient values, which is not necessarily a true simulation of particle interaction. The inter-particle friction coefficient values need to be iteratively changed during model calibration efforts to ensure that the resulting stress-strain plots match those obtained from laboratory-tests (McDowell et al., 2006, Chen et al., 2013). Significantly high friction coefficient values ( $\mu = 2.0$ ) were used during the triaxial test simulations to ensure a reasonable match with the laboratory-generated stress-strain curves.
3. A much higher value of axial strain rate ( $0.35 \text{ s}^{-1}$ ) was used during this research effort to match the peak deviator stress values at different confining pressure observed during laboratory testing. This may present a significant deviation from reality as small strain rates should ideally be chosen to ensure quasi-static conditions throughout the shearing process.

#### 4.5 Summary of Results of Triaxial Monotonic Shear Strength Testing of Railroad Ballast

Findings Findings from the DEM simulation of triaxial monotonic shear strength tests on railroad ballast are summarized below.

1. For both the AREMA #4 and AREMA #24 gradation, the UB (fine-end) of the gradation showed consistently higher shear strength values compared to the LB (coarse-end).
2. No particular trend was observed concerning the effect of material specific gravity on ballast shear strength.
3. As the porosity value was increased, both the peak deviator stress (at failure) and the angle of internal friction decreased.
4. A higher coefficient of friction between the particles led to a higher peak deviator stress (at failure) value.
5. The peak deviator stress (at failure) value increased with increasing confining stress levels. An increase of 334% in the peak deviator stress (at failure) value was achieved as the confining pressure was increased  $34.5 \text{ kPa}$  ( $5 \text{ psi}$ ) to  $206.8 \text{ kPa}$  ( $30 \text{ psi}$ ).
6. As the suction pressure (moisture) value was increased, the peak deviator stress (at failure) increased.

#### 4.6 Comparison of Parametric Study Results of Direct Shear Testing and Triaxial Monotonic Shear Strength Testing on Railroad Ballast

Primary findings from DEM simulations of direct shear strength tests (reported in Chapter 3) and triaxial monotonic shear strength tests (reported in this chapter) on railroad ballast are tabulated below (Table 4.9).

**Table 4.9 Comparison of Parametric Study Results of Direct Shear Testing and Triaxial Monotonic Shear Strength Testing on Railroad Ballast**

<b>Parametric Study</b>	<b>Direct Shear Testing</b>	<b>Triaxial Monotonic Shear Strength Testing</b>
Effect of Ballast Gradations	For both AREMA #4 and #24, the UB results in higher failure shear stresses compared to the LB for normal stress levels of 103.4 <i>kPa</i> and 137.9 <i>kPa</i> ; the trend was reversed for the highest normal stress value (206.8 <i>kPa</i> ).	For both AREMA #4 and #24 materials, the UB gradation resulted in higher shear strengths compared to the LB gradation.
Effect of Flat & Elongated Ratio	Increasing the Flat and Elongated (F&E) ratio numbers led to significant increase in the ballast shear strength.	N/A
Effect of Particle Angularity	Increasing the angularity of ballast particles led to significant increase in the ballast shear strength also reflected though increasing friction angle values.	N/A
Effect of Aggregate Top-Size	With the increase in aggregate top-size, shear strength values increases.	N/A

<b>Parametric Study</b>	<b>Direct Shear Testing</b>	<b>Triaxial Monotonic Shear Strength Testing</b>
Effect of Material Specific Gravity	Increasing trend of failure shear stress and angle of internal friction was found.	No specific trend was observed.
Effect of Specimen Porosity	As the porosity increases, both the failure shear stress and the angle of internal friction decreases.	As the porosity increases, both the peak deviator stress (at failure) and the angle of internal friction decreases.
Effect of Inter-Particle Friction Coefficient	Increasing trends in failure shear stress and angle of internal friction were observed with increasing inter-particle friction coefficient values.	Increasing trends in peak deviator stress (at failure) were observed with increasing inter-particle friction coefficient values.
Effect of Normal Stress (Direct Shear) and Confining Pressure (Triaxial)	The failure shear stress increased with increase in applied normal stress values.	The peak deviator stress (at failure) value increased with increasing confining stress levels.
Effect of Moisture (Suction Pressure)	N/A	As the suction pressure was increased, the peak deviator stress (at failure) increased.

The next chapter (Chapter 5) of this thesis will present the simulation results from geogrid embedded cyclic triaxial testing on railroad ballast.

CHAPTER 5: DISCRETE ELEMENT MODELING OF GEOGRID  
EMBEDDED CYCLIC TRIAXIAL TESTING

**5.1 Introduction**

This chapter presents findings from different tasks undertaken under the scope of this Master's Thesis effort to study the mechanism of geogrid-ballast interaction, and effect of geogrid reinforcement on ballast resilient modulus. First, details on the procedure adopted to simulate cyclic triaxial testing of geogrid-embedded ballast specimens have been presented. The discussions include descriptions related to DEM modeling of geogrid, specimen-size selection, specimen preparation, test variable selection, etc. Subsequently, results from parametric analyses on geogrid-ballast interaction have been presented by changing different test variables; the effect of geogrid on ballast performance has been quantified using the 'Geogrid Gain Factor'. Finally, limitations associated with the modeling approach adopted in the current study have been discussed.

**5.2 DEM Simulation of Geogrid Embedded Cyclic Triaxial Testing**

Simulation of cyclic triaxial testing on geogrid-embedded railroad ballast specimens carried out in this research effort was performed using a recently released "Pavement-Design Package" for PFC 5.0 as the basic framework (Potyondy, 2017b). This package offers the following capabilities:

1. Simulation of cyclic triaxial testing of synthetic unsaturated granular materials such as railroad ballasts under both unreinforced and geogrid-reinforced conditions (see

Figure 5.1). Effect of geogrid reinforcement on ballast performance is quantified using a ‘Geogrid Gain Factor’; detailed description of the geogrid gain factor was presented in Section 2.6.2.

- Both the small-strain cyclic triaxial tests and large-strain monotonic triaxial shear strength tests can be simulated using this package.

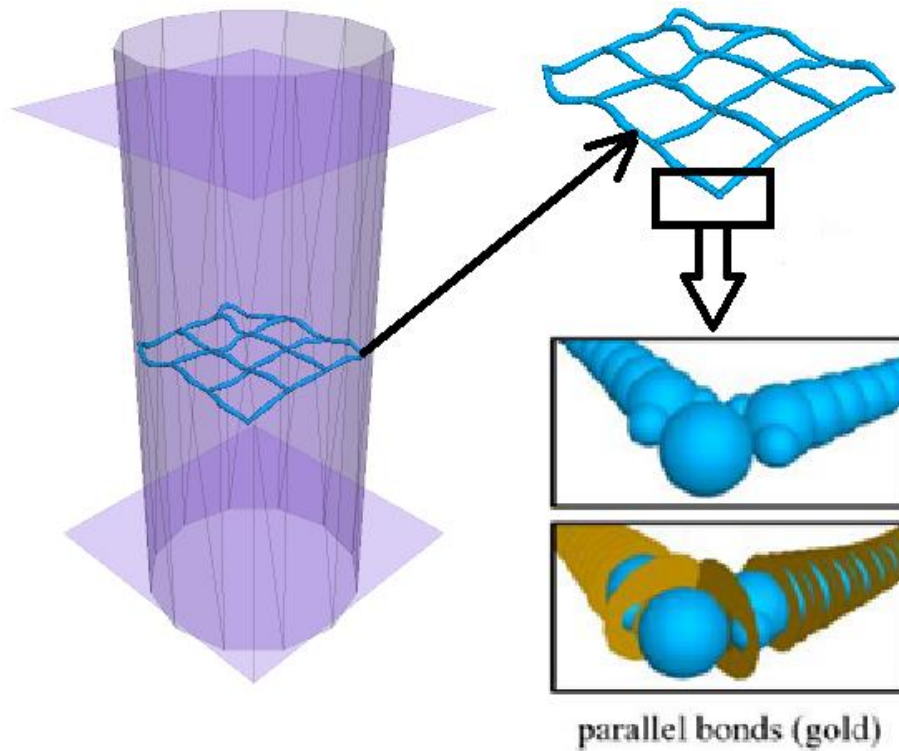


**Figure 5.1 DEM Simulation of Cyclic Triaxial Testing on Geogrid-Embedded Ballast Specimens (Illustrates Model State after the Test is Complete) (adopted from Potyondy, 2017b)**

Further details about the “Pavement-Design Package” (pdPkg) can be found elsewhere (Potyondy, 2017b).

### 5.2.1 Specimen Preparation and Testing

A typical geogrid-reinforced railroad ballast specimen was modeled for cyclic triaxial testing, and the effect of geogrid inclusion was quantified through the calculation of the geogrid gain factor. For the reinforced configuration, the geogrid is embedded in the specimen, while for the unreinforced condition; the specimen is tested without the geogrid. The following sections present brief discussions on the geogrid modeling methodology followed by the specimen preparation approach. Finally, the cycling testing procedure will be outlined, along with relevant results.

#### 5.2.1.1 Geogrid Modeling

The grid-modeling methodology incorporated in the ‘pdPkg’ is based on the procedures reported in the literature by Jas et al. (2015); Stahl and te Kamp (2012, 2013); Stahl et al. (2014); Stahl and Konietzky (2011); and Konietzky et al. (2004). Both biaxial and triaxial geogrids can be modeled. Each biaxial grid junction consists of two intersecting ribs, whereas each triaxial grid junction consists of three intersecting ribs.

There are five types of contacts in the modeled system comprising geogrids: (1) particle-particle, (2) grid-grid, (3) grid-particle, (4) grid-wall and (5) particle-wall. The version of ‘pdPkg’ used, was capable of modeling the particles (i.e. aggregates and ballasts) as spherical shaped balls only. These particles interact with one another via the Hill contact model, and thus the synthetic material is denoted as a ‘Hill material’. On the other hand, the geogrid is modeled as strings of overlapping spherical balls joined by parallel bonds (see Figure 5.1). The parallel bonds provide the structural properties of the grid, and the spherical balls provide the grid surface for grid-particle interaction. The simulated grid behaves like an elastic body, which will not break, and will return to its

original shape when unloaded. The parallel-bond and linear contact models are described elsewhere (Itasca, 2016). Incorporation of the triaxial geogrid has been introduced in the very recent update of the ‘pdPkg’. In this research study, only the biaxial geogrids were modeled. The grid material properties were taken from Stahl and te Kamp (2013) and are listed in Table 5.1.

**Table 5.1 Parameters Used in the DEM Simulations of Geogrid (Stahl and te Kamp, 2013)**

<b>Model Parameters</b>	<b>Values</b>
Grid Aperture Size	39 mm (square), 65 mm (square)
Grid Density	980 kg/m <sup>3</sup>
Grid Effective Modulus	700 MPa
Grid Stiffness Ratio	2.0
Grid-Particle Effective Modulus	500 MPa
Grid-Particle Stiffness Ratio	2.0
Grid-Particle Friction Coefficient	0.5
Local Damping Factor	0.7

Note that the grid effective modulus was chosen as 700 MPa, which is approximately one-half of the effective modulus for polypropylene (typically 1.5 to 2.0 GPa) (Wikipedia, 2015). The structural properties of the grid (quantified by the rib tensile stiffness and the junction torsional stiffness) match those of a Tensar SS20 biaxial geogrid (Potyondy, 2017b). The following figure (Figure 5.2)

shows an undeformed configuration of a biaxial geogrid having a square aperture size of  $65\text{ mm}$ .

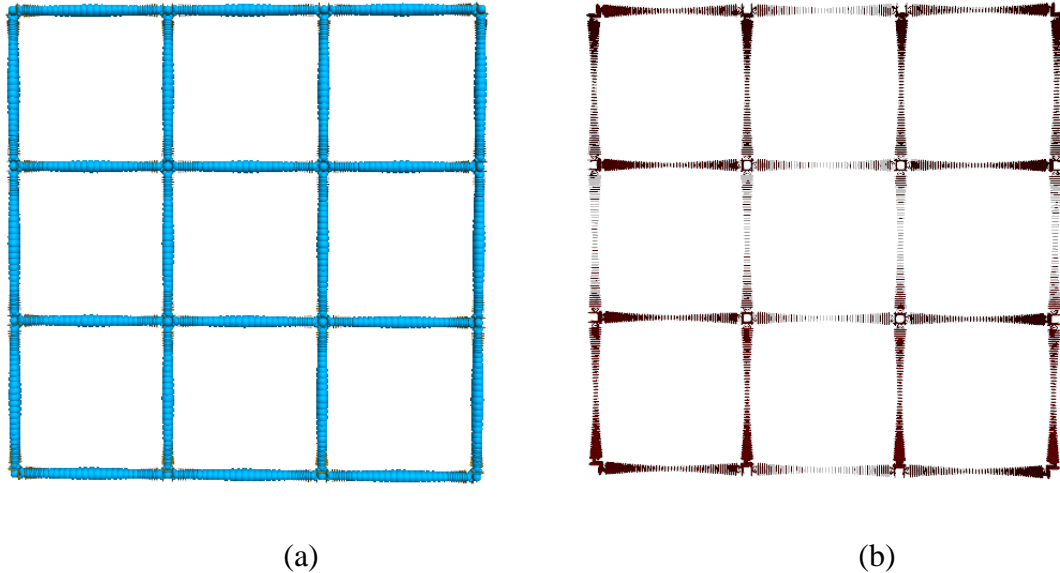


**Figure 5.2 Undeformed Configuration of a Grid Layer (a) Showing Grid Balls, and (b) Grid Bonds**

#### 5.2.1.2 Specimen Preparation

Specimen preparation for the unreinforced configuration follows the same procedure as described earlier in Section 4.2.1. However, for the reinforced configuration, the material-genesis procedure of Potyondy (2017a) is modified to embed a well-interlocked geogrid in a granular material. The boundary-contraction packing procedure to support geogrid inclusion involves the following steps (Potyondy, 2017b):

1. The first step is to create the grid set in its initial, undeformed configuration within the cylindrical shaped triaxial testing specimen, and constrain the grid by fixing the grid balls so that they cannot translate or rotate. The grid remains constrained during the next three steps (i.e. step 2 to 4), during which the grid does not move or deform while the grains flow around the grid.

2. Generate a cloud of particles having a porosity of  $n_c$ .  $n_c = \frac{V_v - V_g}{V_g}$ , where  $V_v$  is the volume of the material vessel and  $V_g$  is the total volume of grains. As previously described in Chapter 4, this porosity does not account for particle overlaps. The particles are drawn from the specified size distribution, and then placed at arbitrarily chosen positions within bins that lie fully within the material vessel (i.e. the cylindrical triaxial test device) such that there may be large particle-particle overlaps. Note that the simulated particles do not overlap an exclusion region that surrounds each grid (see Figure 5.3a).
3. Set the material friction coefficient to zero, and then allow the particles to rearrange until either the mean stress ( $\sigma_m$ ) is near zero (within 0.1% of desired confinement,  $P_m$ ) or static-equilibrium is obtained. This step eliminates the large overlaps by allowing the particles to move apart and flow uniformly into the grid apertures from above and below, and should provide an isotropic state of the material at the end of this step (see Figure 5.3b).
4. Set the material friction coefficient to  $\mu_{CA}$ , and then apply confinement of  $P_m$  by moving the vessel walls under control of the servomechanism until the wall pressures are within the specified pressure tolerance of the material pressure and static-equilibrium has been obtained (see Figure 5.3c). Note that setting  $\mu_{CA} = 0$  gives the densest packing, and progressively looser packing is obtained by increasing the value of this parameter.
5. Finally, in the step 5, the grid constraint is removed by freeing the grid balls so that they can translate and rotate (see Figure 5.3d). Again, step 4 is repeated to allow

the grid to move and deform in response to the compressive forces imposed by the particles.

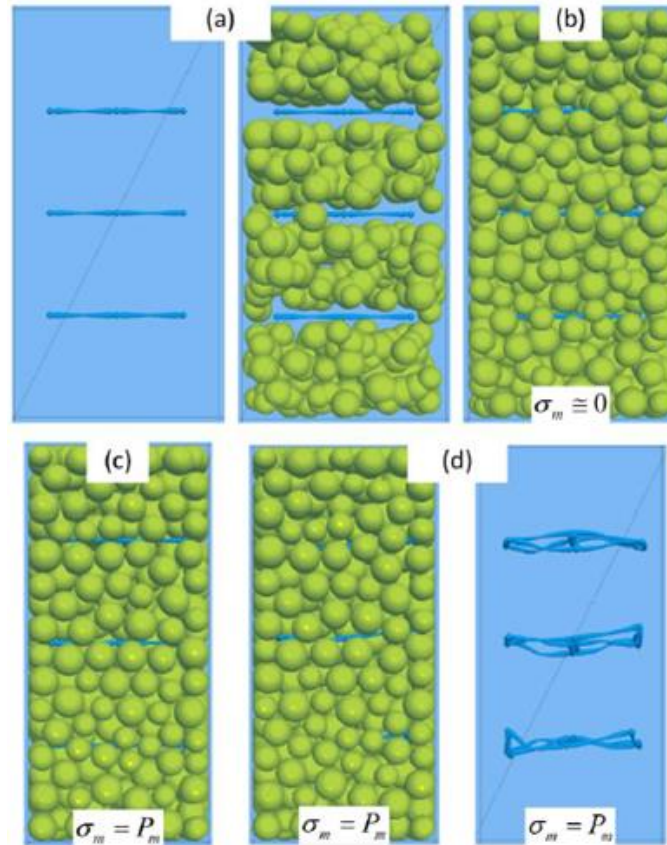


**Figure 5.3 Grid-embedment Procedure: (a) Constrained Grid and Initial Particle Cloud at End of Step 2, (b) Constrained Grid and Relaxed Particle Cloud at End of Step 3, (c) Constrained Grid and Compacted Granular Assembly at End of Step 4, and (d) Unconstrained and Deformed Grid at End of Step 5 (Potyondy, 2017b)**

For the reinforced configuration, the large-scale triaxial test specimen was a cylindrical shaped box consisting of two planar walls (one at the top, and one at the bottom) and a cylindrical wall with 305 mm (12 in.) diameter and 610 mm (24 in.) height; the geogrid was embedded at mid-depth of the specimen (see Figure 5.4). Spherical shaped ballast particles were generated maintaining the AREMA gradations with a typical ballast specific gravity of 2.6. The Hill contact model was assigned to

particle-particle contacts. The Young's modulus and Poisson's ratio, and friction coefficient values were set to  $70 \text{ GPa}$ ,  $0.25$ , and  $1.2$ , respectively. The suction pressure was set to  $30 \text{ kPa}$  to simulate wet conditions. The damping constant was zero, because quasi-static conditions were enforced via local damping, with a local-damping factor of  $0.7$ . The initial cloud porosity of the sample was set to  $0.376$ . During the packing phase, the desired material pressure of  $150 \text{ kPa}$  was obtained by boundary contraction packing procedure described earlier. The model parameters used for this DEM simulation are listed in Table 5.2.

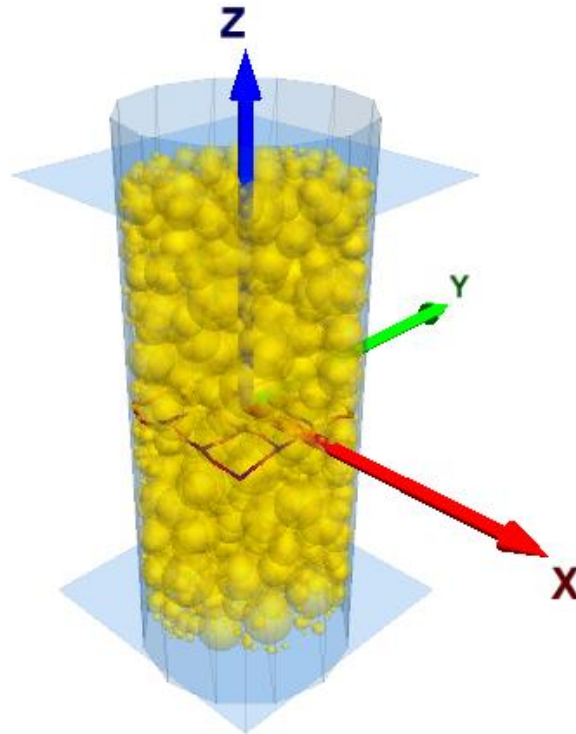


**Figure 5.4** Geogrid Embedded Cylindrical Triaxial Shear Strength Test Specimen Simulated using DEM

**Table 5.2 Parameters Used in the DEM Simulations of Geogrid Embedded Cyclic Triaxial Testing of Railroad Ballasts**

Model Parameters	Values
Specimen Size	305 mm (12 in.) diameter and 610 mm (24 in.) height
Particle-Size	AREMA#4, AREMA#24
Young's Modulus	70 GPa
Poisson's Ratio	0.25
Friction Coefficient	1.2
Initial Cloud Porosity	0.376
Material Pressure	150 kPa
Specific Gravity of Ballast	2.6

#### 5.2.1.3 Cycling Triaxial Testing

The two planar walls on top and bottom of the specimen acted as loading platens, and the velocities of the cylindrical walls were controlled by a servomechanism with a pressure boundary condition in all directions to maintain a constant target confining pressure level of 150 kPa. Axial strain was applied by moving the axial walls (i.e. top and bottom planar walls) at a specified strain rate of  $0.01 \text{ s}^{-1}$  while keeping the confining pressure constant; deviator stress and the axial strain values were monitored throughout the shearing process. Each simulated cyclic triaxial test comprised five load-unload cycles performed at different axial strains: (i) axial strain = 0.05% (two cycles); (ii) axial strain = 0.10% (two cycles); and, (iii) axial strain = 0.20% (one cycle). During each load-

unload cycle, the ballast resilient modulus was calculated as a secant modulus of the hysteretic curve. Figure 5.5 shows a typical deviator stress vs axial strain plot generated during cyclic triaxial testing of a geogrid-embedded ballast specimen.

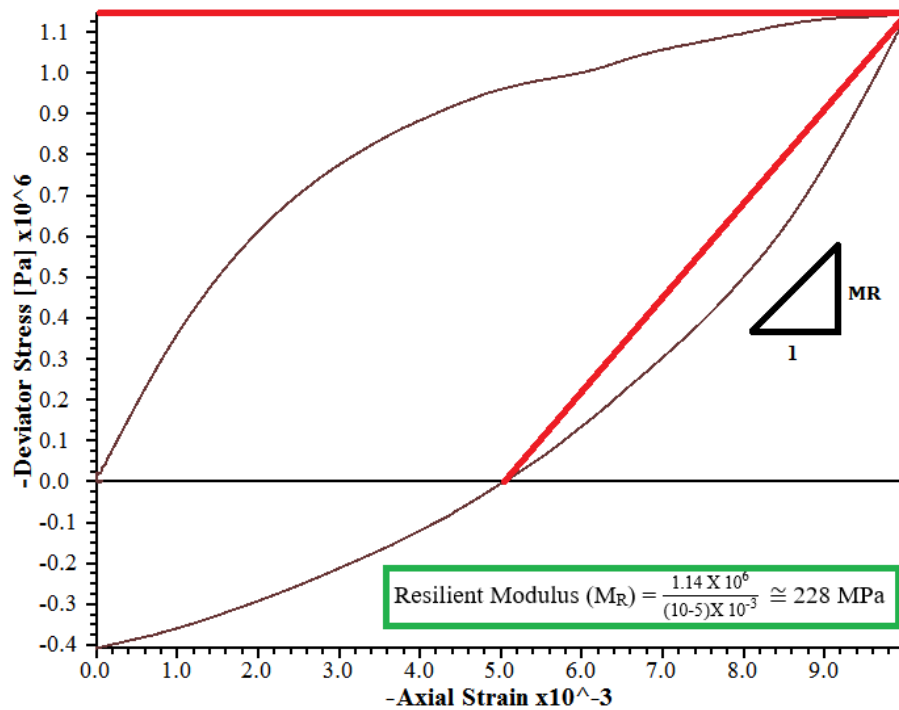


**Figure 5.5** Typical Deviator Stress vs Axial Strain Plot from Cyclic Triaxial Testing on a Geogrid-Embedded Ballast Specimen

### 5.2.2 Calculation of Geogrid Gain Factor

Once the resilient-modulus values were found, value of the geogrid gain factor was calculated following the procedure described below (Potyondy, 2017b).

1. By varying  $\mu_{CA}$  from zero to a non-zero value, two distinct curves for Resilient Modulus ( $M_R$ ) vs. porosity ( $n$ ) were obtained: (1) one for the unreinforced configuration, and (2) the other for the reinforced configuration. The curve corresponding to the unreinforced configuration lied beneath that for the reinforced

configuration (see Figure 5.6). As shown in this figure,  $\mu_{CA}$  values were set to 0.1, 0.35, and 0.6 to attain different porosity values.

2. When  $\mu_{CA}$  was set to a certain non-zero value, the material porosity of the unreinforced specimen was found to be less than that of the reinforced specimen. This may be because inclusion of the geogrid in the specimen inhibits the packing process, forming a local region that is more porous than the surrounding region, and thereby increasing the overall material porosity (Potyondy, 2017b).
3. For the calculation of geogrid gain factor, the resilient-modulus value at any axial strain level was compared between unreinforced and reinforced specimens corresponding to the same material porosity level (see Figure 5.6). Depending on confinement and moisture conditions, a geogrid gain factor value between 1.0 and 2.5 were reported by Potyondy et al. (2016) and Siekmeier et al. (2016). Note that both these studies focused on the simulation of aggregate base materials for pavement applications.

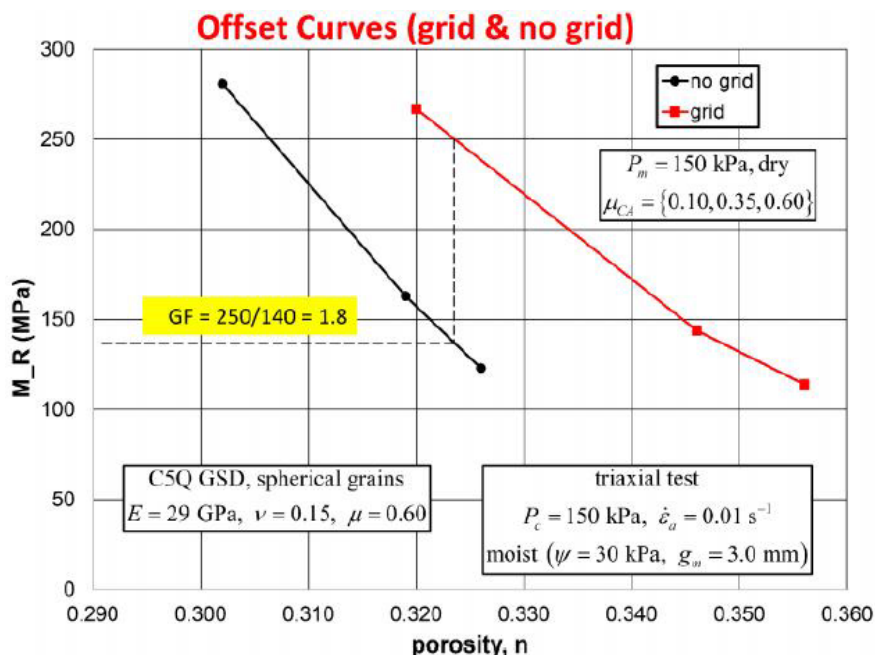


**Figure 5.6 Resilient-Modulus versus Porosity for Reinforced and Unreinforced Configurations Models Varying Friction Coefficient Values, Tested under Moist Conditions at 150 kPa Confinement (after Potyondy, 2017b)**

Note that the current study used  $\mu_{CA}$  values of 0.1, and 0.6 for both reinforced and unreinforced ballast specimens to calculate the geogrid gain factor. Only two  $\mu_{CA}$  values were considered to reduce the computational time requirements.

### 5.3 Parametric Study on Cyclic Triaxial Testing of Geogrid-Embedded Railroad Ballast Specimens

A series of simulations were performed to determine the effects of different material (i.e. particle-size distribution), and other test parameters (geogrid aperture size, and geogrid location) on railroad ballast response. The ballast gradation was chosen to be AREMA #24 – 45% having a specific gravity of 2.60 for the control section. A biaxial geogrid with square aperture size of 65 mm was used. A target confining pressure of 150 kPa was applied. The other model parameters used for this parametric study were same as the parameters shown in Table 5.1 and Table 5.2. Note that in the parametric

study all the model parameters were kept constant, but only the parameter of interest was varied to isolate its individual effect on the study results.

### 5.3.1 Effect of Ballast Gradations

The effect of particle-size distribution (or gradation) was primarily studied using five different ballast gradations conforming to AREMA specifications. When simulated, the number of particles for AREMA #4 LB, #4 UB, #24 LB, #24 - 45%, and #24 UB was 6696, 7705, 2798, 3116, and 3355 respectively. The geogrid gain factors calculated for each of these gradations are tabulated in Table 5.3. Note that the number of particles shown here is different from that of Chapter 4 where the fine particles were truncated. As seen from the table, the geogrid gain factor values for AREMA #4 LB are higher than the UB counterpart. This is probably due to the fact that the #4 LB specimen comprises less number of fines compared to the #4 UB specimen; this results in better confinement with the inclusion of geogrid. For AREMA #24 specimens on the other hand, no consistent trend while moving from the LB to the UB was observed. The geogrid gain factor value increased from the LB to 45% specimen, but then decreased from the 45% to UB specimen (see Table 5.3).

**Table 5.3 Comparative Evaluation of Geogrid Gain Factor Values Showing the Effect of Ballast Gradations**

Gradation	Geogrid Gain Factor		
	@0.05% axial strain	@0.10% axial strain	@0.20% axial strain
AREMA #4 LB	1.33	1.38	1.46
AREMA #4 UB	1.15	1.17	1.15
AREMA #24 LB	1.14	1.12	1.19
AREMA #24 - 45%	1.44	1.37	1.39
AREMA #24 UB	1.16	1.18	1.27

### 5.3.2 Effect of Geogrid Aperture Size

The geogrid aperture size was varied from 39 to 65 mm, and the calculated geogrid gain factor values are presented in Table 5.4. It was observed that geogrid inclusion increases secant modulus (resilient-modulus) values at all axial strain levels. This is true for both aperture sizes. However, aperture size of 65 mm exhibited the highest geogrid gain factor for the tested simulations (37% to 44% increment over the unreinforced configurations). This may be due to the fact that the ballast specimen has a top size of 76 mm, so aperture size of 39 mm was way too small to achieve adequate ballast-geogrid interlocking.

**Table 5.4 Comparative Evaluation of Geogrid Gain Factor Showing the Effect of Geogrid Aperture Size**

Aperture Size	Geogrid Gain Factor		
	@0.05% axial strain	@0.10% axial strain	@0.20% axial strain
39 mm (square)	1.12	1.07	1.04
65 mm (square)	1.44	1.37	1.39

### 5.3.3 Effect of Geogrid Location

The effect of geogrid location within the specimen was studied through simulation of three different cases: (i) one layer of geogrid at the mid depth of the specimen, (ii) two layers of geogrid- one layer at 152 *mm* from the top, the second layer at 152 *mm* from the bottom (see Figure 5.7), and (iii) two layers of geogrid- one layer at 254 *mm* from the top, and the second layer at 254 *mm* from the bottom (see Figure 5.7). These configurations were used based on the study reported by Mishra et al. (2014a). All the geogrids had 65 *mm* square aperture.

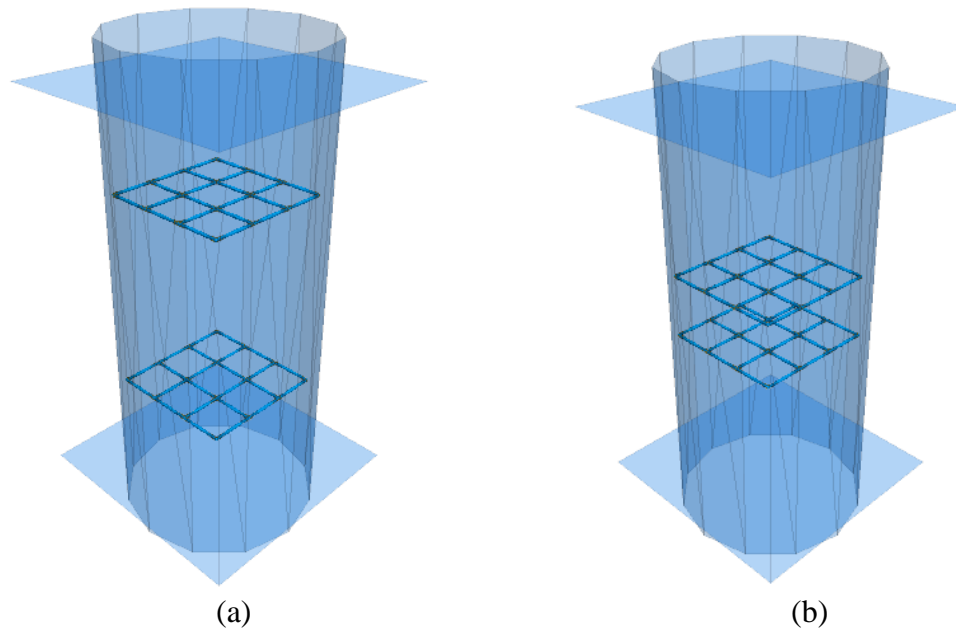


**Figure 5.7 Geogrid-Embedded Cylindrical Test Specimens at the End of Material Genesis Procedure: (a) Two Layers of Geogrid - One Layer at 152 *mm* from the Top, the Second Layer at 152 *mm* from the Bottom; and (b) Two Layers of Geogrid - One Layer at 254 *mm* from the Top, and the Second Layer at 254 *mm* from the Bottom**

The calculated geogrid gain factor values are listed in Table 5.5. As seen from the values, placing one layer of geogrid at the mid-depth resulted in the highest increase in resilient modulus compared to the unreinforced configuration.

**Table 5.5 Comparative Evaluation of Geogrid Gain Factor Showing the Effect of Geogrid Location**

Location	Geogrid Gain Factor		
	@0.05% axial strain	@0.10% axial strain	@0.20% axial strain
Middle	1.44	1.37	1.39
Double (one layer: 152 mm from the top, second layer: 152 mm from the bottom)	1.28	1.32	1.35
Double (one layer: 254 mm from the top, second layer: 254 mm from the bottom)	1.24	1.13	1.14

#### 5.4 Limitations Associated with DEM Simulations of Cyclic Triaxial Testing on Geogrid-Embedded Ballast Specimens

The DEM simulation of cyclic triaxial testing on geogrid-embedded railroad ballast specimens undertaken in this research effort has the following limitations.

1. In reality, ballast particles are irregular (polyhedral) in shape. But the version of 'pdPkg' used as the basic framework during this study did not accommodate any particles shapes other than spheres.
2. The 'pdPkg' was originally developed to support a larger research initiative of the Minnesota Department of Transportation (MnDOT) to better understand and quantify the structural benefit of including geogrid in the aggregate base layer of asphalt-surface roadways (Potyondy et al., 2016). The use of this package for railroad ballast is yet to be explored. In fact, to the author's knowledge, this research effort marks the first ever application of this framework to study geogrid-ballast interaction.

3. The simulation results are yet to be validated with laboratory-test results. This is planned to be done in the future.

### **5.5 Summary of Results from DEM Simulations of Cyclic Triaxial Testing on Geogrid-Embedded Ballast Specimens**

Major findings from this simulation task are summarized below.

1. For specimens conforming to AREMA #4 gradation, the LB specimens exhibited higher increase in resilient modulus (reflected by higher geogrid gain factor values) compared to the UB counterparts. This was probably due to the lower number of fine particles in the LB specimens. However, no such trend was observed for specimens conforming to AREMA #24 gradations.
2. Geogrid inclusion increased the ballast secant modulus values at all axial strain levels. Geogrid aperture size of 65 mm exhibited the highest geogrid gain factor among the tested configurations. Using the lower aperture size (39 mm) does not result in the same degree of geogrid-ballast interlock.
3. Placing one layer of geogrid at the mid depth resulted in the highest increase in resilient modulus compared to other reinforcement configurations.

The next chapter (Chapter 6) of this document will present summary and conclusions from this research effort, and will provide recommendations for future research.

## CHAPTER 6: SUMMARY OF FINDINGS AND RECOMMENDATIONS FOR FUTURE RESEARCH

### **6.1 Introduction**

In this chapter, first, a brief summary of findings from the research tasks performed under the scope of this Master's thesis effort has been presented. This is followed by recommendations for future.

### **6.2 Summary of Findings**

A commercially available three-dimensional Discrete Element Modeling (DEM) package, PFC3D<sup>®</sup> was used in this research effort to study the effects of particle-size distribution and packing characteristics on the shear strength behavior of railroad ballast; this was accomplished by simulating direct shear test, and triaxial monotonic shear strength tests on ballast specimen. A new gradation parameter termed as "Coarse-to-Fine Ratio" (C/F Ratio) was introduced as an indicator of packing condition within the ballast matrix, and the effect of this parameter on ballast shear strength was analyzed. In addition to studying the effects of different material, specimen and test parameters on shear strength of unreinforced ballast, another objective of this research was to investigate the different test and reinforcement configurations on geogrid-ballast interaction.

Once the DEM models of direct shear and triaxial monotonic shear strength tests were developed, available laboratory-test data were used to calibrate those models. Findings from the parametric analyses of different material, test, and specimen

parameters on ballast shear strength as obtained from DEM simulation of direct shear strength tests are summarized below:

1. For both AREMA #4 and AREMA #24 gradations, the finer gradation (UB) resulted in higher failure shear stress values compared to the coarser gradation (LB) for the two lower normal stress values (103.4 *kPa* and 137.9 *kPa*); the trend was reversed for the highest normal stress value (206.8 *kPa*).
2. Increasing the Flat and Elongated (F&E) ratio numbers led to significant increase in the ballast shear strength, with the maximum friction angle ( $\phi$ ) value approaching 81°. However, it should be noted that these results could be misleading, as the simulations do not account for the breakage of flat and elongated particles under loading. In real world application, using flat and elongated particles can have detrimental effects on ballast shear strength (due to increased fouling caused by ballast breakage). Per the simulation results, in a case where the flat and elongated particles do not break under loading, significant increase in the shear strength may be realized.
3. Increasing the angularity of ballast particles led to significant increase in the ballast shear strength also reflected through increasing friction angle values. The simulation results showed that the maximum increase in shear strength is realized as one moves from spherical particles to angular particles. Subsequent increase in the degree of angularity values does not lead to as drastic jumps on the friction angles.
4. As the aggregate top-size was varied from 38 to 76 *mm*, it was observed that the higher the aggregate top size, the higher the shear strength.

5. An increasing trend of failure shear stress and angle of internal friction was found with the increase in specimen specific gravity.
6. As the porosity value was increased, both the failure shear stress and the angle of internal friction decreased.
7. A higher coefficient of friction between the particles led to a higher shearing resistance and angle of internal friction angle values.
8. The failure shear stress increased with increase in applied normal stress values. An increase of 305% in the failure shear stress value was achieved as the normal stress was increased from 34.5 to 206.8 *kPa*.
9. The effect of particle packing on ballast shear strength was studied using a newly developed gradation parameter, referred to as the Coarse-to-Fine Ratio (C/F Ratio). DEM simulation results established that C/F values affected ballast shear strength behavior, with the effect being more significant for AREMA #24 compared to that for AREMA #4. C/F ratio of 1.51 exhibits the densest packing among the four gradations chosen in case of AREMA #24, which is evident from the failure shear stress for this C/F ratio. However, C/F ratio of 1.27 almost yields the best shear stress-displacement relations for all the different normal stresses of AREMA #4 gradation.

Findings from the parametric analyses of the triaxial monotonic shear strength testing of railroad ballasts indicated:

1. For both the AREMA #4 and AREMA #24 gradation, the UB (fine-end) of the gradation showed consistently higher shear strength values compared to the LB (coarse-end).

2. No particular trend was observed concerning the effect of material specific gravity on ballast shear strength.
3. As the porosity value was increased, both the peak deviator stress (at failure) and the angle of internal friction decreased.
4. A higher coefficient of friction between the particles led to a higher peak deviator stress (at failure) value.
5. The peak deviator stress (at failure) value increased with increasing confining stress levels. An increase of 334% in the peak deviator stress (at failure) value was achieved as the confining pressure was increased from  $34.5 \text{ kPa}$  ( $5 \text{ psi}$ ) to  $206.8 \text{ kPa}$  ( $30 \text{ psi}$ ).
6. As the suction pressure (moisture) value was increased, the peak deviator stress (at failure) increased.

Major findings from the parametric analyses of cyclic triaxial testing of geogrid-embedded railroad ballasts were:

1. For specimens conforming to AREMA #4 gradation, the LB specimens exhibited higher increase in resilient modulus (reflected by higher geogrid gain factor values) compared to the UB counterparts. This was probably due to the lower number of fine particles in the LB specimens. However, no such trend was observed for specimens conforming to AREMA #24 gradations.
2. Geogrid inclusion increased the ballast secant modulus values at all axial strain levels. Geogrid aperture size of  $65 \text{ mm}$  exhibited the highest geogrid gain factor

among the tested configurations. Using the lower aperture size (39 mm) does not result in the same degree of geogrid-ballast interlock.

3. Placing one layer of geogrid at the mid depth resulted in the highest increase in resilient modulus compared to other reinforcement configurations.

### 6.3 Recommendations for Future Research

There are several scopes for future improvement of the findings reported in this research study. Some of the future research recommendations are enumerated as follows:

1. Although one of the most widespread general-purpose Distinct Element Modeling framework, PFC3D<sup>®</sup>, was used as a DEM tool in this research effort, there are several avenues for further modifications and enhancement opportunities of the modeling approach related to the software's capabilities. For example:
  - a. in reality, ballast particles are irregular (polyhedral) in shape. PFC3D<sup>®</sup> is based on spheres as the primary building block for 3D simulations. The clumps approach (combining multiple spheres of different sizes to simulate complex-shaped particles) was used to simulate complex particles. However, it is important to note that this is not the same as simulating using "true" polyhedral particles. Incorporation of polyhedral particles to simulate railroad ballast can be an improvement over the study results.
  - b. the texture (roughness) of individual ballast particles plays a significant role in governing how well the particles slip past each another. However, DEM models are not capable of assigning particle roughness directly. In PFC3D<sup>®</sup> a rough particle texture is simulated by changing friction

coefficient values assigned to individual particles. This assumption may lead to differences between the laboratory-generated and simulated test results.

2. The laboratory validation of effects of the newly developed Coarse-to-Fine Ratio (C/F Ratio) gradation parameter on ballast shear strength is yet to be carried out. This may be done in the future and the findings can be compared to the reported results found through DEM simulations.
3. The simulated models of geogrid-embedded cyclic triaxial testing of railroad ballasts were not calibrated using any laboratory data. The simulation results should be compared to the laboratory-generated test data, and necessary calibration of the model parameters should be performed.
4. The models used during the current study treated the ballast particles as ‘unbreakable’; therefore, possible particle breakage during shearing at high strain levels could not be incorporated. Modeling the ballast particles as ‘breakable clumps’ may result in more realistic simulation of laboratory test conditions.

## REFERENCES

- “Rail Intermodal Keeps America Moving”. Association of American Railroads, May, 2016. Document Rail Intermodal.pdf accessed from [www.aar.org/BackgroundPapers](http://www.aar.org/BackgroundPapers) on November 16, 2016
- “Tensor® Geogrids”. Article accessed from <http://www.tensarcorp.com/Systems-and-Products/Tensar-geogrids> on August 7, 2017
- “What is DEM eBook”. Document accessed from <https://www.edemsimulation.com/download/ebooks/what-is-dem-ebook.pdf/> on March 1, 2017
- Abadi, T., Le Pen, L., Zervos, A., and Powrie, W. (2016). “A Review and Evaluation of Ballast Settlement Models using Results from the Southampton Railway Testing Facility (SRTF)”. *Procedia Engineering*, 143, 999-1006.
- American Railway Engineering and Maintenance-of-Way Association. (2016). “Manual for Railway Engineering”. Lanham, Maryland.
- Anderson, W. F., and Fair, P. (2008). “Behavior of railroad ballast under monotonic and cyclic loading”. *Journal of Geotechnical and Geoenvironmental Engineering*, 134(3), 316-327
- ASTM (2011). “D3080/D3080M: Standard Test Method for Direct Shear Test of Soils under Consolidated Drained Conditions”. American Society for Testing and Materials International, West Conshohocken, Pennsylvania, Vol. 04.08.
- Aursudkij, B., McDowell, G. R., and Collop, A. C. (2009). “Cyclic loading of railway ballast under triaxial conditions and in a railway test facility”. *Granular Matter*, 11(6), 391-401.
- Bathurst, R. J., and Raymond, G. P. (1987). “Geogrid reinforcement of ballasted track”. (No. 1153).

- Bilodeau, J. P., Dore, G., and Pierre, P. (2007). "Erosion susceptibility of granular pavement materials". *International Journal of Pavement Engineering*, 8(1), 55-66.
- Bilodeau, J. P., Dore, G., and Pierre, P. (2008). "Gradation influence on frost susceptibility of base granular materials". *International Journal of Pavement Engineering*, 9(6), 397-411.
- Brown, S. F., Kwan, J., and Thom, N. H. (2007). "Identifying the key parameters that influence geogrid reinforcement of railway ballast". *Geotextiles and Geomembranes*, 25(6), 326-335.
- Buchanan, S. (2007). "Resilient Modulus: What, Why, and How?". Vulcan Materials Company. [Document 2-Resilient-Modulus-Buchanan.pdf accessed from [www.vulcaninnovations.com/public/pdf](http://www.vulcaninnovations.com/public/pdf) on November 16, 2016.]
- CFDEMresearch GmbH. (2017). "LIGGGHTS(R)-PUBLIC Documentation, Version 3.X". Available from <https://www.cfdem.com/media/DEM/docu/Manual.html>
- Chen, C., McDowell, G. R., and Thom, N. H. (2013). "A study of geogrid-reinforced ballast using laboratory pull-out tests and discrete element modelling". *Geomechanics and Geoengineering*, 8(4), 244-253.
- Chen, L. S. (1948). "An investigation of stress-strain and strength characteristics of cohesionless soils by triaxial compression tests". *Proc. 2nd ICSMFE, Rotterdam*, 5, 35-43.
- Cheng, Y. P., Bolton, M. D., and Nakata, Y. (2004). "Crushing and plastic deformation of soils simulated using DEM". *Geotechnique*, 54(2), 131-142.
- Cundall, P. A., and Hart, R. D. (1992). "Numerical Modelling of Discontinua". *Engineering Computations* 9, No. 2, 100-113.
- Cundall, P. A., and Strack, O. D. L. (1978). "BALL-A program to model granular media using the distinct element method". Technical note.
- Cundall, P. A., and Strack, O. D. L. (1979). "A discrete numerical model for granular assemblies". *Géotechnique*, 29(1), 47-65.

- Das, B. M. (2010). "Use of Geogrid in Subgrade-Ballast System of Railroads Subjected to Cyclic Loading for Reducing Maintenance". California State University, Sacramento, USA.
- Dawson, A. R., Thom, N. H., and Paute, J. L. (1996). "Mechanical characteristics of unbound granular materials as a function of condition". Gomes Correia, Balkema, Rotterdam, 35-44.
- de Larrard, F., and Sedran, T. (1994). "Optimization of ultra-high-performance concrete by the use of a packing model". Cement and Concrete Research, 24(6), 997-1009.
- DEM Solutions. (2011). "EDEM 2.4 User Guide". Available from [http://tm.spbstu.ru/images/2/28/EDEM2.4\\_user\\_guide.pdf](http://tm.spbstu.ru/images/2/28/EDEM2.4_user_guide.pdf)
- Dissanayake, D. M. A. G. B., Kurukulasuriya, L. C., and Dissanayake, P. B. R. (2016). "Evaluation of shear strength parameters of rail track ballast in Sri Lanka". Journal of the National Science Foundation of Sri Lanka, 44(1).
- Dubois, F., Jean, M., Renouf, M., Mozul, R., Martin, A., and Bagneris, M. (2011). "Lmgc90". In 10e colloque national en calcul des structures (pp. Clé-USB).
- Dunn, C. S., and Bora, P. K. (1972). "Shear strength of untreated road base aggregates measured by variable lateral pressure triaxial cell". Journal of Materials, 7(2).
- Ekblad, J. (2007). "Influence of water on coarse granular road material properties". (Doctoral dissertation, KTH).
- Ghaboussi, J., and Barbosa, R. (1990). "Three-dimensional discrete element method for granular materials". International Journal for Numerical and Analytical Methods in Geomechanics, 14(7), 451-472.
- Giroud, J. P., and Han, J. (2004). "Design method for geogrid-reinforced unpaved roads. II. Calibration and applications". Journal of Geotechnical and Geoenvironmental Engineering, 130(8), 787-797.
- Goltermann, P., Johanson, V., and Palbol, L. (1997). "Packing of Aggregates: An Alternative Tool to Determine the Optimal Aggregate Mix". ACI Material Journal, 94(5), 435-443.

- Gu, X. Q., and Yang, J. (2013). "A discrete element analysis of elastic properties of granular materials". *Granular Matter*, 15(2), 139-147.
- Gur, Y., Shklarsky, E., and Livneh, M. (1967). "Effect of coarse-fraction flakiness on the strength of graded materials". In *Asian Conf Soil Mech & Fdn E Proc/Is/*.
- Haas, R., Wall, J., and Carroll, R. G. (1988). "Geogrid reinforcement of granular bases in flexible pavements". *Transportation Research Record 1188*, Transportation Research Board, Washington DC, 19–27.
- Huang, H. (2010). "Discrete element modeling of railroad ballast using imaging based aggregate morphology characterization". (Doctoral dissertation, University of Illinois at Urbana-Champaign).
- Huang, H., and Tutumluer, E. (2011). "Discrete element modeling for fouled railroad ballast". *Construction and Building Materials*, 25(8), 3306-3312.
- Huang, H., Tutumluer, E., and Dombrow, W. (2009). "Laboratory characterization of fouled railroad ballast behavior". *Transportation Research Record: Journal of the Transportation Research Board*, (2117), 93-101.
- Hveem, F. N. (1955). "Pavement deflections and fatigue failures". *Highway Research Board Bulletin*, No. 114, Washington, DC, pp. 43-87.
- Hveem, F. N., and Carmany, R. M. (1948). "The factors underlying the rational design of pavements". *Proc. Highway Research Board 28*, Washington, DC, pp. 101-136.
- Indraratna, B., Ionescu, D., and Christie, H. D. (1998). "Shear behavior of railway ballast based on large-scale triaxial tests". *Journal of Geotechnical and Geoenvironmental Engineering*, 124(5), 439-449.
- Indraratna, B., Khabbaz, H., Salim, W., and Christie, D. (2006). "Geotechnical properties of ballast and the role of geosynthetics in rail track stabilization". *Journal of Ground Improvement*. 10 (3), 91e102.
- Indraratna, B., Ngo, N. T., Rujikiatkamjorn, C., and Vinod, J. S. (2012). "Behavior of fresh and fouled railway ballast subjected to direct shear testing: discrete element simulation". *International Journal of Geomechanics*, 14(1), 34-44.

- Indraratna, B., Thakur, P. K., and Vinod, J. S. (2009). "Experimental and numerical study of railway ballast behavior under cyclic loading". *International Journal of Geomechanics*, 10(4), 136-144.
- Ionescu, D., Indraratna, B., and Christie, H. D. (1998). "Behaviour of railway ballast under dynamic loads". In *Thirteenth Southeast Asian Geotechnical Conference* (pp. 69-74).
- Itasca (2016). "Particle Flow Code in Three Dimensions – PFC 5.0 Documentation". Itasca Consulting Group, Inc., Minnesota.
- Jas. H., Stahl, M., Konietzky, H., te Kamp, L., and Oliver, T. (2015) "Discrete Element Simulation of Geogrid Stabilized Sub-Base: Modelling and Calibration and Plate Load Simulation under Special Consideration of Important Boundary Conditions". to appear in *Sixth Symposium on Deformation Characteristics of Geomaterials*.
- Jenkins. J.T., Cundall, P.A., and Ishibashi, I. (1989). "Micromechanical modeling of granular materials with the assistance of experiments and numerical simulations". *Powders and grains*, 257-264.
- Jensen, R. P., Edil, T. B., Bosscher, P. J., Plesha, M. E., and Kahla, N. B. (2001). "Effect of particle shape on interface behavior of DEM-simulated granular materials". *International Journal of Geomechanics*, 1(1), 1-19.
- Jo, S. A., Kim, E. K., Cho, G. C., and Lee, S. W. (2011). "Particle shape and crushing effects on direct shear behavior using DEM". *Soils and foundations*, 51(4), 701-712.
- Kang, D. H., Choo, J., and Yun, T. S. (2013). "Evolution of pore characteristics in the 3D numerical direct shear test". *Computers and Geotechnics*, 49, 53-61.
- Kashani, H. F., Ho, C. L., and Hyslip, J. P. (2017). "Evaluating the Effect of Breakdown Fouling and Water Content on the Ballast Degradation Characteristics". In *2017 Joint Rail Conference* (pp. V001T01A001-V001T01A001). American Society of Mechanical Engineers.

- Kim, B. S., Park, S. W., and Kato, S. (2014). "Distinct element method simulation on deformation mode and stress state for specimen shape in direct shear test". *International Journal of Computational Methods*, 11(02), 1342004.
- Kim, B. S., Takeshita, Y., Park, S. W., and Kato, S. (2016). "Study on opening between shear boxes using DEM simulation". *Japanese Geotechnical Society Special Publication*, 2(18), 681-684.
- Kim, S. H., Tutumluer, E., Little, D. N., and Kim, N. (2007). "Effect of gradation on nonlinear stress-dependent behavior of a sandy flexible pavement subgrade". *Journal of Transportation Engineering*, 133(10), 582-589.
- Koerner, R. M. (1998). "Designing with Geosynthetics". Fourth Edition, Prentice Hall, Upper Saddle River, New Jersey.
- Kolisoja, P. (1998). "Resilient deformation characteristics of granular materials". Tampere University of Technology.
- Konietzky, H., te Kamp, L., Groeger, T., and Jenner, C. (2004). "Use of DEM to model the interlocking effect of geogrids under static and cyclic loading". *Numerical modeling in micromechanics via particle methods*, 3-12.
- Kozicki, J., and Donzé, F. V. (2009). "Yade-open dem: an open-source software using a discrete element method to simulate granular material". *Engineering Computations*, 26(7), 786-805.
- Lackenby, J., Indraratna, B., McDowell, G., and Christie, D. (2007). "Effect of confining pressure on ballast degradation and deformation under cyclic triaxial loading". *Geotechnique* 57, No. 6, 527-536.
- Lees, G. (1964). "The measurement of particle shape and its influence in engineering materials". British Granite and Whinstone Federation.
- Lekarp, F. (1999). "Resilient and permanent deformation behavior of unbound aggregates under repeated loading". (Doctoral dissertation, Institutionen för infrastruktur och samhällsplanering).

- Lekarp, F., Isacsson, U., and Dawson, A. (2000). "State of the art. I: Resilient response of unbound aggregates". *Journal of transportation engineering*, 126(1), 66-75.
- Lim, W. L., and McDowell, G. R. (2005). "Discrete element modeling of railway ballast". *Granular Matter*, 7(1), 19-29.
- Liu, S. H. (2006). "Simulating a direct shear box test by DEM". *Canadian Geotechnical Journal*, 43(2), 155-168.
- Love, J. P. (1984). "Model testing of geogrids in unpaved roads". Doctoral dissertation, Univ. of Oxford, Oxford, UK.
- Lu, M. and McDowell, G. R. (2007). "The importance of modelling ballast particle shape in the discrete element method". *Granular matter*, 9(1-2), 69-80.
- Lu, M., and McDowell, G. R. (2010). "Discrete element modelling of railway ballast under monotonic and cyclic triaxial loading". *Géotechnique*, 60(6), 459-467.
- Masad, E., and Button, J. W. (2000). "Unified imaging approach for measuring aggregate angularity and texture". *Computer-Aided Civil and Infrastructure Engineering*, 15(4), 273-280.
- Masad, E., Olcott, D., White, T., and Tashman, L. (2001). "Correlation of fine aggregate imaging shape indices with asphalt mixture performance". *Transportation Research Record: Journal of the Transportation Research Board*, (1757), 148-156.
- McDowell, G. R., and Li, H. (2016). "Discrete element modelling of scaled railway ballast under triaxial conditions". *Granular Matter*, 18(3), 1-10.
- McDowell, G. R., Harireche, O., Konietzky, H., Brown, S. F., and Thom, N. H. (2006). "Discrete element modelling of geogrid-reinforced aggregates". *Proceedings of the Institution of Civil Engineers-Geotechnical Engineering*, 159(1), 35-48.
- McGown, A., Kupec, J., Heerten, G., and von Maubeuge, K. (2005). "Testing biaxial geogrids for specification and design purposes". In *Geosynthetics Research and Development in Progress* (pp. 1-11).
- Mishra, D., Qian, Y., Kazmee, H., and Tutumluer, E. (2014a). "Investigation of geogrid-reinforced railroad ballast behavior using large-scale triaxial testing and discrete

- element modeling”. *Transportation Research Record: Journal of the Transportation Research Board*, (2462), 98-108.
- Mishra, D., Tutumluer, E., Boler, H., Hyslip, J., and Sussmann, T. (2014b). “Railroad track transitions with multidepth deflectometers and strain gauges”. *Transportation Research Record: Journal of the Transportation Research Board*, (2448), 105-114.
- Nezami, E. G., Hashash, Y. M., Zhao, D., and Ghaboussi, J. (2004). “A fast contact detection algorithm for 3-D discrete element method”. *Computers and Geotechnics*, 31(7), 575-587.
- Ngo, N. T., Indraratna, B., and Rujikiatkamjorn, C. (2014). “DEM simulation of the behaviour of geogrid stabilised ballast fouled with coal”. *Computers and Geotechnics*, 55, 224-231.
- Ngo, N. T., Indraratna, B., and Rujikiatkamjorn, C. (2015). “Investigating the shear behaviour of fouled ballast using discrete element modelling”. *International Journal of Civil, Environmental, Structural, Construction and Architectural Engineering Vol:9, No:12*.
- Ngo, N. T., Indraratna, B., and Rujikiatkamjorn, C. (2016). “Micromechanics-based investigation of fouled ballast using large-scale triaxial tests and discrete element modeling”. *Journal of Geotechnical and Geoenvironmental Engineering*, 04016089.
- Ni, Q., Powrie, W., Zhang, X., and Harkness, R. (2000). “Effect of particle properties on soil behavior: 3-D numerical modeling of shearbox tests”. In *Numerical methods in geotechnical engineering* (pp. 58-70). ASCE.
- O’Sullivan, C., Cui, L., and Bray, J. D. (2004). “Three-dimensional discrete element simulations of direct shear tests”. *Numerical Modeling in Micromechanics via Particle Methods*, 373-382.
- Pan, T., Tutumluer, E., and Anochie-Boateng, J. (2006). “Aggregate morphology affecting resilient behavior of unbound granular materials”. *Transportation Research Record: Journal of the Transportation Research Board*, (1952), 12-20.

- Pan, T., Tutumluer, E., and Carpenter, S. (2005). "Effect of coarse aggregate morphology on the resilient modulus of hot-mix asphalt". *Transportation Research Record: Journal of the Transportation Research Board*, (1929), 1-9.
- Pan, T., Tutumluer, E., and Carpenter, S. H. (2004). "Imaging based evaluation of coarse aggregate used in the NCAT pavement test track asphalt mixes". In *International Symposium on Design and Construction of Long Lasting Asphalt Pavements*, Auburn, Alabama, USA.
- Penman, J. and Priest, D. J. (2009). "The Use of Geogrids in Railroad Applications". PDH Article Series. [Document *The Use of Geogrids in Railroad Applications.pdf* accessed from <http://www.conteches.com> on November 16, 2016.]
- Potyondy, D. (2016). "PFC 5 Documentation Set: Hill Contact Model [version 4]".
- Potyondy, D. (2017a). "PFC 5 Documentation Set: Material-Modeling Support in PFC [fistPkg25].
- Potyondy, D. (2017b). "PFC 5 Documentation Set: Pavement-Design Package for PFC3D [pdPkg12]".
- Potyondy, D., Siekmeier, J., and Petersen, L. (2016). "Aggregate-Geogrid Interaction Model Incorporating Moisture Effects". In *Transportation Research Board 95th Annual Meeting* (No. 16-6085).
- Qian, Y., Lee, S., Tutumluer, E., Hashash, Y., Mishra, D., and Ghaboussi, J. (2013). "Simulating Ballast Shear Strength from Large-Scale Triaxial Tests: Discrete Element Method". *Transportation Research Record: Journal of the Transportation Research Board*, (2374), 126-135.
- Qian, Y., Mishra, D., Tutumluer, E., and Kazmee, H. A. (2015). "Characterization of geogrid reinforced ballast behavior at different levels of degradation through triaxial shear strength test and discrete element modeling". *Geotextiles and Geomembranes*, 43(5), 393-402.
- Qian, Y., Tutumluer, E., Mishra, D., and Kazmee, H. (2014). "Behavior of Geogrid Reinforced Ballast at Different Levels of Degradation". In *Geo-Shanghai 2014*.

- Rao, C., Tutumluer, E., and Kim, I. T. (2002). "Quantification of coarse aggregate angularity based on image analysis". *Transportation Research Record: Journal of the Transportation Research Board*, (1787), 117-124.
- Raymond, G. P. and Bathurst, R. J. (1987). "Performance of large-scale model single tie-ballast systems". *Transportation Research Record* 1131, pp. 7-14.
- Raymond, G.P., Gaskin, P.N., and Svec, O. (1978). "Selection and performance of railroad ballast". In: Kerr, A.D. (Ed.), *Railroad Track Mechanics and Technology*. Pergamon Press, Oxford, pp. 369–385.
- Roberts, F., Kandle, P., Brown, E.R., Lee, D., and Kennedy, T. (1996). "Hot Mix Asphalt Materials, Mixture Design and Construction". NAPA Research and Education Foundation, Second Edition.
- Rohrman, A. K., Kashani, H. F., and Ho, C. L. (2017). "Influence of Fouling and Water Content of Ballast on Railway Substructure Bearing Capacity". In 2017 Joint Rail Conference (pp. V001T01A010-V001T01A010). American Society of Mechanical Engineers.
- Rothenburg, L. and Bathurst, R. J. (1989). "Analytical study of induced anisotropy in idealized granular materials". *Geotechnique*, 39(4), 601-614.
- Roy, D. M., Scheetz, B. E., and Silsbee, M. R. (1993). "Processing of optimized cements and concretes via particle packing". *MRS bulletin*, 18(03), 45-49.
- Santanusana Isach, M. (2013). "Kratos Dem, a paralel code for concrete testing simulations using the discrete element method". (Master's thesis, Universitat Politècnica de Catalunya).
- Seed, H. B., Chan, C. K., and Lee, C. E. (1962). "Resilience characteristics of subgrade soils and their relation to fatigue failures in asphalt pavements". In *International Conference on the Structural Design of Asphalt Pavements. Supplement*.
- Selig, E. T., and Roner, C. J. (1987). "Effects of particle characteristics on behavior of granular material". *Transportation Research Record*, (1131).

- Selig, E. T., and Waters, J. M. (1994). "Track geotechnology and substructure management". Thomas Telford.
- Siekmeier, J., Bittmann, J., Potyondy, D., and Petersen, L.. (2016). "Introducing a Geogrid Gain Factor for Flexible Pavement Design". in Proceedings University of Minnesota 64th Annual Geotechnical Engineering Conference.
- Stahl, M., and Konietzky, H. (2011). "Discrete Element Simulation of Ballast and Gravel under Special Consideration of Grain-Shape, Grain-Size and Relative Density". *Granular Matter*, 13, 417-428.
- Stahl, M., and te Kamp, L. (2012). "Project 12206: Geogrid Modelling with PFC3D - Generation and Calibration of TriAx-Geogrid TX160". Itasca Consultants GmbH, Gelsenkirchen, Germany, Report to Tensar International Ltd., United Kingdom, Report 01-2012.
- Stahl, M., and te Kamp, L. (2013). "Project 13008: Geogrid Modelling with PFC3D— Generation and Calibration of Biaxial Geogrid SS20". Itasca Consultants GmbH, Gelsenkirchen, Germany, Report to Tensar International Ltd., United Kingdom, Report 01-2013.
- Stahl, M., Konietzky, H., te Kamp, L., and Jas, H. (2014). "Discrete Element Simulation of Geogrid-Stabilised Soil". *Acta Geotechnica*, 9, 1073-1084.
- Suiker, A. S., Selig, E. T., and Frenkel, R. (2005). "Static and cyclic triaxial testing of ballast and subballast". *Journal of geotechnical and geoenvironmental engineering*, 131(6), 771-782.
- Sukumaran, B., and Ashmawy, A. K. (2001). "Quantitative characterisation of the geometry of discret particles". *Geotechnique*, 51(7), 619-627.
- Talbot, A. N., and Richart, F. E. (1923). "The strength of concrete-its relation to the cement, aggregates and water". *Bulletin*, No. 137, 1923, pp. 1–116.
- Tamás, K., Kovács, Á., and Jóri, I. J. (2016). "The Evaluation of the Parallel Bond's Properties in DEM Modeling of Soils". *Periodica Polytechnica. Engineering. Mechanical Engineering*, 60(1), 21.

- Tan, D.S., Khazanovich, L., Siekmeier J., and Hill, K.M.. (2014). "Discrete Element Modeling of Effect of Moisture and Fine Particles in Lightweight Deflectometer Test". *Transportation Research Record: Journal of the Transportation Research Board*, No. 2433, 58–67, DOI: 10.3141/2433- 07. Washington, D.C.: Transportation Research Board of the National Academies.
- Thom, N. H., and Brown, S. F. (1988). "The effect of grading and density on the mechanical properties of a crushed dolomitic limestone". In *Australian Road Research Board (ARRB) Conference, Canberra (Vol. 14, No. 7)*.
- Trollope, D. H., Lee, I. K., and Morris, J. (1962). "Stresses and deformation in two layer pavement structures under slow repeated loading". In *Australian Road Research Board (ARRB) Conference, Canberra (Vol. 1, No. 2)*.
- Tsuji, Y., Tanaka, T., and Ishida, T. (1992). "Lagrangian numerical simulation of plug flow of cohesionless particles in a horizontal pipe". *Powder technology*, 71(3), 239-250.
- Tutumluer, E., Huang, H., and Bian, X. (2009)." Research on the behavior of geogrids in stabilization applications". In: *Proc., Jubilee Symposium on Polymer Geogrid Reinforcement*.
- Tutumluer, E., Huang, H., Hashash, Y., and Ghaboussi, J. (2006). "Aggregate shape effects on ballast tamping and railroad track lateral stability". In *AREMA Annual Conference, Louisville, KY, Sept (pp. 17-20)*.
- Vantuono, W. C. (2011). "The greening of the railroads-and why it matters". *Railway Age*, 212(2).
- Vavrik, W., Pine, W., and Carpenter, S. (2002). "Aggregate blending for asphalt mix design: Bailey method". *Transportation Research Record: Journal of the Transportation Research Board*, (1789), 146-153.
- Walls, J. C., and Galbreath, L. L. (1987). "Railroad ballast reinforcement using geogrids". In *Proceedings of geosynthetics (Vol. 87, pp. 38-45)*.
- Wang, J., and Gutierrez, M. (2010). "Discrete element simulations of direct shear specimen scale effects". *Géotechnique*, 60(5), 395-409.

- Wang, Z., Jing, G., Yu, Q., and Yin, H. (2015). "Analysis of ballast direct shear tests by discrete element method under different normal stress". *Measurement*, 63, 17-24
- Warne, T. R. (2004). "2010 and Beyond: A vision of America's Transportation Future". Document NCHRP20-24(33)CFinal.pdf accessed from <http://onlinepubs.trb.org/onlinepubs/archive/NotesDocs> on November 16, 2016
- Wikipedia. (2015) Entry for "young's modulus polypropylene" on June 4, 2015.
- Xiao, Y., Tutumluer, E., Qian, Y., and Siekmeier, J. (2012). "Gradation effects influencing mechanical properties of aggregate base-granular subbase materials in Minnesota". *Transportation Research Record: Journal of the Transportation Research Board*, (2267), 14-26.
- Yan, W. M. (2009). "Fabric evolution in a numerical direct shear test". *Computers and Geotechnics*, 36(4), 597-603.
- Yideti, T. F., Birgisson, B., Jelagin, D., and Guarin, A. (2013). "Packing theory-based framework to evaluate permanent deformation of unbound granular materials". *International Journal of Pavement Engineering*, 14(3), 309-320.
- Zhao, D., Nezami, E. G., Hashash, Y. M., and Ghaboussi, J. (2006). "Three-dimensional discrete element simulation for granular materials". *Engineering Computations*, 23.
- Zhou, Q., Shen, H. H., Helenbrook, B. T., and Zhang, H. (2009). "Scale dependence of direct shear tests". *Chinese Science Bulletin*, 54(23), 4337-4348. (7), 749-770.